Simulating Blast Effects in Steel Skeletal Structures

by Emily Leigh Guzas

SIMULATING BLAST EFFECTS IN STEEL SKELETAL STRUCTURES

A Dissertation

Presented to the Faculty of the Graduate School

of Cornell University

in Partial Fulfillment of the Requirements for the Degree of

Doctor of Philosophy

by

Emily Leigh Guzas

August 2010

SIMULATING BLAST EFFECTS IN STEEL SKELETAL STRUCTURES

Emily Leigh Guzas, Ph.D.

Cornell University 2010

This research embodies a synergistic application of sophisticated commercial finite element codes and internally developed software tools. The contribution to the state of the art is the development of a new approach to constitutive modeling, within a computationally expedient framework, which enables the consideration of blast effects in steel skeletal structures composed of wide-flange members. This research is split into three main parts: (1) development of an air blast load generation code, derived from openly available sources, to calculate spatially and temporally varying blast loads on a structure for a given explosive scenario, (2) formulation and implementation of a blast beam-column element (macro-element) that encapsulates the effects of an explosion on the capacity of a single steel wide-flange member, and (3) testing of the blast beam-column element approach, as implemented in a nonlinear explicit dynamic finite element code, through various validation and application examples. Regarding the first part of the research, blast loading from explosive air burst is modeled using a series of empirical parameters and equations derived from open literature sources, where loads are represented by overpressure time histories that are applied in a spatially varying manner over a finite element domain. Sensitivity studies carried out for dynamic behavior of a plate and girder subjected to blast loading with variations in load parameters show that structural response is sensitive to small changes in load definition. Regarding the second part of the research, a new method for modeling the reserve capacity of a blast-damaged structural

component is derived that uses bounding surface plasticity models, defined in stress-resultant space, to represent the effects of the blast by way of a plastic reduction matrix. Each bounding surface is created by generating numerical failure data for a given component and explosive scenario through a series of virtual load tests (using a high-resolution model of a wide-flange member in LS-DYNA), and then fitting the data to a continuous function. For each test, a member that has already been damaged by blast loading (within a dynamic nonlinear finite element analysis), is statically loaded to failure in separate collapse analyses, each with a unique combination of proportional moment-thrust loading. Given a specific blast location and explosive yield, the locus of all force points (moment and axial loads) at failure defines the bounding surface for this member, for a particular blast, where this bounding surface is approximated by a continuous function that is a linear combination of real-valued spherical harmonic functions. Regarding the third part of the research, an automated process is implemented to create a library of bounding surface plasticity models representing the reserve capacity for various wide-flange members under different explosive scenarios. The library of bounding surfaces is coupled to a developed nonlinear explicit dynamic finite element code, written in C, that includes the blast beam-column element. The code does not explicitly model the explosion itself but rather calculates a series of parameters that define the explosion location relative to a given member, and then accesses the library of bounding surfaces to find the bounding surface with parameters that most reasonably approximate the actual physical explosive scenario, and member geometry. Finally, the macro-element-based code is used to predict the post-blast collapse load of a structural system in a few representative test problems, in order to assess accuracy of results and computational savings.

BIOGRAPHICAL SKETCH

The author grew up in Herndon, VA, which is a suburb of Washington, D.C., and attended Herndon High School there. In 2002, she received a Bachelor of Science in Civil Engineering from the University of Virginia. Upon graduating, she worked as a bridge engineer with URS Corporation in Hunt Valley, MD, performing bridge inspections for movable bridges, designing and detailing a few highway bridges, and reviewing shop drawings. In 2004, she enrolled in the graduate program within the School of Civil and Environmental Engineering at Cornell University. In the summer of 2006, Emily worked at Sandia National Laboratories in Albuquerque, NM. While there, her efforts focused on researching and testing new diagnostic techniques to measure air blast overpressure loading. In the fall of 2006, Emily started work with Dr. Christopher Earls at Cornell University, and received her Master of Science in January 2008. Her graduate coursework has focused on Structural Engineering (major), and Solid Mechanics and Civil Infrastructure Systems (minors).

This document is dedicated to my husband, Brian, and to my parents, Clara and Doug.

ACKNOWLEDGEMENTS

Many thanks to my thesis advisor, Chris Earls, for accepting me as his student partway through my studies and letting me run with my unconventional ideas. I would also like to thank my committee member, Chris Conley, for providing mentoring and support as I transitioned into work with Dr. Earls. Additionally, thanks to Ken Hover for being such a wonderful teaching mentor. And finally I must thank Heather Reed for all the effort she put forth toward preliminary code development for the research presented in the second and third papers of this dissertation.

I would also like to recognize my funding sources. The material presented in this dissertation is based upon work supported under a National Science Foundation Graduate Research Fellowship and under departmental funding from the School of Civil and Environmental Engineering at Cornell University.

On a personal level, I would like to acknowledge my husband, Brian Guzas – I cannot thank you enough for helping me get back on the (iron) horse after each and every fall! In the number two slot, I will thank my fellow Earls group member, Chris Stull. With much coffee and discourse (scholarly and not), we made it through graduate school together. Also, thanks to "The Concrete Crew", Devon (Cordle) Hahn and Jenn Lewis, for all the support from our days at the University of Virginia and beyond. Thanks to Megan McDonald, for bracketing my time in Ithaca and having a talent for finding new and fun activities in any place, including our own Ithaca. Finally, thanks to Mike Ludgate and the BikeSki group for all of the hospitality, and for introducing me to mountain biking. I will dearly miss our rides in Hammond Hill and Shindagin State Forests.

A special thanks to my family and to the Guzas family for helping me escape Cornell now and then and reminding me of the supreme importance of family.

TABLE OF CONTENTS

LIST OF TABLES

LIST OF FIGURES

CHAPTER 1

AIR BLAST LOAD GENERATION FOR SIMULATING STRUCTURAL RESPONSE

1.1 Abstract

The current research presents a detailed methodology for generating air blast loading for use within a finite element context. Parameters describing blast overpressure loading on a structure are drawn from open literature sources and incorporated within a blast load generation computer code developed for this research. This open literature approach lends transparency to the details of the blast load modeling, as compared with many commonly used approaches to blast load generation, for which the details are not publicly available. As a demonstration, the load generation code is used with the finite element software LS-DYNA to simulate the response of a steel plate and girder subjected to explosions modeled using these parameters as well as blast parameters from other sources.

1.2 Introduction

In recent years, human threat to structures has become highlighted as a concern worldwide. The results of terrorist attacks have demonstrated that conventionally designed structures are vulnerable to explosive loading, with localized blast damage initiating global collapse in some cases [23]. As it is that this particular scenario is outside of the realm of common practice for structural engineers, it

is important that an understanding of the unique loading features of the hazard be considered. Along these lines, a transparent means for generating analogs to air blast loading of structures is a required point of departure supporting this outcome.

1.2.1 Overview

Air blast, which involves the detonation of explosive material in air, can be modeled with a decaying exponential equation form that uses a series of parameters, which depend on explosive charge size, type, and distance to a target. There are numerous different sets of air blast parameter data available in the literature, both in graphical and equation forms [6, 7, 41, 40, 59]. However, the data provided in these sources varies in terms of usability and completeness, as discussed in detail in a separate section of this paper.

Thus, one of the objectives of the research presented herein is to provide a complete set of blast parameter definitions from the open literature and to implement these in a load generation code to produce air blast loading for finite element simulations of structures subjected to explosive air burst. By employing open literature sources only, the designer is able to investigate all assumptions in the load generation process, something that is not possible when using load generation software that is restricted in usage and distribution. The air blast load generation code developed for this research is capable of applying spatially and temporally varying blast loads to a structure. Improvements on a previously published approach for air blast load generation by Chock and Kapania [21] are the inclusion of angle of incidence and shielding effects, and the

use of equation forms for parameters rather than relying on tabular data.

Also, since there exist numerous disparate collections of air blast parameter data, a second goal of this research is to compare structural responses corresponding to different sets of parameter data, where the blast loading is applied to the test problems using the developed blast load generation code. The intent here is to examine any difference in response as a result of relatively small, but legitimate, changes in parameter definition.

1.2.2 Literature review

There is a variety of previous research regarding different air blast modeling approaches and uncertainty in explosive air burst. Beshara [11] drew on sources in the unclassified literature to review numerous aspects of external blast load modeling on aboveground structures, including equations for various parameters. Beshara pointed out that structural response depends on numerous blast loading parameters, all of which are difficult to define with any certainty.

Santiago and Bhattacharya [54] investigated the response of an aluminum plate to an air blast, where the loading is based on an uncoupled hydrocode calculation of a shock wave. The hydrocode results were sampled at different spatial intervals, producing loading functions varying widely in terms of peak overpressure, impulse, and arrival time. Their results showed that the plate response is most sensitive to an impulse parameter.

Chock and Kapania [21] provided an in-depth review of air blast phenomenology, and compared the air blast loading approaches used by Baker

[6] versus Kingery and Bulmash [40]. They also developed an air blast load generation code based on the graphical results of Baker and the equations of Kingery and Bulmash. They compared a blast overpressure profile for one explosion scenario, and evaluated the structural response of an arbitrary aircraft wing subjected to an explosion modeled using the Kingery-Bulmash equations.

Bogosian et al. [15] compared air blast loading produced by three major blast generation programs, ConWep, SHOCK, and BlastX, all of which are restricted to use by the U.S. military and government contractors. They focused on the parameters of reflected positive phase overpressure, positive incident overpressure, positive incident impulse, as well as a few negative phase parameters. They developed a database of experimental explosives data for a wide variety of explosion sizes, charge materials and shapes, and blast scenarios, covering a range of scaled distances from 1.2–40 $m/kg^{1/3}$. Their statistical analysis indicated that the two-sigma range of parameter values was 1/3 to 2/3, a very large range.

Baylot and Rickman [10] followed up on the work of Bogosian et al. [15] with an investigation of the uncertainty in air blast overpressures and impulses, as measured experimentally. They carried out small scale (1:50) experiments of a nine-building arrangement simulating an urban setting, where data were taken from a number of pressure transducers located on the different buildings. When comparing anywhere from 4–11 measurements of the same parameters for nominally identical charge sizes and standoff distances, they found that the maximum values for a parameter deviated from 15% to 90% above the averaged value for a test.

Florek and Benaroya [27] reviewed research on air blast load modeling approaches and their effects on structural deflections, especially with regard to aviation structures. They focused on the analysis of beams, plates, shells, and single degree of freedom (SDOF) systems as representative structures subjected to pulse loading of a variety of shapes, from triangular to square to decaying exponential. In particular, they discussed attempts to eliminate pulse shape effects in rigid plastic materials.

Borenstein and Benaroya [16] examined the response of a clamped aluminum plate to a simulated blast loading employing a decaying exponential form, with either an instantaneous rise or a finite rise to a peak overpressure level. The rectangular plate was modeled as an elastic-perfectly plastic material, with the plasticity modeled via plastic yield lines in a standard envelope pattern. In order to create samples of loading for a Monte Carlo analysis, they assumed that one (or sometimes all) of the loading parameters was a uniformly distributed random variable, with any remaining variables (determined from Kingery and Bulmash [40]) left deterministic. Their sensitivity study determined that, in the majority of cases, the structural response was most sensitive to load duration time.

The current work builds upon previous research in numerous aspects. First, it provides a complete set of parameter equations from the open literature, drawn from Kinney and Graham [41] and Brode [18]. These open air literature sources are vital for analysts needing to understand the assumptions inherent within the loading model, thus avoiding a "black box" condition. Also, this research compares structural responses for a plate and a girder subjected to loading modeled with these parameters, with the well-known Kingery-Bulmash

parameters, and also with equivalent triangular pulse loading. These example problems demonstrate the code capability when used as a preprocessor to generate loading for nonlinear finite element analyses carried out using commercial software.

1.2.3 Paper organization

Background on air blast phenomenology is given in Section 1.3 of the current paper, while Section 1.4 includes information about air blast parameters (including the proposed parameter equations) and discusses the development of the air blast load generation code. Section 1.5 presents the case studies examined for this research: a plate and a girder subjected to various air blast loadings. Case study results are presented in Section 1.6 and conclusions are drawn in Section 1.7.

1.3 Air blast phenomenology

1.3.1 Air blast overpressures

The evolution of an air blast involves various stages: detonation, shock wave formation and propagation, and a decay in the shock wave strength that ends with a return to ambient conditions. In the context of this research, air blast refers to the detonation of a conventional high explosive, such as Trinitrotoluene (TNT), in air.

Following detonation, an explosive air burst arises out of a rapid expansion of gases that initiates a shock wave. The shock wave propagates radially outwards from the detonation epicenter. At the shock wave front there is a sharp discontinuity in air pressure, to a peak level above atmospheric conditions (peak overpressure), representing the compression of the air medium. Fig. 1.1 shows a schematic of a typical time history of overpressure at a stationary location affected by an explosion in air. This overpressure time history, or air blast profile, consists of a positive phase and a negative (suction) phase. In many cases, the negative phase of the blast overpressure time history can be ignored for structures, especially those without an abundance of frangible materials [7].

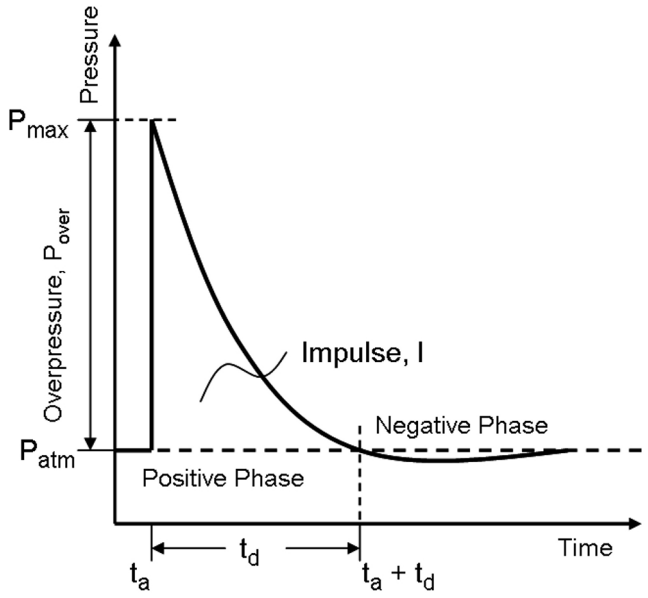

Figure 1.1: Schematic of a typical open air blast profile.

Any structure or object in the path of the shock wave will reflect the wave. The obstruction of the air velocity at the structure surface induces a significant increase in load on the structure. Thus, when describing the loading on a structure induced by explosive air burst, reflected and side-on (free air) cases

are treated separately, with different values for reflected peak overpressure and side-on peak overpressure.

At a stationary point in space, the effects of air blast have frequently been modeled with a modified Friedlander's equation [16], as

$$P(t) = \begin{cases} 0, & t < t_a, \\ P_{max}\left(1 - \frac{t-t_a}{t_d}\right) e^{-b\left(\frac{t-t_a}{t_d}\right)}, & t_a \leq t \leq t_a + t_d, \\ 0, & t > t_a + t_d, \end{cases} \tag{1.1}$$

where $P(t)$ is the overpressure at time t after detonation, P_{max} is the peak overpressure, t_a is the arrival time of the shock wave, t_d is the duration of the shock wave, and b is the decay constant. Depending on whether or not the point of interest is located on the surface of an object, P_{max} is either equal to P_s, the peak side-on overpressure (in free air) or P_r, the maximum reflected overpressure (upon shock wave reflection at a rigid surface).

1.3.2 Blast scaling

In empirical approaches, air blast parameters are most often presented for a reference explosion, and some type of scaling is subsequently used to obtain the parameter values for the actual charge weight of interest [6, 7, 41, 59]. The two types of scaling most commonly used are Sach's scaling and Hopkinson scaling [6, 7, 41]. Sach's scaling is a more generic form of Hopkinson scaling that is especially suited for predicting characteristics of blast waves from explosive bursts at high altitudes, such as nuclear bomb detonations [7]. Since the current research is focused on detonations of conventional high explosives, instead of nuclear materials, Hopkinson scaling is appropriate.

The Hopkinson scaling law states that when two charges of the same explosive material are detonated in the same atmospheric conditions, similar shock wave effects are experienced at equivalent scaled distances, Z, defined as

$$Z = \frac{R}{W^{1/3}}, \tag{1.2}$$

where R is the standoff distance, or distance between a point of interest and the blast epicenter, and W is the charge weight. In the literature, various parameters quantifying the effects of explosive air burst are defined as a function of scaled distance, Z, for a reference explosion. This reference explosion almost always corresponds to a charge weight equal to either 1 kg or 1 lb of TNT.

For explosives other than TNT, the usual approach is to calculate an equivalent weight in TNT for the explosive, W_{TNT}, according to

$$W_{TNT} = \frac{H_{exp}}{H_{TNT}} w_{exp}, \tag{1.3}$$

where w_{exp} is the weight of the explosive, and H_{exp} and H_{TNT} are the heats of detonation for the explosive and for TNT, respectively [11]. In some sources, the ratio H_{exp}/H_{TNT}, which represents the ratio of energy output between a given explosive and TNT, is called the TNT equivalence factor. Values for the heat of detonation for more common explosives are tabulated in Kinney and Graham [41] and Baker et al. [7].

Hopkinson scaling assumes that pressures, temperatures, densities, and velocities are the same at homologous times. Parameter data from the literature, as applied to a given explosion, are then determined by applying a scaling factor to parameter values for a reference explosion at the same scaled distance. The scaling factor is unity for peak overpressures, but times and impulses are scaled by the factor $k = (W/W_{ref})^{1/3}$, where W is the weight (equivalent TNT) of the charge of interest and W_{ref} is the weight of the reference explosion.

1.4 Air blast load generation code

The air blast load generation computer code written as part of the current research determines overpressure profiles at nodal locations within a finite element model for a given explosion scenario. The overpressure time histories are calculated based on Eq. (1.1), and are converted to nodal force time histories using element tributary area. The associated air blast parameters are calculated as a function of scaled distance, angle of incidence, and charge type (spherical or hemispherical). A choice of different blast parameter sources is available for the air blast load computation.

1.4.1 Blast parameters

Values for the parameters describing air blast in Eq. (1.1) can be found in a few different sources. The work of Baker [6, 7] is very thorough, including information about both reflected and side-on air blast cases, but the graphical format of the data is not very conducive to implementation within an air blast loading code. The work of Kingery and Bulmash [40] includes blast data from numerous different tests, both for side-on and reflected cases, and their data is presented in the form of equations as a function of scaled distance. These air blast parameter equations (known as the Kingery-Bulmash equations) serve as the basis for ConWep [33], which is a well-known air blast load generation program. However, it is important to note that both ConWep and the work of Kingery and Bulmash are limited in distribution, only available to the U.S. military and government contractors. Other works [59, 41] include alternative equations for air blast parameters, but do not include complete information, especially regard-

ing reflected air blast. Baker et al. [7] includes detailed information about peak values of shock overpressure, as taken from Brode [18].

Blast parameters following Kinney and Graham and Brode

The air blast parameter equations presented in this section comprise a complete set of parameter equations from open literature sources. The equations are taken from Kinney and Graham [41] and Brode [18], with some modifications and additions.

The duration time, taken directly from Kinney and Graham [41], is given as

$$\frac{t_d}{W^{1/3}} = \frac{980\left[1 + (\frac{Z}{0.54})^{10}\right]}{\left[1 + (\frac{Z}{0.02})^{3}\right][1 + (\frac{Z}{0.74})^{6}]\sqrt{1 + (\frac{Z}{6.9})^{2}}}, \tag{1.4}$$

where t_d is the duration, in seconds, of the positive phase of the blast profile.

Information about the peak overpressure in free air is also taken directly from Kinney and Graham [41], and is defined as

$$P_s = P_{atm}\frac{808\left[1 + (\frac{Z}{4.5})^{2}\right]}{\sqrt{\left[1 + (\frac{Z}{0.048})^{2}\right]\left[1 + (\frac{Z}{0.32})^{2}\right]\left[1 + (\frac{Z}{1.35})^{2}\right]}}, \tag{1.5}$$

where P_s is the peak side-on overpressure in units of bars, and P_{atm} is the atmospheric pressure in bars.

As part of the development of an experimental air blast database, Bogosian et al. [15] tabulated the distribution of blast test data points available for reflected and incident blast parameters. This summary indicated a similar number of available data sets for reflected and for incident overpressure measurements; however, information regarding peak reflected overpressure, P_r, is much harder to find than for incident overpressure in the open literature. All sources

that do include parameter information for reflected overpressures present data for the normally reflected case, with angle of incidence effects treated separately, if at all.

In the far field limit for explosions of any size, or for small explosions, the air can be treated as an ideal gas in order to establish a relationship between the peak side-on overpressure and peak reflected overpressure at a surface. According to Brode [18], this relationship is

$$P_r = P_s\left(2 + \frac{6P_s}{P_s + 7P_{atm}}\right), P_s < \text{ 6.9 bar} \tag{1.6}$$

where P_r is the maximum overpressure for normal reflection, P_s is the peak side-on overpressure, and P_{atm} is the ambient air pressure. An implicit assumption in this equation is that $\gamma = 1.4$, where γ is the heat capacity ratio of the air medium.

When overpressure values exceed 6.9 bar, molecules in the air start to interact with one another and the ideal gas assumption is no longer valid. For this regime, Brode [18] defines the peak normally reflected overpressure as

$$P_r = P_s\left(\frac{0.03851\ P_s}{1 + 0.0025061\ P_s + 4.041 \times 10^{-7} {P_s}^2} + 2 + \ldots \right.$$
$$\left. + \frac{0.004218 + 0.7011\ P_s + 0.001442\ {P_s}^2}{1 + 0.1160\ P_s + 8.086 \times 10^{-4}\ {P_s}^2}\right), P_s \geq \text{ 6.9 bar}, \tag{1.7}$$

where P_s is again the peak side-on overpressure in bars.

Suitable expressions for the decay constant and the arrival time are not included in the works of Kinney and Graham [41] or Brode [18]. Thus, the following equations for arrival time and decay constant are developed by fitting piecewise polynomials to data for a 1 kg TNT reference explosion in Kinney and Graham [41]. The data include arrival times and decay coefficients over a range of scaled distances.

The resulting expression for the arrival time is

$$\frac{t_a}{W^{1/3}} = \sum_{i=1}^{4} a_i \, Z^{i-1}, \, 0.3 \leq Z \leq 500 \text{ m/kg}^{1/3}, \tag{1.8}$$

where t_a is the arrival time, in seconds, of the shock wave initiated by an air blast. Values for the fitted polynomial coefficients, a_i, are included in Table 1.1 for various ranges of Z.

Table 1.1: Fitted polynomial coefficients to define the arrival time.

Range ($\text{m/kg}^{1/3}$)	a_0	a_1	a_2	a_3
$0.3 \leq Z < 2.4$	1.769362e-2	-2.032568e-2	5.395856e-1	-3.010011e-2
$2.4 \leq Z < 12$	-2.251241e+0	1.765820e+0	1.140477e-1	-4.066734e-3
$12 \leq Z \leq 500$	-6.852501e+0	2.907447e+0	9.466282e-5	-9.344539e-8

A higher order of polynomial is required to produce an accurate fit for the decay constant over the range of scaled distances, especially for smaller scaled distances. The decay constant follows this relationship

$$b = \sum_{i=1}^{6} c_i \, Z^{i-1}, \, 0.3 \leq Z \leq 500 \text{ m/kg}^{1/3}, \tag{1.9}$$

where b is the dimensionless decay constant for side-on air blast. Values for the fitted polynomial coefficients, c_i, are shown for different ranges of Z in Table 1.2.

Table 1.2: Fitted polynomial coefficients to define the decay coefficient

Range ($m/kg^{1/3}$)	c_0	c_1	c_2	c_3	c_4	c_5
$0.3 \leq Z < 0.95$	3.08473e+2	-2.14692e+3	5.95329e+3	-8.22603e+3	5.68743e+3	-1.57341e+3
$0.95 \leq Z < 2.4$	1.76074e+1	-2.67855e+1	1.78607e+1	-5.65557e+0	6.94164e-1	0
$2.4 \leq Z < 6.5$	4.43216e+0	-2.71877e+0	7.41973e-1	-9.34132e-2	4.46971e-3	0
$6.5 \leq Z < 40$	7.11610e-1	-6.26846e-2	3.32532e-3	-8.24049e-5	7.61887e-7	0
$40 \leq Z \leq 500$	2.51614e-1	-1.76758e-3	9.51638e-6	-2.19712e-8	1.79135e-11	0

The decay constant is determined from the positive phase impulse, or the area under the pressure time history curve, for either side-on or reflected blast. Kinney and Graham [41] tabulate the decay constant for a wide range of distances, but only for side-on blast. By assuming similarity between time histories of side-on overpressure and normally reflected overpressure, demonstrated by

$$\frac{I_r}{I_s} = \frac{P_r}{P_s}, \tag{1.10}$$

the decay constant can be used interchangeably for side-on and normally reflected cases [7]. While this assumption may introduce error into the prediction of I_r, Baker [6] includes plots of reflected impulse measured experimentally over a wide range of scaled distances, with confidence intervals, and these plots shows that there is an extremely wide range of data for reflected impulse. Considering that there is a lack of reflected data in the literature, the authors determined that the assumption of similarity was an acceptable one.

The above parameter equations for t_a and b are evaluated for goodness-of-fit by using the following error metric based on a normalized ℓ_2 norm,

$$Error = \frac{\| x - x_{dat} \|_2}{\| x_{dat} \|_2} = \frac{\sqrt{\sum_{i=1}^{N} [\,(x)_i - (x_{dat})_i\,]^2}}{\sqrt{\sum_{i=1}^{N} [\,(x_{dat})_i\,]^2}}, \tag{1.11}$$

where $(x)_i$ is the parameter value calculated at scaled distance Z_i using the appropriate parameter equation, $(x_{dat})_i$ is the corresponding parameter value tabulated in Kinney and Graham [41], and N is the total number of scaled distances included in the tabulated data. Error values for each of the parameter equations, as calculated with Eq. (1.11), are 6.63×10^{-4} for P_s, 4.85×10^{-7} for t_d, 3.18×10^{-7} for t_a, and 4.21×10^{-4} for b.

Since similarity has been assumed in air blast profiles for reflected and side-on cases, via Eq. (1.10), then the impulse can be calculated by integrating $P(t)$ in

Eq. (1.1) to get the expression

$$I = \frac{P_{max}\, t_d\, e^{-b}\left(b\, e^{b} - e^{b} + 1\right)}{b^2}, \tag{1.12}$$

where I is either the reflected or side-on impulse, P_{max} is either the reflected or side-on peak overpressure, t_d is the duration time, and b is the decay constant. Upon investigation, fitting the decay constant according to Eq. (1.9) actually provides a better approximation to the side-on impulse data in Kinney and Graham [41], as compared with the equation Kinney and Graham developed from the same data set for side-on impulse,

$$I_s = \frac{0.067\ \sqrt{1 + \left(\frac{Z}{0.23}\right)^4}}{Z^2 \sqrt[3]{1 + \left(\frac{Z}{1.55}\right)^3}}. \tag{1.13}$$

The relative error for calculated I_s values, as compared to the corresponding tabulated data in Kinney and Graham [41], is 3.06×10^{-2} for I_s from Kinney and Graham, Eq. (1.13), and is 1.89×10^{-4} using the fitted equation for b to calculate I_s, Eq. (1.12). Besides the increase in accuracy as compared to tabulated data, using a parameter equation for the decay constant, rather than impulse, is advantageous because this avoids the need for root-solving to calculate the decay constant for each overpressure time history generated by the air blast loading code.

The blast parameter values over a range of scaled distances are summarized in Fig. 1.2. The decay constants are not shown in this figure, but rather are used to calculate values for side-on impulse, I_s, and reflected impulse, I_r, according to Eq. (1.12), for various scaled distances.

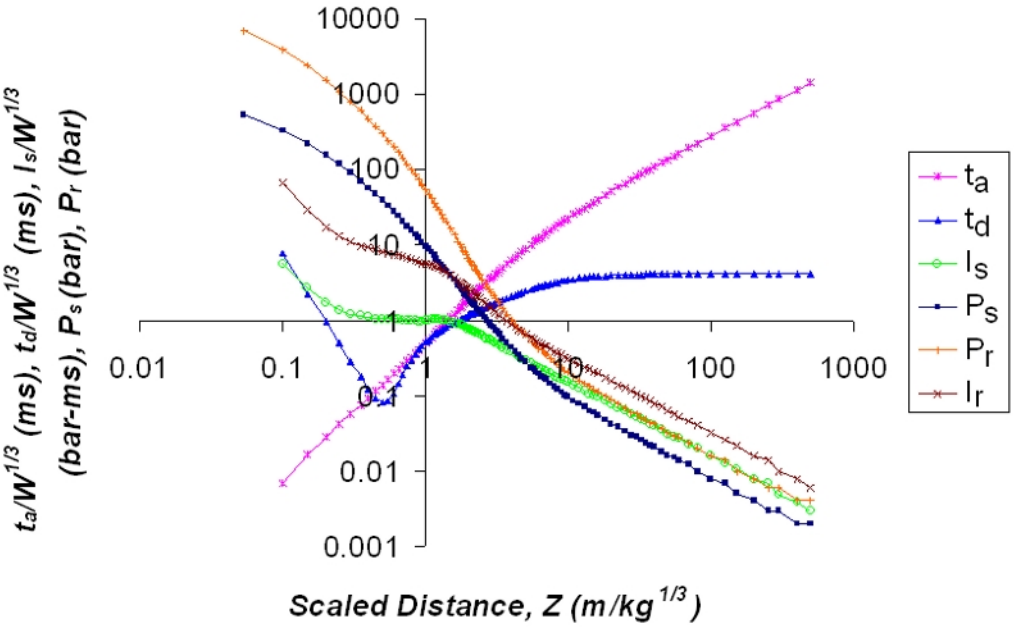

Figure 1.2: Scaled blast load parameters used in air blast loading program.

Blast parameters from Kingery and Bulmash

The approach by Kingery and Bulmash [40] involves numerically fitting functions to data from various explosive tests. The resulting Kingery-Bulmash equations are defined in terms of log-log scaling, and take the form of

$$Y = C_0 + C_1 U + \ldots + C_N U^N \tag{1.14}$$

where

$$U = K_0 + K_1 T. \tag{1.15}$$

In these equations, Y is the common logarithm of the blast parameter of interest (*e.g.* P_r or $t_d/W^{1/3}$), T is the base 10 logarithm of the scaled distance, Z, and N is the order of fit. Values for the coefficients C and K are not available within the

open literature. Thus, while the Kingery-Bulmash equations are widely used by the U.S. military and government contractors, they are not available for research publishable in the open literature.

Blast parameters for design

Numerous sources including military technical manuals, such as *TM 5-1300* [61], and other sources on design [59] suggest a simplification to the decaying exponential blast profile shown in Fig. 1.1. This approach involves approximating the typical overpressure profile with an equivalent triangular pulse. The peak overpressure, P_{max}, and the impulse, I, are preserved but the duration time is modified as

$$t_d' = \frac{2I}{P_{max}}. \tag{1.16}$$

The decay constant, b, is set to zero to give a triangular shape to the blast profile.

Accordingly, the equivalent triangle assumption can be applied to either the currently proposed set of parameter equations (following Kinney and Graham [41] and Brode [18]) or the Kingery-Bulmash equations [40], for use in the air blast load generation code developed for this research.

1.4.2 Angle of incidence

The angle at which a shock wave strikes a structure affects the magnitude of the peak reflected blast overpressure. In fact, there is a complex relationship between the coefficient of reflection, C_r, which is a ratio of the peak reflected overpressure to the peak side-on overpressure, and the angle of incidence, Θ.

As discussed by Chock and Kapania [21], assuming normal reflection is conservative and easier to implement within a blast generation program. However, Randers-Pehrson and Bannister [52] account for angle of incidence effects in their implementation of ConWep into DYNA2D and DYNA3D, an implementation that carries over into the commercial LS-DYNA.

Within their implementation, the reflected blast overpressure profile is a function of both time and angle of incidence and it is a combination of the normally reflected and side-on blast overpressure time histories. Accordingly, the air blast profile, $P(t, \Theta)$, to be applied to an individual finite element at a point in time is calculated as

$$P(t, \Theta) = P_r(t)\ cos^2\Theta + P_s(t)\ (1 + cos^2\Theta - 2\ cos\,\Theta), \tag{1.17}$$

where Θ represents the angle between the normal of an element surface, which includes the point of interest, and a ray between the point of interest and the blast detonation point. $P_r(t)$ is the reflected air blast profile, following Eq. (1.1) with $P_{max} = P_r$, and $P_s(t)$ is the side-on blast profile, which is computed from Eq. (1.1) with $P_{max} = P_s$. To ensure proper air blast load calculation using Eq. (1.17), element normals must point toward (instead of away from) the blast source.

For all of the loading options implemented within the air blast load generation code, the incident impulse is calculated as

$$I(\Theta) = I_r\ cos^2\Theta + I_s\ (1 + cos^2\Theta - 2\ cos\,\Theta), \tag{1.18}$$

where I_r is the impulse for normal reflection, I_s is the side-on impulse, and Θ is the angle of incidence. The duration time for the equivalent triangular parameter equations is a function of this incident impulse,

$$t_d^{'}(\Theta) = \frac{2\ I(\Theta)}{P(t = t_a, \Theta)} = \frac{2\ I(\Theta)}{P_r\ cos^2\Theta + P_s\ (1 + cos^2\Theta - 2\ cos\,\Theta)}, \tag{1.19}$$

where $P(t = t_a, \Theta)$ is the overpressure at the arrival time, from Eq. (1.17), P_r is the peak reflected overpressure for normal incidence, and P_s is the peak side-on overpressure.

However, for the loading approach using the proposed equations, the assumption of similarity in Eq. (1.10) simplifies the incorporation of angle of incidence effects within the developed air blast load generation code. Since $P_r/I_r = P_s/I_s$ and the decay constant is the same for both reflected and side-on air blast, then the incident overpressure time history for the proposed equations can be calculated using the modified Friedlander equation in Eq. (1.1), with

$$P_{max}(\Theta) = P_r \, cos^2\Theta + P_s \, (1 + cos^2\Theta - 2 \, cos\,\Theta), \tag{1.20}$$

where Θ is the angle of incidence, P_r is the peak overpressure for normal reflection, and P_s is the maximum side-on overpressure.

Currently the air blast load generation code employed herein uses the same methodology for estimating angle of incidence effects as the implementation of ConWep in LS-DYNA, from Randers-Pehrson and Bannister [52]. Future work could focus on improving the calculation of P_{max} to account for the Mach stem effect, which is not accounted for in [52].

1.4.3 Hemispherical blast

Explosions located at the ground surface are categorized as hemispherical blast. In *TM 5-1300*, there are separate sets of parameters for spherical and hemispherical blast [61]. However, these parameters are presented in graphical form and were drawn from sources not available in the open literature. Thus, for the

current research the magnification factor approach [6, 40, 59] described subsequently has been employed.

When a charge is detonated at the ground surface, simultaneous reflected waves from the ground are produced, reinforcing the shock wave generated by the initial explosion. If the ground were a perfect reflecting surface, this magnification effect would be equivalent to the shock produced by a charge twice the weight of the actual explosive. However, experimental data indicate that the magnification factor should be less than two (but more than one) because the ground absorbs energy for surface bursts. In fact, a magnification factor of 1.8 is suggested by multiple sources [6, 40, 59], and is employed within the air blast load generation code developed for this research. Accordingly, the approach for hemispherical blast is exactly the same as for spherical blast, except that the charge weight W is replaced by $1.8\,W$.

1.4.4 Shielding effects

For explosive air burst on structures with more complex geometries than a single flat surface, shielding and wave diffraction affect the applied load distribution. Shielding is a function of component geometry and blast location. In this research, shielding effects are incorporated into the blast load generation code using a ray tracing technique to determine which surfaces of a structure are in direct line of sight to an explosion.

Accordingly, fully reflected air blast loads are applied to regions with an unobstructed path from detonation source point to structural boundary. However, in regions of a structural surface that are not in direct line of sight to an explosion, the loading situation is much more complex, especially in the vicinity of sharp corners [13]. Shock waves diffract around corners, and so while the air is compressed above atmospheric pressure at the surface beyond a corner, the overpressure here does not reach fully reflected levels. Applying fully reflected loading to this region would be very conservative, although not applying any loading at all would not be representative of the physical situation. Thus, in areas of a surface partially shielded by another part of the structure, the air blast load generation code models the magnification of the surrounding overpressure with an applied blast loading corresponding to the side-on, or free air, overpressure.

As an example, Fig. 1.3 illustrates a wide-flange member subjected to an explosion where the bottom flanges partially shield some of the explosive effects. Here, the load generation code would determine which nodes are shielded by tracing rays from the blast epicenter to the edges of the bottom flange and then extending these rays to any intersections on the web or top flange surfaces. Reflected air blast loading would then only be applied to regions of the member that are not shielded from the initial shock wave: the bottom surface of the bottom flanges, the bottom surface of the top flanges nearest the blast, and the upper portion of the web on the side facing the blast, as shown in Fig. 1.3. The lower part of the girder web facing the explosion is partially shielded from the blast, and in this region side-on overpressure loading would be applied. As further explanation, the side-on overpressure is the blast loading observed as an explosive shock wave travels past a stationary point in free air, whereas re-

flected overpressure is the much larger loading observed at a point on a rigid surface as a shock wave strikes and reflects off of the surface. While the numerical example presented later in this paper – a wide-flange member subjected to an explosion centered on mid-span and mid-height – does not exhibit shielding, the present discussion of shielding is included herein for completeness.

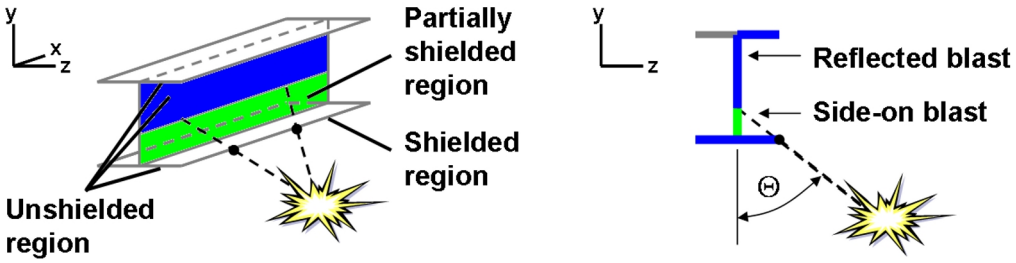

Figure 1.3: Schematic of shielding effects included in air blast loading program.

Although shielding is incorporated into the airblast loading code as described above, pressure relief and clearing effects are not accounted for within the current code. Pressure relief occurs after a reflected blast wave reaches a free edge of the reflecting surface. Physically, when an explosive shock wave impacts a flat surface, pressure is built up by the sudden constraint of flow at the surface, magnifying the blast overpressure here and creating a reflected wave that travels along the structural surface. When the reflected wave reaches a free edge a sudden air flow takes place between high and low pressure regions, creating a rarefaction wave that propagates away from the free edge and back towards the interior of the structural surface. This rarefaction wave acts to relieve the surrounding overpressure from a higher reflected level to a lower stagnation overpressure value. At a point on the surface, this would be modeled by a marked decrease in the air blast overpressure time history after the clearing time, or time when the rarefaction wave reaches the point of interest.

Pressure relief is not included in the air blast loading code because the literature does not provide a universally accepted model of pressure relief. Many sources, including *TM 5-1300* [61], Kinney and Graham [41], and Baker et al. [7], differ in their calculation of the clearing time. Also, while the method for modeling pressure relief in *TM 5-1300* has been used in practice for many years, recent research by Rickman and Murrell [53] casts doubt onto the accuracy of this approach. Rickman and Murrell [53] performed several small-scale experiments to measure reflected overpressure values at various points of a rectangular structure subjected to various hemispherical explosions. Their data show that the calculation of clearing time and stagnation pressure provided by *TM 5-1300* [61] is inaccurate, and they propose new equations for modeling the stagnation pressure, derived from regression analysis of their experimental data. While these curve fits provide a much better approximation for the reflected air blast loading, they were not incorporated in the developed air blast loading code as these equations were determined for a range of scaled distances from $Z = 1.82$ to 12.18 $\mathrm{m/kg^{1/3}}$, whereas the air blast code was developed for a range of $Z = 0.32$ to 500 $\mathrm{m/kg^{1/3}}$. While the latter portion of the range of scaled distances in the code is not really of engineering significance, the closer range is of extreme interest and in fact both examples presented herein fall in this range.

Another assumption made within the paper is to neglect any loading effects on the far faces of a structural surface. In reality, for a structure such as a wide-flange beam, the shock wave from an explosion would almost certainly immediately engulf the structure, imposing positive overpressure on the front faces that would be partially offset by the portion of the shock that wraps around the structure to the back faces. While this is an important physical effect, it is extremely difficult to model with any degree of accuracy. Thus, the loading ef-

fects on the far surfaces of structural faces are neglected by the code, inducing a measure of conservatism into model results.

1.4.5 Code Flow

The developed air blast load generation code essentially works as a preprocessor to a commercial finite element package such as LS-DYNA [31] or ADINA [1]. The code proceeds as shown in Fig. 1.4. Inputs to the code are the finite element mesh; explosion type, size, and location; and flag for type of loading. The loading flag corresponds to various sets of parameters available for use in describing the air blast loading including the currently proposed set of equations, the equivalent triangular version of these, the Kingery-Bulmash equations, or the equivalent triangular version of Kingery-Bulmash equations.

There are a few important differences between the developed air blast generation code and the implementation of ConWep in LS-DYNA. Since the air blast code acts as a preprocessor, it is portable to other finite element software packages besides LS-DYNA and it produces loading data that can be analyzed to get an idea of the loads at various locations in a model. However, the implementation of ConWep in LS-DYNA is strictly internal, and only provides the reflected overpressure and arrival time for the node of the structural model first affected by an explosion. The proposed air blast load generation tool can provide loading with air blast parameters derived from open literature sources, whereas ConWep is based on the Kingery-Bulmash equations, which are not openly available. Finally, the air blast loading code includes a shadowing algorithm to determine which components are in direct line-of-sight to an explo-

sion, applying fully reflected loading to these regions and side-on blast loading to partially shielded surfaces.

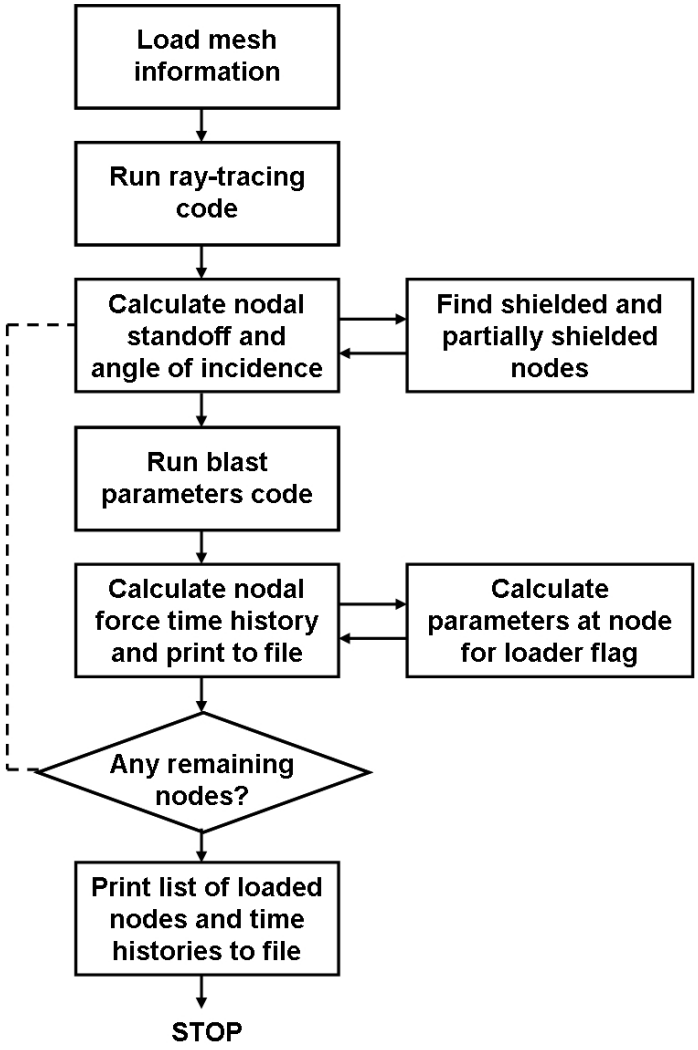

Figure 1.4: Air blast loading code flow chart.

1.5 Case studies

Two case studies are presented for investigating the effects of air blast modeling on structural response. The plate model includes a spatially uniform application

of loading (*i.e.* a plane wave), in order to isolate the effect of different parameter values for a single scaled distance. The girder model includes the full range of angle of incidence effects as well as a temporally and spatially varying loading.

1.5.1 Loading

For both of the case studies presented, air blast loading is applied over the structural surfaces using the air blast load generation code. Loads are applied as nodal force time histories within the finite element models. There are four separate cases of loading considered for each structure:

1. Currently proposed set of equations – *Current*
2. Equivalent triangular version of *KG* – *Current-Tri*
3. Kingery-Bulmash equations – *KB*
4. Equivalent triangular version of Kingery-Bulmash equations – *KB-Tri*

1.5.2 Material model

The extreme nature of explosive loading necessitates the inclusion of nonlinear effects for accurate simulations of structures subjected to explosions. This includes not only nonlinear kinematics but also the consideration of rate-dependent material behavior. The commercial finite element package, LS-DYNA, is a transient dynamic nonlinear finite element code with an availability of numerous nonlinear material models [45]. Given its wide usage in air blast simulations, LS-DYNA is used as the finite element solver for this research.

A well-known model for rate-dependent material behavior is the Johnson-Cook model [34, 35]. The Johnson-Cook constitutive relationship is expressed as

$$\sigma_{flow} = \left[A + B\left(\varepsilon_{ep}\right)^{n}\right]\left[1 + C\, ln\, \dot{\varepsilon}^{*}_{ep}\right]\left[1 - (T^{*})^{m}\right], \tag{1.21}$$

where σ_{flow} is the flow stress, ε_{ep} is the effective plastic strain, $\dot{\varepsilon}^{*}_{ep} = \dot{\varepsilon}_{ep}/\dot{\varepsilon}_{0}$ is the dimensionless plastic strain rate, T^{*} is the homologous temperature, and A, B, n, C, and m are material constants. Note that $\dot{\varepsilon}_{0}$ is the quasistatic strain rate used in experiments to determine the static strain hardening parameters, B and n.

As part of the present research, a weak form of the heat equation was solved to investigate the spatio-temporally varying temperature field within a representative 12.7 mm thick steel plate component subjected to a thermal loading that was consistent with an open air blast. Based on results from this analysis, heating effects were deemed not to be of concern to the girder and plate problems modeled in this research. Accordingly, ignoring the temperature term gives the simplified version of the Johnson-Cook model used in this research, which is

$$\sigma_{flow} = \left[A + B\left(\varepsilon_{ep}\right)^{n}\right]\left[1 + C\, ln\, \dot{\varepsilon}^{*}_{ep}\right]. \tag{1.22}$$

In this form, the flow stress is the product of a strain hardening term, $\left[A + B\left(\varepsilon_{ep}\right)^{n}\right]$, and a viscoplastic term, $\left[1 + C\, ln\, \dot{\varepsilon}^{*}_{ep}\right]$.

Johnson-Cook model parameters for a mild steel (SS 141672), as reported by Kajberg and Wikman [36], are used to model the constitutive behavior for the case studies considered herein. Material constants used for this steel are E = 209 GPa, ν = 0.3, and ρ = 7850 kg/m^3 [4] for the plate and E = 203 GPa, ν = 0.3, and ρ = 7850 kg/m^3 for the girder. The Johnson-Cook parameter values, determined using a split Hopkinson bar test, high-speed photography, and optimization

techniques, are reported to be $A = 319$ MPa, $B = 554$ MPa, $C = 3.27 \times 10^{-2}$, $n = 0.135$, $\dot{\varepsilon}_0 = 5.7 \times 10^{-3}$ s^{-1} [36].

1.5.3 Square plate

The first case study involves a square steel plate subjected to a spherical explosion. The plate is 914 x 914 x 3.18 mm (36 x 36 x 1/8 in), with fixed boundary conditions on the vertical edges and free boundary conditions along the horizontal edges. A charge of 1.36 kg (3 lb) TNT is centered on the plate, located at a minimum standoff distance of 1.52 m (5 ft), corresponding to a minimum scaled distance of $Z = 1.37$ kg/m^3. Because of the symmetry in loading and boundary conditions, only 1/4 of the plate is modeled for computational expediency. An overview of the model setup is shown in Fig. 1.5.

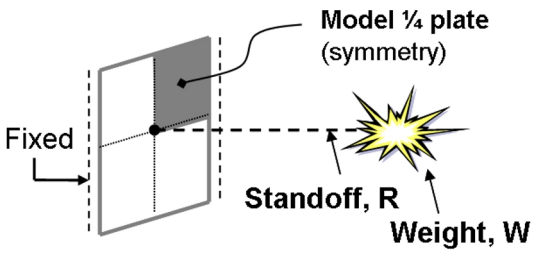

Figure 1.5: Plate model setup.

Explicit time integration is utilized in the solution, along with large strain, large displacement kinematic assumptions. An automatic time-stepping scheme uses the Courant condition to limit step size, producing time steps on the order of 1 μs. The dynamic analysis is carried out to a total solution time of 200 ms, with mass damping (5%) applied after 100 ms in order to yield the fi-

nal deformed shape of the plate by the end of the analysis. The plate is modeled with Belytschko-Lin-Tsay shell elements with five through-thickness integration points, where a global mesh seed of 4.57 mm is applied. The Belytschko-Lin-Tsay element employs one-point quadrature in the plane of the element and uses empirical parameters to suppress the hourglass deformation modes [31]. Standard viscosity-based hourglass control in LS-DYNA is used, with membrane, bending, and warping hourglass coefficients equal to 0.10. The employed mesh was arrived at by way of a mesh convergence study.

1.5.4 Girder

The second case study examines the response of a steel wide-flange member to explosive air burst. The girder is a W360x122 (W14x82) section, 4.57 m (15 ft) long, with simply supported boundary conditions. The investigated air blast scenario involves a spherical explosion of 453.6 kg, centered on the girder and located 4.57 m (15 ft) away from the point at mid-span, mid-height of the girder. This blast scenario corresponds to a minimum scaled distance of $Z = 0.60$ kg/m^3. Fig. 1.6 illustrates a schematic of the girder model.

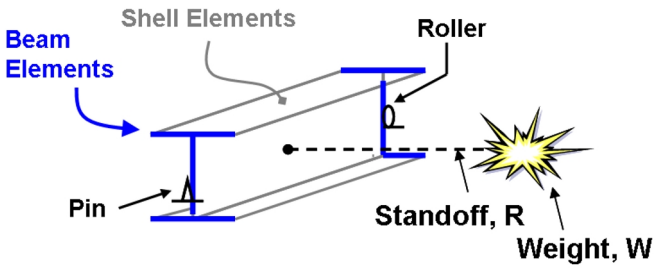

Figure 1.6: Girder model setup.

The girder is modeled with a combination of elements. Belytschko-Lin-Tsay shell elements, defined along the girder midline geometry with element thickness equal to the girder plate thicknesses, comprise the body of the girder. Cross-sectional distortion at the support locations is suppressed by placing very stiff beam elements along the middle lines of the end cross-sections. These beam elements employ the Belytschko-Schwer resultant formulation [31], and are circular in cross-section with a diameter of 25.4 mm. The material used for the beam elements is perfectly elastic, with $E = 20,300$ GPa and $\nu = 0.3$. A mesh seed of 21.4 mm, or 6 elements per flange outstand, applied globally to the model, provides sufficient resolution to capture local deformation effects induced by the explosion, as evidenced by a mesh convergence study.

A dynamic analysis is carried out to a total solution time of 1000 ms. Mass damping (5%) is applied after 500 ms to yield the final deformed shape of the girder by analysis completion. Explicit time integration with automatic time-step calculation is used, producing time steps on the order of 3 μs. To ensure a uniform critical time step size throughout the model, the density of the beam elements is adjusted so that the global model critical time step size is similar for both the shell and beam elements. Accordingly, $\rho = 380\,\rho_{shell} = 2983 \times 10^3$ kg/m^3, where ρ_{shell} is the density of the shell elements.

1.6 Results and discussion

1.6.1 Comparison of Overpressure Profiles

Air blast overpressure profiles calculated using the four different methods, outlined at the beginning of Section 4, are examined. The main comparisons are made between Kingery-Bulmash versus the proposed parameters developed from Kinney and Graham [41] and Brode [18], and between each of these versus their equivalent triangular counterparts. Since the parameter equations draw from different data sets, with only some overlap, it cannot be definitively determined which approach is more correct without access to further explosives test data.

For the loading applied to the plate model, a spherical explosion of $W = 1.36$ kg of TNT, at a standoff of $R = 1.52$ m is employed. Parameter values for the different approaches are summarized in Table 1.3. Fig. 1.7 shows the air blast overpressure time histories developed using the four different methods.

Table 1.3: Air blast parameters for $R = 1.52$ m and $W = 1.36$ kg

Loading	t_a (ms)	t_d (ms)	$t_a + t_d$ (ms)	P_{max} (bar)	I_r (bar-ms)
Current	1.033	0.891	1.924	5.197	22.15
Current-Tri	1.033	0.469	1.502	5.197	22.15
KB	1.072	1.890	2.962	4.124	19.52
KB-Tri	1.072	0.423	1.495	4.124	19.52

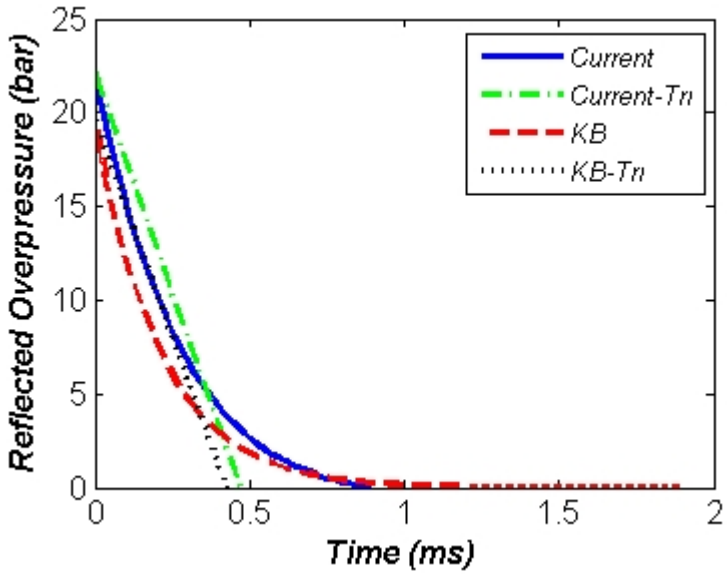

Figure 1.7: Comparison of overpressure profiles for R = 1.52 m, W = 1.36 kg.

The largest difference between the loading produced by the proposed equations and the Kingery-Bulmash equations is seen in the load duration, which is not surprising given the amount of scatter in experimental data for air blast duration time that is shown in figures in Baker [6]. When comparing each approach with their triangular equivalents, the most significant difference is seen in the Kingery-Bulmash results since there is such a long tail in the air blast profile produced using this method.

One measure of the differences in air blast overpressure profiles produced by the four approaches is a comparison of their frequency spectrums. Fig. 1.8 highlights the frequency spectrums, which are calculated with fast Fourier transforms (FFT), for the different parameter sets at R = 1.52 m and W = 1.36 kg. Two universal trends are noteworthy, the first being that the energy in the air blast loading is spread over a wide range of frequencies, and the second that since the decaying exponential (or equivalent triangle) is not a periodic function, the

largest amount of energy is concentrated at zero frequency on the FFT plot.

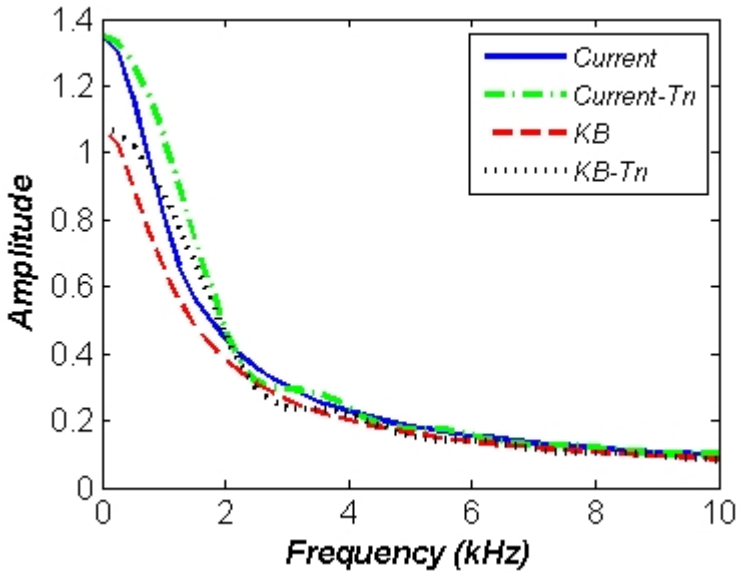

Figure 1.8: Comparison of frequency content of air blast loading for R = 1.52 m, W = 1.36 kg.

Closer examination of the frequency content between the specific loading approaches yields a few differences. Since the pulse form for the equivalent triangular approaches varies from their unmodified counterparts, the frequency content of the loading applied to a structure varies slightly. A larger relative difference is seen between the frequency spectrums of the blast profiles for the proposed parameter equations and the Kingery-Bulmash equations. The amplitude of the frequency spectrum of the overpressure loading from the Kingery-Bulmash approach is smaller than that from the proposed equations, a function of the diminished peak overpressure and reflected impulse of the air blast profile from the Kingery-Bulmash equations, as compared with the profile from the proposed equations. However, it is important to note that although the discrepancies in frequency content of overpressure loading produced by the four

approaches appear relatively minor within this context, any variation in the frequency content of input loading will lead to differences in simulated structural response time histories.

A detailed comparison is not made between the air blast overpressure profiles that comprise the full spatio-temporal loading for the girder problem. However, the parameter values are reported for the loading at the girder point closest to the explosion (at mid-height and mid-span). At this minimum stand-off distance of R = 4.57 m, for the charge weight of W = 453.6 kg, the parameter values produced by the different loading approaches are shown in Table 1.4.

Table 1.4: Air blast parameters for R = 4.57 m and W = 453.6 kg

Loading	t_a (ms)	t_d (ms)	$t_a + t_d$ (ms)	P_{max} (bar)	I_r (bar-ms)
Current	1.462	0.816	2.278	57.32	212.34
Current-Tri	1.462	0.540	2.002	57.32	212.34
KB	1.595	3.723	5.318	87.01	201.93
KB-Tri	1.595	0.862	2.457	87.01	201.93

1.6.2 Plate example

Of interest in most explosion simulations is the maximum deformation induced in a structure by a blast. In the plate problem, the peak displacement caused by an air blast occurs at the center of the plate. Accordingly, Fig. 1.9 shows the transverse displacement results at the center node of the plate for the various loading approaches considered herein. While the results appear similar in the first few cycles of response, they diverge soon after that as the plate starts to plastically deform.

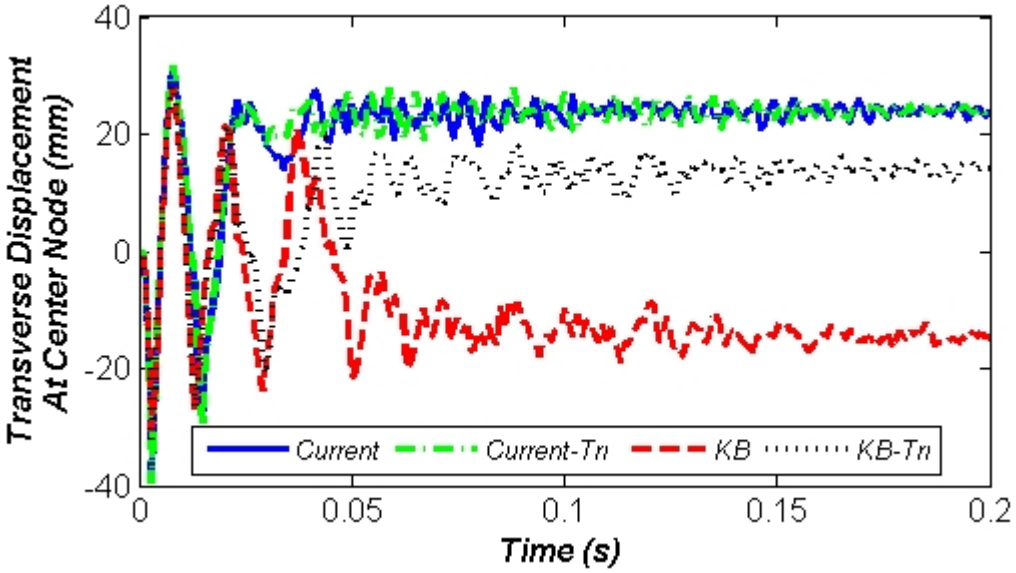

Figure 1.9: Comparison of plate transverse displacement at center.

As an illustration of the differences seen in the displacements at a later time after the explosion, transverse displacement results at a specific snapshot in time are examined for the different loading cases. The metric for comparison is the transverse displacement profile along the horizontal centerline of the plate at t = 200 ms. The profile location is illustrated in Fig. 1.10 and the resulting plate transverse displacement profiles for the four loading methods are included in Fig. 1.11.

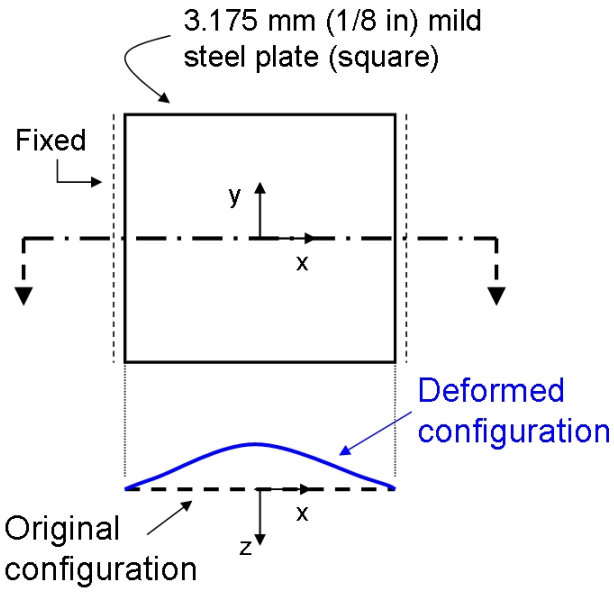

Figure 1.10: Schematic of plate center displacement profile.

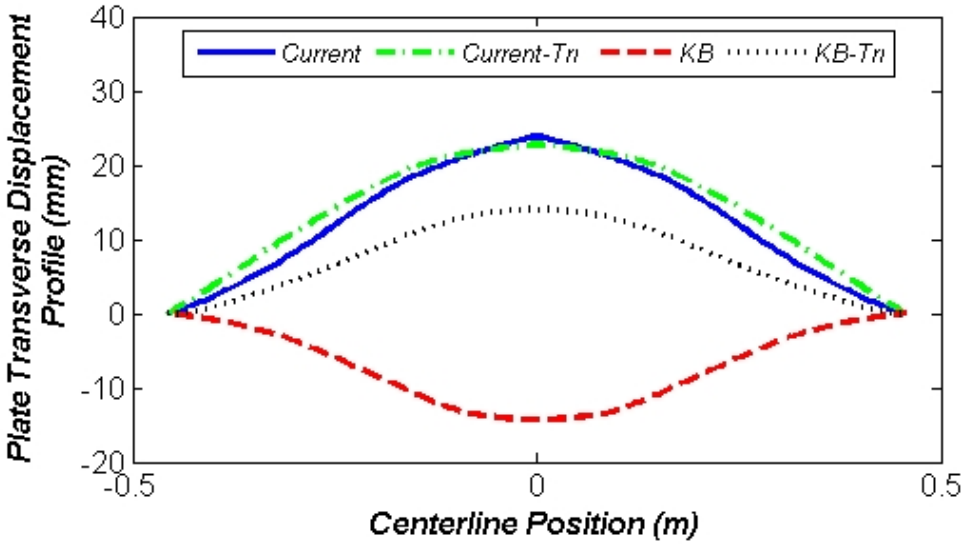

Figure 1.11: Comparison of plate center displacement profiles at t = 200 ms.

It is interesting to note that for all of the load approaches except the one using the original Kingery-Bulmash equations, the plate response settles to a permanently deformed configuration that is toward, instead of away from, the explosion epicenter. While this seems counterintuitive, it is not the first time this type of result has been documented. In their investigation of the response of thin circular aluminum plates subjected to a spatially uniform square pulse loading, Bassi, Genna, and Symonds [8] observed permanent deformation pointed toward the direction of loading. They indicated that for very thin, elastic-perfectly plastic plates with fixed boundary conditions, there exist small ranges of loading parameters for which the plate deforms towards the loading in the early stages of response, and then does not have enough energy left to subsequently snap back away from the loading source. It seems that a similar situation is seen in these results, for a thin plate of a Johnson-Cook material subjected to exponentially decaying and triangular pulse loadings.

Another metric for comparison between the plate responses is a normalized ℓ_2 norm similar to the form in Eq. (1.11). The error is calculated as

$$\frac{\| {dz_{Case1}}^t - {dz_{Case2}}^t \|_2}{\| {dz_{Case1}}^t \|_2} = \frac{\sqrt{\sum_{i=1}^{N} \left[({dz_{Case1}}^t)_i - ({dz_{Case2}}^t)_i \right]^2}}{\sqrt{\sum_{i=1}^{N} \left[({dz_{Case1}}^t)_i \right]^2}}, \tag{1.23}$$

where $({dz_{Case1}}^t)_i$ is the transverse displacement at node i along the plate centerline at time $t = 200$ ms for load case number 1, N is the number of nodes along the plate centerline and $({dz_{Case2}}^t)_i$ is the transverse displacement at the same time and location for case number 2. Load cases and error results are summarized in Table 1.5.

Table 1.5: Relative error between plate transverse displacement profiles at t = 200 ms.

Case 1	Case 2	Error, $\frac{\| dz_{Case1}{}^t - dz_{Case2}{}^t \|_2}{\| dz_{Case1}{}^t \|_2}$
Current	*Current-Tri*	0.013
KB	*KB-Tri*	3.971
Current	*KB*	7.195

The error calculation is greatly affected by the fact that the final deformed configuration of the plate that was loaded with an explosion modeled using the Kingery-Bulmash equations is pointed away from, rather than toward, the blast, in contrast to the other cases. If this profile were flipped so that it faced toward the blast instead, the measured error would change from 3.971 to 0.002 for the second comparison in Table 1.5 and it would change from 7.195 to 0.480 for the third case. However, it is important to preserve the direction of plate transverse deformation when comparing the actual final deformed shapes since this direction will be important to plate stability under certain structural configurations, such as those experiencing eccentric loading.

1.6.3 Girder example

In the girder problem, the peak transverse displacements are located at girder mid-height and mid-span. Fig. 1.12 compares the nodal transverse displacement results at this location on the girder for the different blast loading methods. The transverse displacements produced by the proposed equations developed from Kinney and Graham and Brode match closely with the displacements

produced by the corresponding triangular equivalent loading. However, larger differences are seen between the Kingery-Bulmash and equivalent triangular Kingery-Bulmash results, and especially between both sets of Kingery-Bulmash results and the responses induced by the currently proposed air blast loading equations.

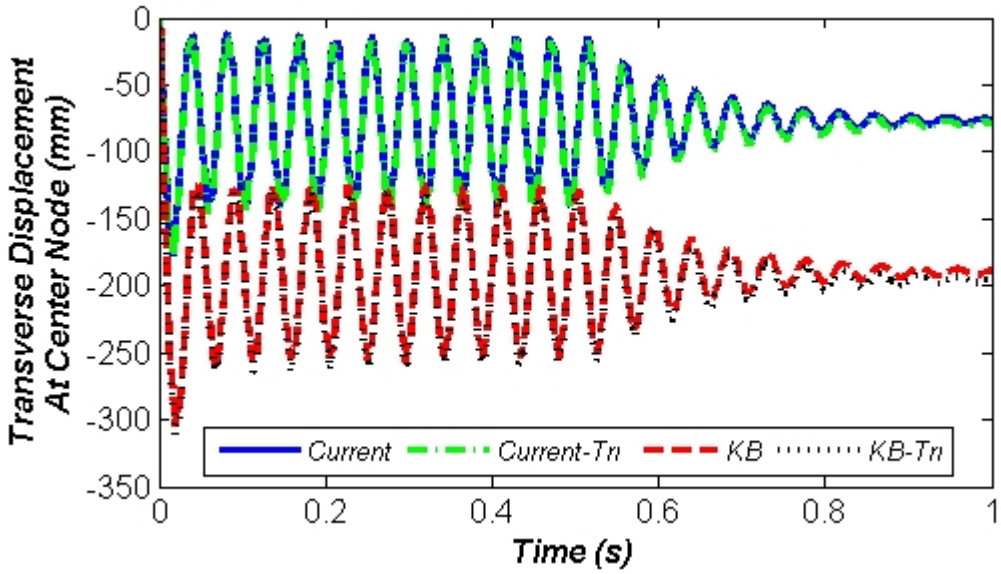

Figure 1.12: Comparison of girder transverse displacement at mid-height, mid-span.

Fig. 1.13 depicts a representative result of simulated girder deformation induced by the explosion. This contour plot of averaged accumulated effective plastic strain represents the girder response at t = 1 s for the equivalent triangular Kingery-Bulmash loading. Two main features are noteworthy, the permanent set in the web away from the blast, and the deformation within the compression flanges nearest the detonation epicenter.

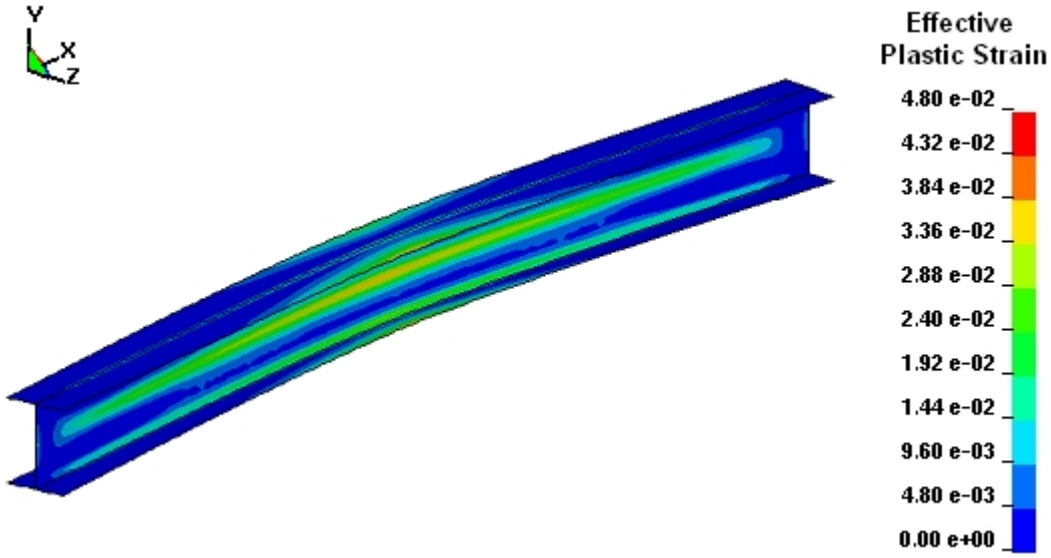

Figure 1.13: Contours of accumulated effective plastic strain at t = 1 s.

Further examination of the flange vertical displacement is warranted since the magnitude and location of localized deformations oftentimes greatly affects the global capacity of a structural member within a system. In Fig. 1.14, the y-displacements at each node along the top flange edge nearest the blast are compared for the different loading cases at t = 1 s, long after the plastic strains have stopped changing in this region. These results take the form of displacement profiles along the girder top flange edge, which clearly show regions of localized deformation.

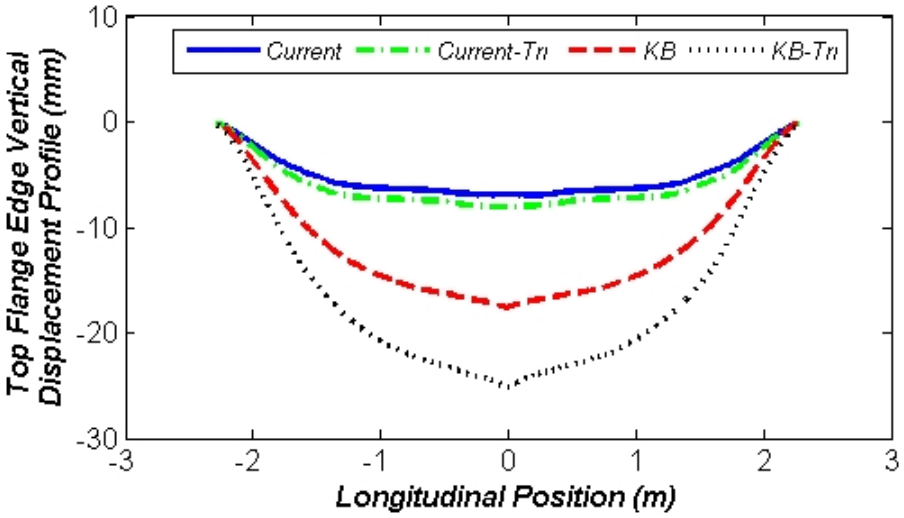

Figure 1.14: Comparison of girder flange edge displacement profiles at t = 1 s.

A quantitative comparison of the displacement profiles can be made with an ℓ_∞ norm, or

$$\| dy \|_\infty = \max_{i=1}^{N} (| dy_i^t |), \tag{1.24}$$

where dy_i^t corresponds to the y-displacement at the nodes along the top flange edge nearest to the blast at time t = 1 s, and N is the number of nodes. The peak vertical displacements are 17.6, 25.3, 7.0, and 8.1 mm for the Kingery-Bulmash equations, the Kingery-Bulmash triangular equivalent, the proposed equations developed from Kinney and Graham and Brode, and the triangular equivalent of the proposed equations, respectively. The peak flange displacement occurs near midspan for all loading methods, in spite of their relative similarities. Similar to the plate case study, the four different load approaches produce significantly different results. In terms of relative comparisons, the peak displacements are closer in magnitude for the equivalent triangular pulse loading, as compared with their parent parameter equations, than they are between the Kingery-Bulmash and the proposed parameter cases.

The flange displacement profile is more exaggerated for the cases with Kingery-Bulmash types of loading than those loaded by a variant of the proposed parameters from Kinney and Graham and Brode. At first glance, it would seem that this is purely due to the substantial difference in predicted reflected impulse between these loading approaches. However, parameter studies on the research presented herein, and numerous sources in the literature [47, 59, 7], show that there is a strong interrelationship between pressure and impulse, and so the difference in structural response cannot be traced to either of these parameters acting in isolation. In fact these results clearly show that duration time is also important to response, since there is such a wide range between the deformation caused by the Kingery-Bulmash loading as compared to its triangular equivalent. While discussing differences, it is important to note that the Kingery-Bulmash loading and the proposed set of parameter equations emanated from different empirical data sets for open air blast tests. It is expected that variations within these tests plays a significant role in precipitating some of the differences highlighted earlier.

1.7 Conclusions

Structural vulnerability to acts of terrorism has received increasing attention in the past few years. A first step toward accurate simulation of structural response to different explosion scenarios is to establish suitable models of loading. To this end, this research presents a complete set of parameter equations to describe external air blast loading for a structure, based on open literature sources [41, 18]. The proposed air blast parameters are notable in that they are drawn from data available in the open literature and that they are in equation, rather

than graphical form. These parameters, together with alternative parameter methods (the Kingery-Bulmash equations, and equivalent triangular pulses), have been implemented within an air blast load generation code written for this research. This code improves upon other codes in its inclusion of a shadowing algorithm for determination of unshielded and partially shielded structural surfaces, and its application of side-on, rather than fully reflected, blast to surfaces partially shielded from explosive air burst. Additionally, given its open literature sources, all assumptions and limitations within the proposed approach are available for critical review by the analyst/designer.

The proposed blast load generation code is used to provide loading representing each set of parameters in finite element simulations of a steel plate and a wide-flange girder subjected to an explosive air burst. Results obtained by coupling the currently developed air blast load generation code with LS-DYNA illustrate that small changes in blast loading parameter definition can have a significant effect on structural response time histories. Since small details have such a large effect on structural response for air blast phenomena, there is a clear need for further research to better assess the unavoidable uncertainty that is inherent in air blast loading.

1.8 Acknowledgment

This material is based upon work supported under a National Science Foundation Graduate Research Fellowship. Any opinions, findings, conclusions or recommendations expressed in this publication are those of the author and do not necessarily reflect the views of the National Science Foundation.

CHAPTER 2

SIMULATING BLAST EFFECTS ON STEEL BEAM-COLUMN MEMBERS: METHODS

2.1 Abstract

A beam-column element is formulated and implemented within a nonlinear explicit dynamic finite element code to be used for simulating explosive effects in steel skeletal structures composed of wide-flange members. The damage imposed by a blast is encapsulated by a bounding surface plasticity model in stress-resultant space. These bounding surfaces are formed by fitting numerical failure data to a basis of real-valued spherical harmonics: the needed data are obtained through a series of numerical experiments in which a shell element-based model of a member is first exposed to a blast and then is statically loaded to failure for various combinations of proportional moment-thrust loading. A comparison of undamaged and blast-damaged bounding surface data for a variety of blast locations demonstrates the effects of an explosion on the reserve capacity of a member. Code validation and examples are presented in a companion paper [29].

2.2 Introduction

Over the last decade, the proliferation of terrorist attacks on structures has generated much concern. Damage caused by explosive attacks has exposed a general vulnerability to blast in many conventionally designed structures, with lo-

calized blast damage triggering global failure in some cases [23]. While many complex analysis tools exist for the assessment of blast effects on structures, an openly available, computationally efficient approach to this problem is needed in general structural engineering practice (*i.e.* structures other than military facilities, embassies, etc.).

Under the influence of an explosion, hot-rolled steel wide-flange members are susceptible to coupled lateral-torsional buckling and localized damage that may influence system-wide structural stability. The need to examine the post-blast behavior of a structure motivates the use of structural elements, such as frame elements. However, it can be difficult to capture the salient physics within a one-dimensional frame element idealization. As an alternative, high-resolution models of structures that use shell or continuum element discretization of individual structural components, in uncoupled or coupled analyses, are able to accurately predict member response to an explosive event. However, models of this type require a high level of expertise and are computationally expensive, especially for larger structural systems. Thus, one of the objectives of the current research is to formulate a beam-column element, based on a traditional frame element, that is able to accurately and efficiently predict the remaining capacity in a steel structural system exposed to an explosion. Along these lines, a method is proposed for modeling the reserve capacity of blast-damaged structural members using bounding surface plasticity models, or bounding surfaces, to capture the effects of component-level damage, in order to enable the application of frame elements in the study of blast-damaged systems.

Each bounding surface is developed from a large set of numerically generated failure data (as obtained from a high-resolution shell element model) for

a wide-flange member that has been damaged by a given explosion and subsequently loaded to collapse. While this data-driven approach to bounding surface modeling within the element formulation does exact a substantial up-front computational cost, this is a small price to pay for the savings in computational time when comparing the finite element code employing the blast beam-column element and an analysis using a high-resolution model.

This paper is the first of two companion papers to formulate, implement, and validate a beam-column element for the simulation of air blast effects in steel skeletal structures with wide-flange components. The element formulation and implementation is included herein, and the validation and examples are presented in the companion paper [29].

2.2.1 Literature review

Within a frame element formulation, bounding surface plasticity models, which are defined in stress-resultant space, are adapted from traditional stress-space plasticity to model inelastic cross-section deformations in response to combined axial loading and biaxial bending. Formulations employing bounding surface plasticity models have been the focus of research since the 1970's. Research directly leading to the traditional frame element formulation that serves as the basic framework of the current blast beam-column element includes the work of Porter and Powell [50], Orbison et al. [49], Hilmy and Abel [32], and Powell and Chen [51]. Additionally, the work of Deierlein and El-Tawil [25] is useful in that it provides an in-depth discussion of bounding surface plasticity models, although the two-surface bounding surface model developed in their research is

not used herein. The work of Orbison et al. [49] is notable in that their model of the bounding surface for a steel cross-section uses a single continuous, smooth function, an approach that is adopted in modeling the bounding surface for the blast beam-column element. The version of the traditional frame element formulation used as the point of departure in the current research is taken from McGuire et al. [48], and is included in a subsequent section.

Recognizing that bounding surfaces tend to be of a phenomenological nature, it is important to have an understanding of the structural behavior exhibited by blast-damaged frame members. Research regarding the modeling of blast effects on steel frames is limited. Bogosian et al. [14] develop a method to assess the collapse resistance of a steel frame building to the explosive threat from a failed space launch using a physics-based, computationally efficient approach. They incorporate an aggregate load-deflection curve, developed from static collapse analyses of a full building subjected to linearly increasing pressure loading carried out in ADINA, as a resistance function in an equivalent (SDOF) model, which is used to evaluate the peak response induced by a far-off explosion, modeled as a planar wave, on the structure for numerous extremely large explosive weights.

Other work has focused on modeling the response of steel frame structures subjected to explosions and ensuing fire, including that of Song et al. [60] and Chen and Liew [20, 44]. Song et al. [60] develop an approach to carry out nonlinear analyses of steel frames exposed to fire and blast, in isolation or in combination, where their code adaptively remeshes a structural system as needed, replacing the initial elastic macro-elements with smaller elasto-plastic elements.

Chen and Liew [20] use a mixed element approach to analyze steel frame structures subjected to a localized explosion that is followed by fire, where members far away from the blast are modeled with beam elements, and those closer to the blast are modeled using shell elements. Liew [44] presents results demonstrating the deficiencies associated with modeling a wide-flange member under explosive loading by using traditional beam elements or single degree-of-freedom (SDOF) methods. In a numerical example, a multi-story building is exposed to a 1000 kg (2205 lb) TNT explosion located 5 m (16.4 ft) from the front of the first story of the building, where the explosive loading is produced using the implementation of ConWep [33] in LS-DYNA [52], and the building response is simulated using a mixed element approach that builds upon the work in [20].

In both [60, 20], it is important to note that the blast overpressure loading is applied to members in a spatially uniform manner, in contrast to the spatially varying load application employed by the current research [28]. While more recent work by Liew [44] includes spatial and temporal variation in blast load modeling, it should be stated that this loading is calculated using a form of ConWep, which is based on the Kingery-Bulmash equations [40] that are well-known, but not openly available.

The current work builds upon previous research by developing a beam-column element with a bounding surface plasticity model specifically for blast applications. The air blast loading used to develop failure data for the bounding surface models is somewhat realistic, including spatial and temporal variation in load application. Also, a variety of different explosive locations are considered.

2.2.2 Paper organization

An overview of the beam-column element formulation is given in Section 2.3 of the current paper, while Section 2.4 discusses the bounding surface failure data acquisition. Section 2.5 presents bounding surface results for undamaged and blast-damaged versions of a member for three general explosive locations. Section 2.6 discusses the approach to modeling bounding surface data with real-valued spherical harmonics and presents fits to the bounding surface data for the three general test cases. The element implementation is discussed in Section 2.7, in order that conclusions may be drawn in Section 2.8.

2.3 Overview of element formulation

The blast beam-column element formulation is based on the traditional concentrated-plasticity frame element developed for nonlinear analysis of steel structures. For this element, the plasticity model relates member end forces (stress resultants) to member end deformations, which include axial strains and curvatures [25]. The 12 element end forces and their associated element degrees of freedom are shown in Fig. 2.1, as ordered pairings.

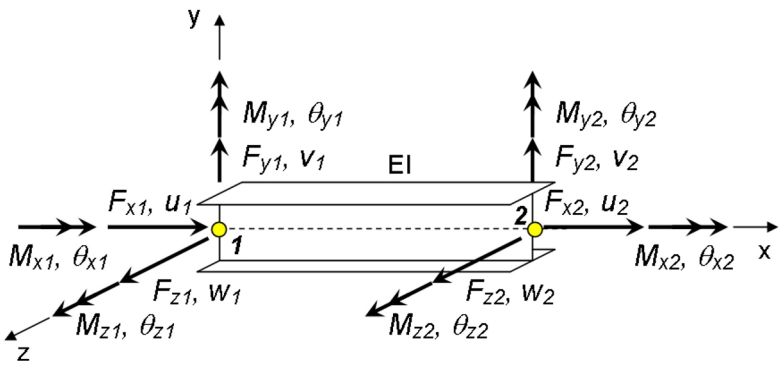

Figure 2.1: Beam-column element degrees of freedom and corresponding forces at each end. Force F_x coincides with the axial force, P.

2.3.1 Traditional element formulation

The following constitutes the foundation of the blast beam-column element formulation, where this basic formulation takes as a point of departure the traditional frame element for steel members [48, 49]. As is typical for a concentrated-plasticity element, plastic deformation is confined to zero-length plastic zones (hinges) at element ends. The material in the plastic hinges is assumed to be elastic-perfectly-plastic, with no strain hardening, and follows an associated flow rule for plastic deformation. Since this element is formulated for use in modeling structural elements with large span-to-depth ratios, shearing strain due to torsion and transverse shear are ignored when predicting the initiation of inelastic behavior at element ends, and so the boundary between elastic and inelastic behavior can be described by a three-dimensional bounding surface that specifies the initiation of inelastic response as a function of axial load and biaxial bending. The transition from elastic to plastic behavior is assumed to be abrupt and is represented by a sudden, complete plastification of the cross-

section at the yielded element end [48, 49].

Plastic behavior at element ends is dictated by a bounding surface plasticity model defined in stress-resultant space. A representative bounding surface for a steel wide-flange member is shown in Fig. 2.2.

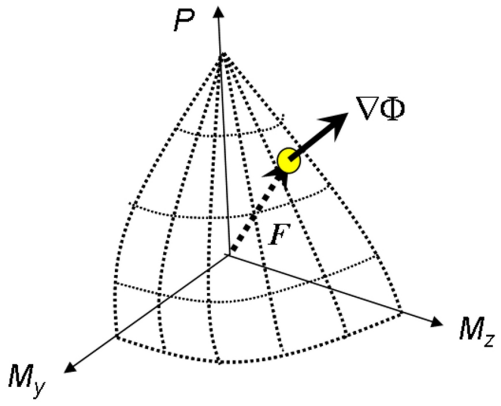

Figure 2.2: Hypothetical bounding surface plasticity model, shown in stress-resultant space.

Only the first octant of the surface is represented here because the bounding surface for an undamaged bisymmetrical cross-section is assumed to be symmetric about the coordinate axes in stress-resultant space [48]. The full element bounding surface is a function of three variables: the axial force, P; minor axis bending moment, M_y; and major axis bending moment, M_z, at an element end. Generally, these element forces are normalized by the element plastic section capacities P_Y, M_{py}, and M_{pz}, within the bounding surface definition. As an example, one form of the yield function for a traditional steel frame element is [48]

$$\Phi(p, m_y, m_z) = p^2 + {m_z}^2 + {m_y}^4 + 3.5p^2{m_z}^2 + 3p^6{m_y}^2 + 4.5{m_z}^4{m_y}^2 = 1, \qquad (2.1)$$

where p, m_y, and m_z represent the non-dimensional coordinates

$$p = P/P_Y, \tag{2.2}$$

$$m_y = M_y/M_{py}, \tag{2.3}$$

and

$$m_z = M_z/M_{pz}, \tag{2.4}$$

and P_Y, M_{py}, and M_{pz} are the squash load and minor and major axis plastic bending moments, respectively [48]. The gradient to the non-normalized bounding surface, denoted as $\nabla\Phi$ in Fig. 2.2, functions prominently in the element formulation

$$\nabla\Phi \equiv \left\{\partial\Phi/\partial P \;\; \partial\Phi/\partial M_y \;\; \partial\Phi/\partial M_z\right\}^T. \tag{2.5}$$

A main objective of the current research concerns the development of a suitable form for a yield function, analogous to Eq. (2.1), that is capable of describing the capacity that remains in an element after an explosion. The approach taken for modeling such a yield function forms a core part of the blast beam-column element formulation, and will be discussed later in this paper.

The bounding surface governs constitutive behavior at element ends. If the current force point is inside of the bounding surface, the element end is considered to be elastic, but if the current force point impinges on the bounding surface and persists there, then plastic behavior ensues. Force points outside of the bounding surface are inadmissible. In Fig. 2.2, the force vector **F** points to the current force point, located on the surface at $\left\{P \;\; M_y \;\; M_z\right\}$.

According to an associated flow rule, the plastic deformation at an element end is proportional to the gradient to the yield function (with respect to non-normalized element forces) at a given force point on the bounding surface. As

an example, if the internal forces at element end 1 represent a force point on the element end bounding surface, then the plastic deformation for element end 1 is a product of the magnitude of the plastic deformation, λ_1, and the direction of the deformation, $\mathbf{G_1}$, which is

$$\mathbf{G_1} = \left\{ \partial\Phi/\partial P_1 \;\; \partial\Phi/\partial M_{y1} \;\; \partial\Phi/\partial M_{z1} \right\}^T . \tag{2.6}$$

Thus, the vector of plastic increments in displacement at the element ends, $\mathbf{dU_p}$, is defined as

$$\mathbf{dU_p} = \begin{Bmatrix} dU_{p1} \\ dU_{p2} \end{Bmatrix} = \begin{bmatrix} \mathbf{G_1} & 0 \\ 0 & \mathbf{G_2} \end{bmatrix} \begin{Bmatrix} \lambda_1 \\ \lambda_2 \end{Bmatrix} = \mathbf{G}\,\lambda, \tag{2.7}$$

where $\mathbf{G_1}$ and $\mathbf{G_2}$ are the gradients to the bounding surface with respect to non-normalized element end forces P, M_y, and M_z at each element end, and λ_1 and λ_2 are the magnitudes of plastic deformation at the element ends [48, 49]. Vectors $\mathbf{G_1}$ and $\mathbf{G_2}$ are null if their respective element end force points do not persist on the bounding surface and so the matrix $\mathbf{G}$ only has nonzero elements at entries corresponding to an element end whose force point is impinging on the bounding surface [48, 49].

The relationship between the increment in the internal force vector, $\mathbf{dF}$, and the increment in displacement at both element ends, $\mathbf{dU}$, for the beam-column element is

$$\mathbf{dF} = \left(\mathbf{K_e} + \mathbf{K_g} + \mathbf{K_m}\right)\mathbf{dU} = (\mathbf{K_T} + \mathbf{K_m})\,\mathbf{dU} = \mathbf{K}\,\mathbf{dU}, \tag{2.8}$$

for material and geometrically nonlinear analyses, where $\mathbf{dU}$ can be decomposed into an elastic part, $\mathbf{dU_e}$, and a plastic part, $\mathbf{dU_p}$ to give $\mathbf{dU} = \mathbf{dU_e} + \mathbf{dU_p}$. Here, $\mathbf{K_e}$ is the linear elastic stiffness matrix, $\mathbf{K_g}$ is the initial stress matrix, $\mathbf{K_T} = \mathbf{K_e} + \mathbf{K_g}$ is the elastic tangent stiffness matrix, $\mathbf{K_m}$ is the element plastic reduction matrix, and $\mathbf{K}$ is the total system stiffness matrix [48, 49]. The initial stress matrix, which accounts for the nonlinear coupling of axial force and

flexure and the interaction between St. Venant's torsion and flexure within the element, and the linear elastic stiffness matrix are identical for the beam-column element and the classic frame element [48] and are not included here. The plastic reduction matrix, derived in [48, 49], is

$$\mathbf{K_m} = -\frac{\mathbf{K_T}\,\mathbf{G}}{\mathbf{G}^T\,\mathbf{K_T}\,\mathbf{G}}\,\mathbf{G}^T\,\mathbf{K_T}. \tag{2.9}$$

The gradient to the element bounding surface, $\nabla\Phi$, appears in Eq. (2.9) via $\mathbf{G}$, which is defined within Eq. (2.7) and relies on Eq. (2.6) and Eq. (2.5). The plastic reduction matrix in Eq. (2.9) differs slightly from the traditional form appearing in the literature [48, 49] as the elastic tangent stiffness matrix is substituted for the linear elastic stiffness matrix here. The definition for $\mathbf{K_m}$ is included here since the bounding surfaces used for each formulation differ as well.

2.3.2 Deviation from traditional element formulation

The main differences between the blast beam-column element and the traditional frame element lie with the yield function and the modes of failure captured within the element formulation. The bounding surface for the blast beam-column element is based on numerical failure data acquired from detailed shell element-based models of individual wide-flange members subjected to a simulated explosion and subsequently loaded to collapse. Failure of the high-resolution models is based either on buckling or an excessive strain level anywhere within the member, as discussed in greater detail later in this paper. Since the yield function of the blast beam-column element is based on failure of an entire wide-flange member, if the force point at either member end impinges on the associated bounding surface, then the *member* is assumed failed, and both

ends assigned nonzero entries in **G**. This is in contrast to the behavior of individual member ends specified in more traditional formulations.

2.4 Bounding surface failure data acquisition

Development of a yield function to define a bounding surface for the blast beam-column element is based on failure data obtained numerically for a steel wide-flange member with simulated blast-induced damage. Numerical experiments are carried out using the commercial finite element package, LS-DYNA, which is a transient dynamic nonlinear finite element code with an availability of numerous nonlinear material models [45].

Component failure data is acquired through a series of virtual load tests. For these, a member that has already been damaged by blast loading, within a dynamic nonlinear finite element analysis, is statically loaded to failure in separate collapse analyses, each with a unique combination of proportional moment-thrust loading. The moments and axial load at failure provide a single force point representing failure. Given a specific blast location and explosive yield, the locus of all such similar points defines the bounding surface for this member, for a particular blast. Repetition of this procedure for other explosions results in a library of potential bounding surfaces in a beam-column element model. The procedure is outlined as follows:

1. Select parameters defining the current bounding surface (*i.e.* geometry, material, etc. for the member and blast)
2. Perform a nonlinear dynamic analysis to simulate the structural response

to the blast and resulting damage sustained by the member

3. Loop over a series of axial load and biaxial moment combinations

   - For each moment-thrust combination, perform a collapse analysis to determine the force point at failure (defined by either load-shedding or excessive straining)

4. Compile failure force point data to give a point cloud (in stress-resultant space) that represents the bounding surface for that member, for the chosen explosive scenario

2.4.1 Material model

Given the severity of explosive air burst, it is essential to incorporate nonlinearity into the high-resolution blast simulations, in the form of nonlinear kinematics and rate-dependent constitutive behavior. Material rate-dependency and strain-hardening are included in the well-known Johnson-Cook relation [34, 35],

$$\sigma_{flow} = \left[A + B\left(\varepsilon_{ep}\right)^{n}\right]\left[1 + C\, ln\, \dot{\varepsilon}^{*}_{ep}\right]\left[1 - (T^{*})^{m}\right], \tag{2.10}$$

where σ_{flow} is the flow stress, ε_{ep} is the effective plastic strain, T^{*} is the homologous temperature, and A, B, n, C, and m are material constants. In Eq. (2.10) the expression $\dot{\varepsilon}^{*}_{ep} = \dot{\varepsilon}_{ep}/\dot{\varepsilon}_{0}$ denotes the dimensionless plastic strain rate, which has been normalized by $\dot{\varepsilon}_{0}$, the quasistatic strain rate used in the experimental determination of the strain hardening parameters, B and n.

Based on results from previous research [28], a simplified form of the Johnson-Cook relationship from Eq. (2.10) is used for the current research. For

this model, the flow stress is defined as the product of a strain hardening term, $\left[A + B\left(\varepsilon_{ep}\right)^n\right]$, and a viscoplastic term, $\left[1 + C\, ln\, \dot{\varepsilon}^*_{ep}\right]$, or

$$\sigma_{flow} = \left[A + B\left(\varepsilon_{ep}\right)^n\right]\left[1 + C\, ln\, \dot{\varepsilon}^*_{ep}\right]. \tag{2.11}$$

Johnson-Cook model parameters for ASTM-A36 steel are used to model the constitutive behavior of the hot-rolled steel wide-flange members. Material constants used for this steel are E = 199.4 GPa, ν = 0.3, and ρ = 7850 kg/m^3. The Johnson-Cook parameters are A = 244.764 MPa, B = 483.929 MPa, $C = 1.6503 \times 10^{-2}$, n = 0.23505, $\dot{\varepsilon}_0 = 1.9457 \times 10^{-4}$ s^{-1} [57, 55, 56].

2.4.2 Wide-flange member model

The post-blast capacity of a structural member depends on numerous parameters not limited to member length, cross-sectional proportions, material, boundary conditions, and blast size and location with respect to the member; therefore, it is clear that the bounding surface for a blast beam-column element is strongly dependent on a given set of these parameters. However, with the high performance computing resources currently available, it is possible to carry out the numerous numerical experiments needed to provide bounding surface data for a wide variety of members and blast locations (*i.e.* to populate a library of such surfaces, for various parameter combinations), as detailed in the companion paper [29].

The current research is focused on the development of bounding surface models for a reasonable subset of explosion locations for a single member, to be used as a proof of concept for the blast beam-column element formulation. For the purposes of the present discussion, we will restrict our attention

to a W360x57.8 (W14x38) member, 3.05 m (10 ft) long, with simply supported boundary conditions. Fig. 2.3 illustrates a schematic of the high-resolution model for a representative blast scenario, one in which the explosion is centered on the member web and its force induces bending in the weak-axis direction.

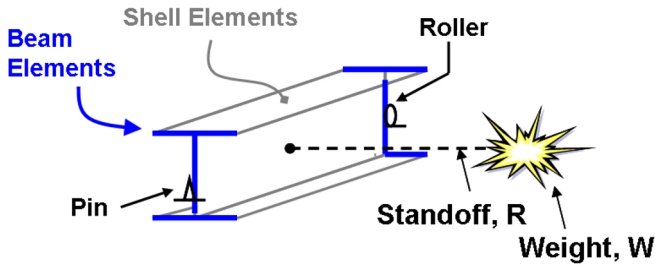

Figure 2.3: Wide-flange member model setup.

The model is comprised of a mix of shell and beam elements. The web and flanges are modeled with Belytschko-Lin-Tsay shell elements [31] with element thickness equal to the appropriate plate thicknesses. Very stiff Belytschko-Schwer [31] beam elements are placed along the web and flanges at the member ends, in order to suppress cross-sectional distortion at the support locations. The beam elements are circular in cross-section with a diameter of 25.4 mm, and are perfectly elastic, with $\nu = 0.3$ and $E = 20,300$ GPa, which is 100 times the stiffness of the shell element material. A mesh seed of 14.3 mm, or 6 elements per flange outstand, applied globally to the model, provides sufficient resolution to capture local deformation effects induced by an explosion, as determined by a mesh convergence study.

2.4.3 Blast Loading

Air blast loading is applied over structural surfaces in direct line of sight of the explosion using a blast load generation code previously developed by the authors [28]. Acting as a preprocessor to LS-DYNA, the air blast load generation code calculates spatially and temporally varying blast loads for a given explosive scenario, where these loads are then applied as nodal force time histories within the finite element model.

While LS-DYNA has a built-in capability to calculate and apply air blast loading, the air blast load generation code developed by the authors is used for this research because it is based on data and equations derived from open-literature sources, and it includes a shadowing algorithm that applies reduced blast loading to partially shielded surfaces. In contrast, the air blast loading module in LS-DYNA is based on ConWep [33], a well-known air blast load generation program only available to the U.S. military and government contractors, and it cannot account for partial shielding since it is only able to apply fully reflected blast loading to selected model nodes.

Blast overpressure

For each node in direct line of sight to an explosion, the air blast generation code calculates the standoff distance R between the node and the blast source, then uses parameter equations to calculate the air blast parameters for a reference explosion at the same scaled distance, $Z = R/W^{1/3}$, where W is the weight of the explosive (equivalent TNT) [28]. Employing Hopkinson scaling, which assumes that pressures, temperatures, densities, and velocities at equivalent scaled dis-

tances are the same at homologous times, the air blast parameter values for the reference explosion are converted to blast parameter values corresponding to the current explosive scenario.

Specifically, the parameter equations used are drawn from data and equations openly available in [41, 18], and the resulting overpressure time histories are of a decaying exponential form called the modified Friedlander's equation,

$$P(t) = \begin{cases} 0, & t < t_a, \\ P_{max}\left(1 - \frac{t-t_a}{t_d}\right) e^{-b\left(\frac{t-t_a}{t_d}\right)}, & t_a \leq t \leq t_a + t_d, \\ 0, & t > t_a + t_d. \end{cases} \tag{2.12}$$

Here, $P(t)$ is the overpressure at time t after detonation, P_{max} is the peak overpressure, t_a is the arrival time of the shock wave, t_d is the duration of the shock wave, and b is the decay constant. Depending on whether or not the point of interest is located on the surface of an object, P_{max} is either equal to P_s, the peak side-on overpressure (in free air) or $P(t, \Theta)$, the (reflected) overpressure developed upon shock wave reflection at a rigid surface for a given angle of incidence, Θ [28]. The associated air blast parameters, P_{max}, t_a, t_d, and b are calculated as a function of scaled distance, angle of incidence, and charge type (spherical or hemispherical). Since the load calculation for hemispherical explosions involves much more uncertainty than spherical explosions, only spherical explosions are examined herein. Within the air blast load generation code, the overpressure time histories are calculated based on Eq. (2.12), and are converted to nodal force time histories using element tributary area.

Protective design of structures for air blast involves design for a target threat, or charge weight W. Vehicle bombs employing sedans to vans can contain 227 to 1814 kg (500 to 4000 lb) of TNT equivalent explosive material [26]. A bomb size

of W = 453.6 kg (1000 lb) equivalent TNT is in the middle of the range of potential terrorist threats associated with automotive bombs [26]. Consequently, the current research focuses on a W = 453.6 kg (1000 lb) equivalent TNT explosion, in order to produce results that correspond to an intermediate-level explosive threat.

Load Application

As previously stated, the force time histories calculated by the air blast load generation code are applied over structural surfaces in direct line of sight to an explosion. However, with respect to wide-flange members, there are cases where the blast epicenter is not centered on the web or the flanges, a situation that causes regions of the member to be partially shielded from the full force of the shock wave. To address this problem, the air blast load generation code uses a shielding algorithm for application of loads in partially shielded areas [28].

The shielding algorithm uses a ray tracing technique to determine which surfaces of a structure are in direct line of sight to an explosion and which surfaces are partially shielded by another part of the structure. In partially shielded areas, the air blast load generation code models the magnification of the surrounding overpressure with an applied blast loading that corresponds to the side-on, or free air, explosive shock load. In regions in direct line of sight to the blast, fully reflected blast loading is applied. As further explanation, the side-on overpressure is the blast loading observed as an explosive shock wave travels past a stationary point in free air, whereas reflected overpressure is the much larger loading observed at a point on a rigid surface as a shock wave strikes and reflects off of the surface.

Fig. 2.4 shows an example of the load application for a partially shielded member. Reflected air blast loading is only applied to regions of the member that are not shielded from the initial explosive shock wave: the bottom surface of the bottom flanges, the bottom surface of the top flanges nearest the blast, and the upper portion of the web on the side facing the blast. The lower part of the member web facing the explosion is partially shielded from the blast, and in this region, side-on overpressure loading is applied.

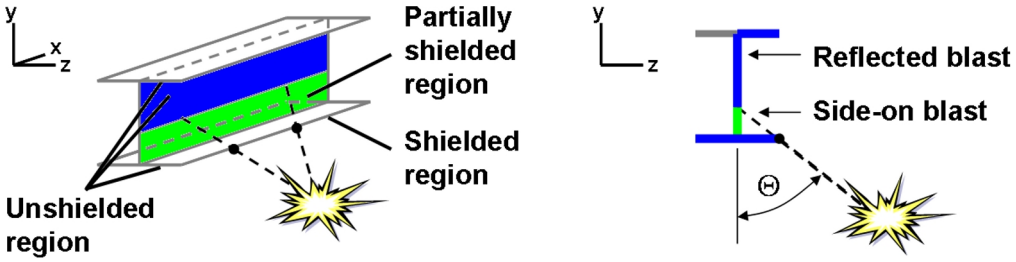

Figure 2.4: Schematic of shielding effects included in air blast load generation program.

2.4.4 Analysis sequence

As stated previously, failure data acquisition involves a multi-step analysis procedure. First, a nonlinear dynamic explicit analysis is performed to determine the damaged model configuration of a member exposed to a certain explosive threat. In a separate static analysis, the blast-damaged member is then loaded with proportional moment-thrust loading until failure, in order to obtain a data sample of the radial distance to the bounding surface along that applied loading vector.

Dynamic analyses are carried out to a total solution time of 1300 ms, where mass damping (5%) is applied after 750 ms in order to generate the final deformed shape of the wide-flange member by the end of the analysis. The damping force is assumed to be proportional to the velocity, with a proportionality constant equal to the damping ratio, ζ, multiplied by twice the fundamental frequency of the structure, where $\zeta = 0.05$.

When using automatic time-stepping, LS-DYNA sets the time step to the minimum of the critical time step size computed for the beam and shell elements. Thus, to ensure a uniform critical time step size for the entire model, the density of the cross-section-stiffening beam elements is modified so that the critical time step size is similar for both the shell and beam elements. Consequently, the material density of the beam elements is set as $\rho = 655\rho_{shell} = 5142 \times 10^3$ kg/m^3, where ρ_{shell} is the density of the shell elements.

2.4.5 Failure criteria

When simulating the post-blast static response of a member, combinations of moment-thrust loading are applied to a member and increased proportionally to failure. While combined loading with a strong component of axial compression often results in global collapse due to column instability, failure for load combinations with tensile or small compressive axial loads is more complicated. In design codes, the failure of tensile members is often assumed to occur upon full plastification of the cross-section [3]. Consequently, for the members considered in this research, the second criterion for structural failure is the exceedance of a specified maximum strain anywhere in the member domain. The failure

strain ϵ_{fail} is defined to be the strain level at which strain-hardening commences in ASTM-A36 steel, equal to an engineering strain of $\epsilon_{st} = 0.0203$ [5]. Employing the usual conversion to true strain, the strain-to-failure criterion is represented by a true effective plastic strain of $\epsilon_{ep} = 0.01887$.

While seemingly arbitrary, limiting normal cross-section strains to be smaller than ϵ_{st} makes sense from the standpoint that $\epsilon_{st} \approx 5\,\epsilon_Y$ for ASTM-A36 steel; such a deformation level would likely result in structural integrity issues within a given structural system. Additionally, when considering plastic hinging, the attainment of flexural normal stresses equal to ϵ_{st} roughly corresponds to commonly applied non-seismic structural ductility requirements [3].

2.4.6 Static analyses to determine failure loads

In the second step of the analysis sequence for a given blast-damaged member, the damaged member is loaded to failure in a static collapse analysis. The deformed geometry and residual strain field from the end of the dynamic blast simulation are used to initialize each static analysis. Collapse analyses are carried out in LS-DYNA using a nonlinear quasi-Newton solver and automatic load step control.

For an individual collapse analysis, combined loading representing a vector in stress-resultant space is applied proportionally as $LPF \cdot \left\{P \; M_y \; M_z\right\}$, where the load proportionality factor, LPF, is increased until either of the two previously defined failure criteria is met. Loading vectors are defined such that the Euclidean norm of the loading vector when normalized by the plastic section capacities is equal to LPF, or $\sqrt{\left(\frac{P}{P_Y}\right)^2 + \left(\frac{M_y}{M_{py}}\right)^2 + \left(\frac{M_z}{M_{pz}}\right)^2} = 1$. Thus, the value of the

load proportionality factor (LPF) at failure, equal to max(LPF), actually represents the radial distance $\hat{r}(\theta, \phi)$ from the origin along the current loading vector to the bounding surface in normalized stress-resultant space for the member and blast scenario of interest, or

$$\hat{r}(\theta, \phi) = \max(LPF), \tag{2.13}$$

where θ is the colatitude, $\theta \in [0\ \pi]$, and ϕ is the longitude, $\phi \in [0\ 2\pi)$, as is typical for spherical coordinates. The colatitude and longitude can be calculated using the following Cartesian-to-spherical coordinate conversions:

$$\theta = \theta(p, m_y, m_z) = \arccos\left\{\frac{p}{\sqrt{{m_y}^2 + {m_z}^2 + p^2}}\right\}, \tag{2.14}$$

and

$$\phi = \phi(p, m_y, m_z) = \text{atan2}(m_z, m_y), \tag{2.15}$$

where p, m_y, and m_z are the non-dimensional coordinates defined in Eq. (2.2), (2.3), and (2.4). A schematic of the static loading and the failure data acquisition process is shown in Fig. 2.5. The moments are applied as force couples over the cross-section midline height, h, and bottom flange width, b_f.

In order to obtain data representing the blast-damaged bounding surface for a given member and explosive scenario, multiple separate collapse analyses are performed for loading vectors at various θ and ϕ over a spherical grid in stress-resultant space. The sampling grid consists of a series of equally spaced latitude and longitude lines of unit radius. Results of a sensitivity study suggest that a sampling grid with 13 latitude and longitude lines per octant is sufficient to capture the blast bounding surface topology in a computationally efficient manner. This grid mesh density is formed using an angular increment in colatitude and longitude equal to 7.5 deg ($\Delta\theta = \Delta\phi = 7.5$ deg), for a total of 1106 sampling points.

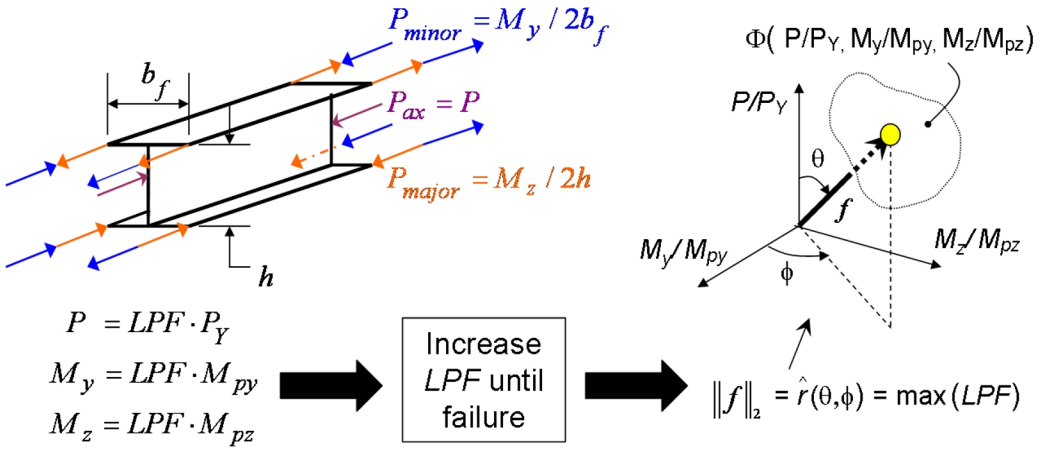

Figure 2.5: Application of static forces P, M_y, and M_z, and corresponding data sample of bounding surface in normalized stress-resultant space. Moments M_y and M_z are applied as force couples P_{minor} and P_{major}, respectively.

As this process is extremely computationally intensive, requiring 1106 separate collapse analyses to compile data samples of the bounding surface for a single structural member and explosive scenario, the process has been automated with a set of ancillary programs and scripts. The automated failure data acquisition is performed in parallel on a SGI Altix XE 1300 High Performance Computing Cluster, where each of the 42 nodes has 8 GB of RAM and two quad-core Xeon Processors (2.66 GHz). The data acquisition for each of the bounding surfaces for the case studies presented herein requires roughly 15 hours of computational time across 48 processor cores.

2.5 Bounding surface failure data results

While the source of an air blast could be located at an infinite number of points with respect to the local coordinate axes of a structural member, this parameter space is narrowed to a handful of practically relevant locations for the re-

search presented in this paper. Of particular interest are blast locations that induce structural motion dominated by a single fundamental mode shape, such as bending about the strong- or weak-axis. For these explosive loading scenarios, the pure nature of the response may be useful in justifying changes observed in the member bounding surface as a result of the blast. However, most blast locations will result in a mixed-mode response, and so blast locations producing this type of response are also considered.

In order to simplify the following discussion regarding failure data results for different explosive scenarios, blast locations are cataloged as a function of the following three parameters, illustrated in Fig. 2.6:

- $R_{\perp}$: the perpendicular distance from the blast source point to the element longitudinal axis
- X: the distance along the element longitudinal axis to the intersection with the vector denoting the perpendicular distance from the blast source point to the element longitudinal axis
- $\Theta_{\perp}$: the angle between the normal to the member longitudinal axis that is coplanar with the member web, and the vector from the blast source point to the element longitudinal axis along the shortest path (of length $R_{\perp}$)

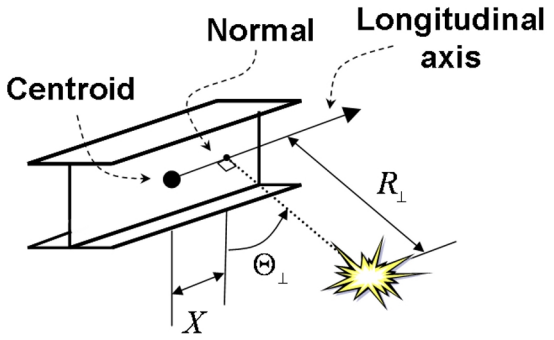

Figure 2.6: Blast location defined as a function of $R_\perp$, $\Theta_\perp$, and X, where $\Theta_\perp$ = 45 deg and $X = L/4$ is shown here.

2.5.1 Case studies

In order to examine a variety of response modes, three separate cases of perpendicular loading angle ($\Theta_\perp$) are considered for the member using the following naming conventions:

1. Strong-axis blast ($\Theta_\perp$ = 0 deg)
2. Half blast ($\Theta_\perp$ = 45 deg)
3. Weak–axis blast ($\Theta_\perp$ = 90 deg)

For explosions located at midspan of the member (X = 0), the prevailing structural response is strong-axis flexure for $\Theta_\perp$ = 0 deg, and weak-axis flexure for $\Theta_\perp$ = 90 deg. Values of $\Theta_\perp$ between 0 and 90 deg will produce a response that combines various dominant structural modes. Results from these three cases for midspan explosions (X = 0) are the focus of this paper and are presented subsequently. As previously mentioned, the target threat is a W = 453.6 kg (1000 lb) TNT equivalent spherical air blast.

For each of the general cases, $R_\perp$ is iterated on in 0.15 m (0.5 ft) increments until a value is reached such that the maximum effective plastic strain over the model domain is slightly less than the failure strain, or until $\max(\epsilon_{ep}) \approx 0.01887$. This represents a standoff distance that comes very close to causing failure of the member through the action of the (dynamic) explosion alone. The resulting minimum perpendicular standoff distances for midspan blast are: $R_\perp = 6.10$ m (strong-axis blast), $R_\perp = 8.23$ m (half blast), and $R_\perp = 14.63$ m (weak-axis blast).

2.5.2 Results for undamaged and blast-damaged members

In order to ascertain the effects of an explosion on member capacity, the bounding surface data for the blast-damaged member are compared to the bounding surface data for an undamaged member, where both sets of data are obtained as detailed previously, and each data sample is calculated according to Eq. (2.13). Fig. 2.7, 2.8, and 2.9 depict the blast-damaged failure data superimposed with the undamaged failure data in normalized stress-resultant space for the three general test cases. These visualizations are achieved by connecting adjacent failure points in the spherical grid with polygon facets. The facets are rectangular for the main body of the sampling grid, but are triangular for points immediately adjacent to the pure axial loading states.

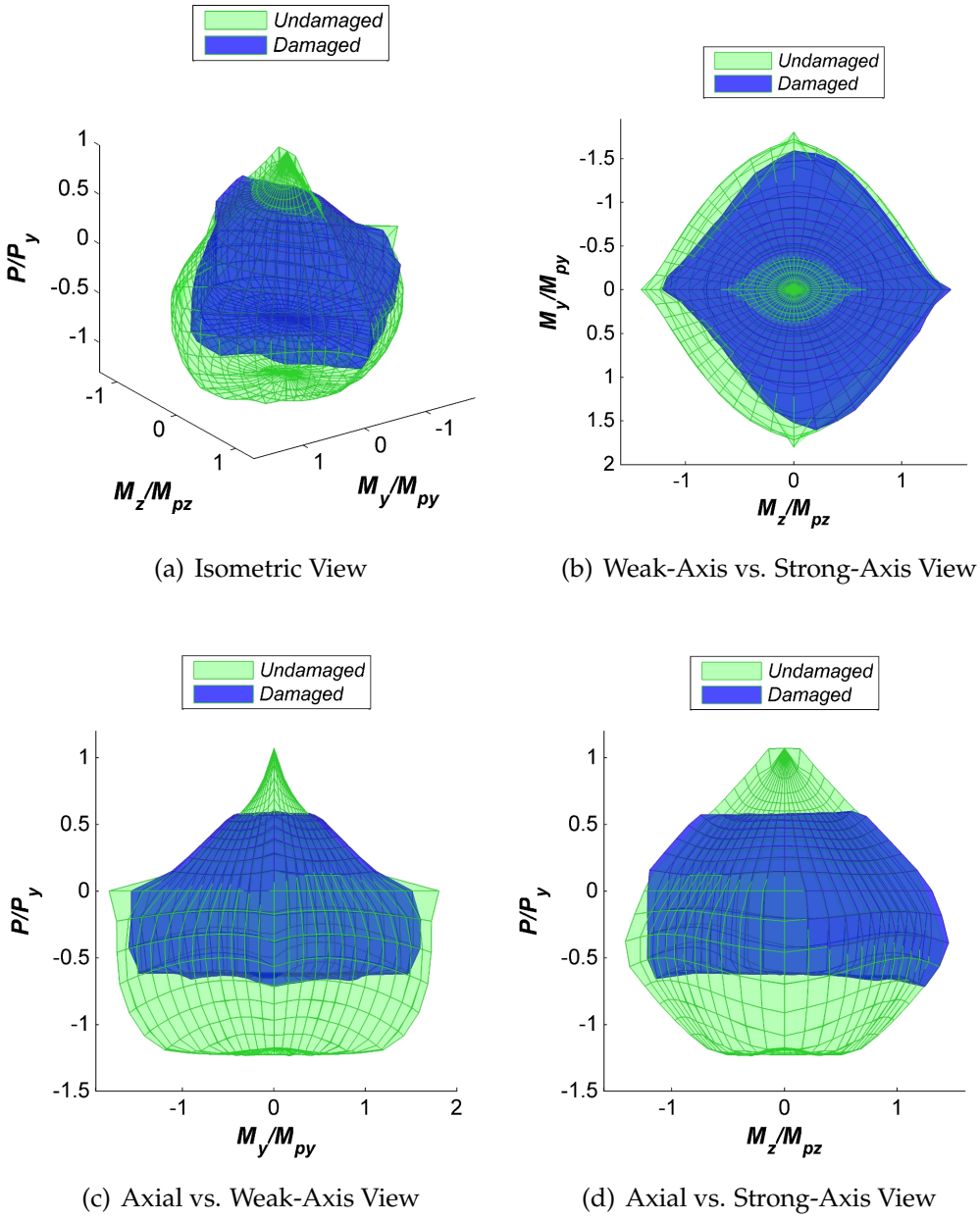

(a) Isometric View

(b) Weak-Axis vs. Strong-Axis View

(c) Axial vs. Weak-Axis View

(d) Axial vs. Strong-Axis View

Figure 2.7: Comparison of bounding surfaces for an undamaged W360x57.8 (W14x38) member, L = 3.05 m long, and one that has been subjected to an explosion at $R_{\perp}$ = 6.10 m, $\Theta_{\perp}$ = 0 deg, and X = 0 m (strong-axis blast at midspan).

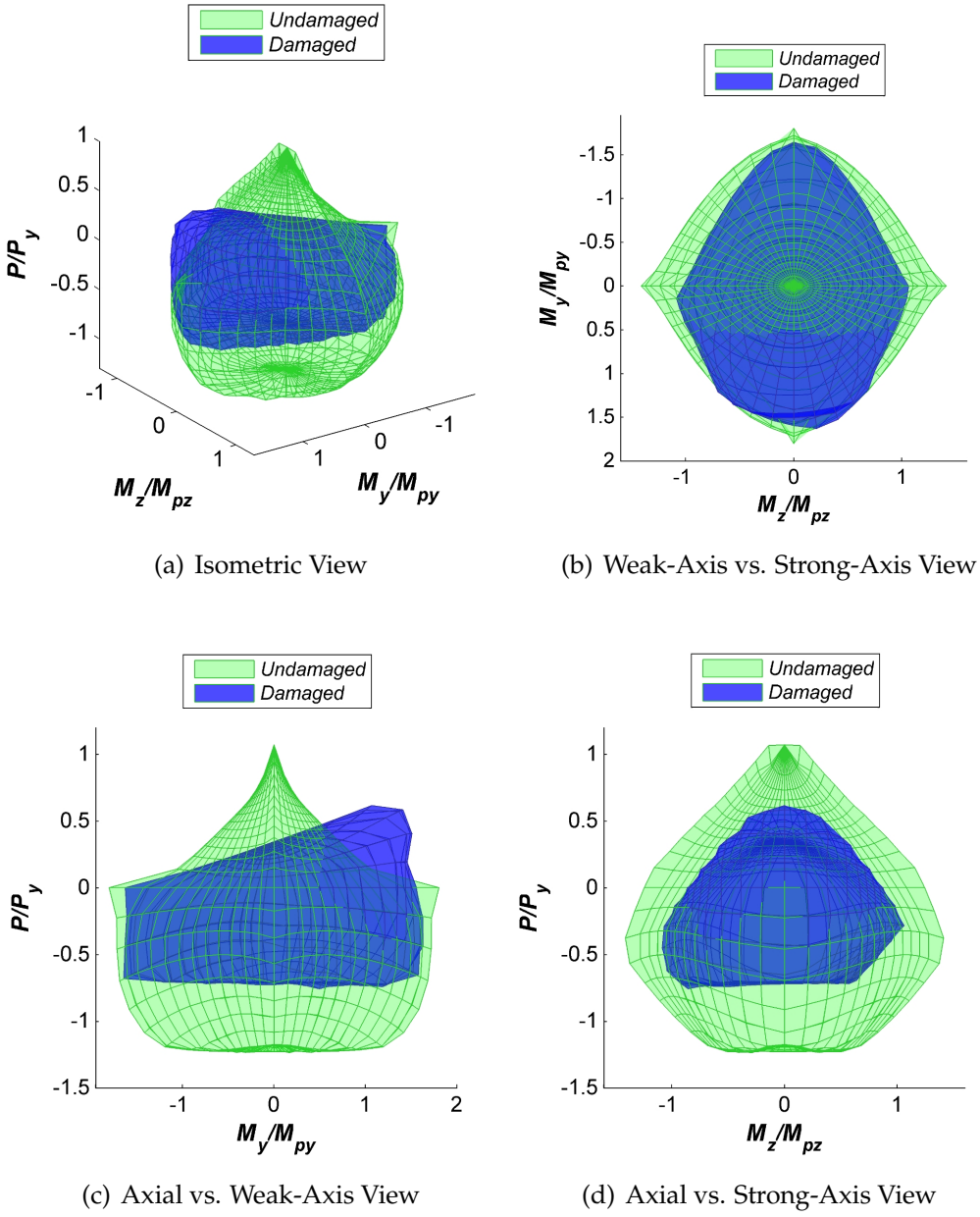

(a) Isometric View

(b) Weak-Axis vs. Strong-Axis View

(c) Axial vs. Weak-Axis View

(d) Axial vs. Strong-Axis View

Figure 2.8: Comparison of bounding surfaces for an undamaged W360x57.8 (W14x38) member, L = 3.05 m long, member and one that has been subjected to an explosion at $R_{\perp}$ = 8.23 m, $\Theta_{\perp}$ = 45 deg, and X = 0 m (half blast at midspan).

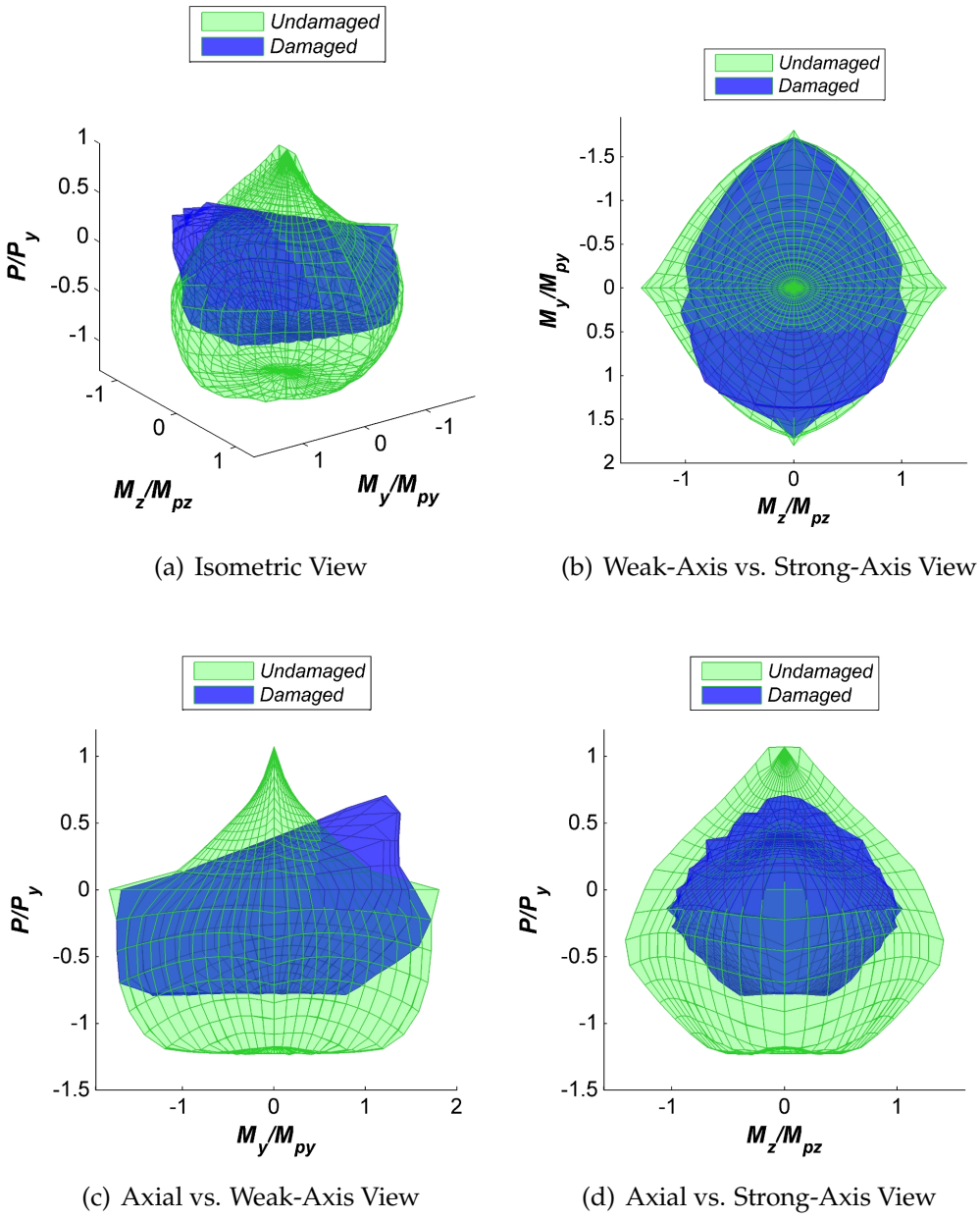

(a) Isometric View

(b) Weak-Axis vs. Strong-Axis View

(c) Axial vs. Weak-Axis View

(d) Axial vs. Strong-Axis View

Figure 2.9: Comparison of bounding surfaces for an undamaged W360x57.8 (W14x38) member, $L = 3.05$ m long, member and one that has been subjected to an explosion at $R_{\perp} = 14.63$ m, $\Theta_{\perp} = 90$ deg, and $X = 0$ m (weak-axis blast at midspan).

Fig. 2.7, 2.8, and 2.9 provide a qualitative picture of the change in member capacity resulting from explosions in various locations with respect to member geometry. In all cases, the blast produces a significant reduction in member strength for many combinations of member forces; however, some locations exist where the damaged bounding surface breaches the superimposed undamaged bounding surface, indicating strengthening of the member for certain subsets of force combinations. This strengthening effect is especially apparent in the half and weak-axis cases, where it occurs in the compressive half of stress-resultant space for the sense of weak-axis flexure opposite to that induced by the explosion. This phenomenon can most easily be observed in Fig. 2.8(c) and Fig. 2.9(c). The strengthening effect physically emanates from a requirement to bend opposite to the direction of blast damage (*i.e.* straightening the member, then continuing with flexure in the same sense).

Additionally, all damaged and undamaged bounding surfaces exhibit flattened bottom regions, which is an artifact of the strain-to-failure criterion that is generally the mode of failure for load combinations with tensile axial components. This flattening of the bounding surface is also seen at the top of the damaged surface for the strong-axis blast case, shown in Fig. 2.7(d); here, the member has sustained enough plastic deformation from the blast that under compressive loading it fails due to excessive strain levels rather than buckling.

Regarding the strong-axis case, there also exists a distortion of the bounding surface that is characterized by a reduced member capacity for forces with large components of strong-axis bending in the same direction as induced by the blast, although the capacity for strong-axis bending forces in the opposite direction is virtually unchanged. This is most easily observed in Fig. 2.7(b). This

distortion is not readily apparent in the half blast case pictured in Fig. 2.8(b).

The effect of the blast on member capacity is quantitatively evaluated using the following global damage index, based on a normalized ℓ_2 norm,

$$DI = \frac{\| \hat{r}(\theta,\phi)_{dmg} - \hat{r}(\theta,\phi)_{und} \|_2}{N} = \frac{\sqrt{\sum_{i=1}^{N} \left[\hat{r}(\theta_i,\phi_i)_{dmg} - \hat{r}(\theta_i,\phi_i)_{und} \right]^2}}{N}. \tag{2.16}$$

Here, N is the number of sampling points, and $\hat{r}(\theta,\phi)_{dmg}$ and $\hat{r}(\theta,\phi)_{und}$ are the radial failure data obtained from Eq. (2.13) for the blast-damaged and undamaged members, respectively. The results calculated using this metric for the three general test cases are displayed in Table 2.1.

Table 2.1: Damage index values for a W360x57.8 (W14x38) member, L = 3.05 m long, for blast at midspan.

Case	$R_\perp$ (m)	$\Theta_\perp$ (deg)	X (m)	DI
Strong-axis	6.10	0	0	1.08×10^{-2}
Half	8.23	45	0	1.19×10^{-2}
Weak-axis	14.63	90	0	1.18×10^{-2}

The quantitative results indicate that the wide-flange member experiences a similar level of global blast-induced damage for each of the three general cases, with slightly more damage imparted to the member in the strong-axis case. However, it is important to point out that the level of damage is greatly affected by the explosion standoff distance. For example, in the above results the blast epicenter for the weak-axis case is more than twice as far away from the member centroid as it is for the strong-axis case, yet these two cases produce quantitatively similar magnitudes of change between the undamaged and blast-damaged bounding surfaces. This result highlights the importance of nonlinear blast energy attenuation with distance, since the ratio in strong- to weak-axis plastic section modulus for this section is approximately a factor of five.

2.6 Bounding surface modeling

The blast beam-column element formulation uses the gradient to the bounding surface at a given force point (in stress-resultant space) for the computation of the plastic deformation by way of a plastic reduction matrix that encapsulates all nonlinear material effects. As seen from Fig. 2.7, 2.8, and 2.9, faceted bounding surface data for blast-damaged wide-flange members are not everywhere smooth. Thus, it is necessary to find a functional form that gives a smooth approximation to the failure data in order to prevent numerical difficulties that may arise in attempting to compute a gradient at a corner.

2.6.1 Spherical harmonic functions

Given the method of failure data acquisition, a natural choice for a functional form to represent the bounding surface failure data is one that is based on a linear combination of spherical basis functions. Such basis functions may be obtained as spherical harmonics, which possess the following characteristics: they are the angular portion of the solution to Laplace's equation in spherical coordinates; they are defined on the unit sphere; and they form a complete set of orthonormal functions [24, 19]. These functions are commonly used for surface rendering in computer graphics, computational biology and chemistry, and medical imaging applications [17, 19, 12, 24, 58]. Spherical harmonic (SPHARM) functions are defined as [17, 12]

$$\begin{aligned} Y_l{}^m(\theta,\phi) &= \sqrt{\frac{(2l+1)}{4\pi}}\sqrt{\frac{(l-m)!}{(l+m)!}}\, P_l{}^m cos(\theta)\, e^{\,im\phi} \\ &= N(l,m)\, P_l{}^m cos(\theta)\, e^{\,im\phi}, \end{aligned}$$

where $N(l,m)$ is a normalization function and ${P_l}^m cos(\theta)$ are the Legendre associated polynomials that are defined with respect to Cartesian coordinates as [17, 12]

$$ {P_l}^m(x) = \frac{(-1)^m}{2^l\, l!}(1-x^2)^{\frac{m}{2}} \frac{\partial^{\,l+m}}{\partial x^{\,l+m}}(x^2-1)^l, \tag{2.17} $$

and can be converted to ${P_l}^m cos(\theta)$ by substituting $x = \cos\theta$ in the above [42, 17]. For a given spherical harmonic, ${Y_l}^m(\theta,\phi)$, the integer l denotes the harmonic degree and the integer m is the order, which is constrained to $-l < m < l$ [24]. Spherical harmonics exhibit the following property

$$ {Y_l}^{-m}(\theta,\phi) = (-1)^m\ {Y_l}^{m\,*}(\theta,\phi), \tag{2.18} $$

where ${Y_l}^{m\,*}(\theta,\phi)$ is the complex conjugate of ${Y_l}^m(\theta,\phi)$ [17, 12].

The real-valued subset of spherical harmonics, called tesseral harmonics, are often used for fitting graphical data, and are defined as [12]

$$ {y_l}^m(\theta,\phi) = \begin{cases} \sqrt{2}\ N(l,m)\ {P_l}^m cos(\theta)\ cos\, m\phi, & m > 0, \\ {Y_l}^0(\theta,\phi), & m = 0, \\ \sqrt{2}\ N(l,m)\ {P_l}^m cos(\theta)\ sin\, |m|\phi, & m < 0, \end{cases} \tag{2.19} $$

where the normalization function $N(l,m)$ is the same as in Eq. (2.17). The current research is concerned with real, rather than complex, surface quantities, and so the real-valued subset of spherical harmonics, ${y_l}^m(\theta,\phi)$, are the basis functions used to provide functional approximations to the blast bounding surface data examined herein.

2.6.2 Bounding surface modeling with real-valued spherical harmonic functions

The yield function chosen to model the blast-damaged beam-column element bounding surface defines the radial distance from the origin to a point on the bounding surface in normalized stress-resultant space. The radial yield function takes the form of

$$r(\theta, \phi) = \sum_{l=0}^{\infty} \sum_{m=-l}^{l} c_l{}^m \, y_l{}^m(\theta, \phi), \tag{2.20}$$

where θ and ϕ are the colatitude and longitude in stress-resultant space, respectively, as defined in Eq. (2.14) and (2.15). Sensitivity studies conducted as part of this research show that an acceptable degree of accuracy can be obtained by approximating the bounding surface function using basis functions up to the 4^{th} order, achieved by truncating the series at $L = l_{max} = 4$. Thus, the radial yield function is given by the following truncated series with 25 terms

$$r(\theta, \phi) \approx \sum_{l=0}^{L} \sum_{m=-l}^{l} c_l{}^m \, y_l{}^m(\theta, \phi). \tag{2.21}$$

Applying a least-squares regression to the available bounding surface data provides an estimate for the harmonic coefficients $c_l{}^m$ in Eq. (2.21). By defining $\hat{\mathbf{r}}$ as a column vector of sampled radial failure data points that each correspond to a given (θ_i, ϕ_i) pair, $\mathbf{Y}$ as a matrix of the real-valued spherical harmonics where each row is evaluated for (θ_i, ϕ_i), and $\hat{\mathbf{c}}$ as a column vector of the corresponding harmonic coefficients, then Eq. (2.21) can be written as the following linear system of equations [24],

$$\hat{\mathbf{r}} = \mathbf{Y} \, \hat{\mathbf{c}}. \tag{2.22}$$

In Eq. (2.22), $\hat{\mathbf{r}}$ is a column vector of radial failure data points sampled according to Eq. (2.13) at different values of θ and ϕ for $N = 1106$ samples,

$$\hat{\mathbf{r}} = \begin{pmatrix} \hat{r}(\,\theta_1, \phi_1\,) \\ \hat{r}(\,\theta_2, \phi_2\,) \\ \vdots \\ \hat{r}(\,\theta_N, \phi_N\,) \end{pmatrix}, \tag{2.23}$$

$\hat{\mathbf{c}}$ is a vector of the estimated harmonic coefficients up to degree L, or

$$\hat{\mathbf{c}} = \begin{pmatrix} \hat{c}_0{}^0 \\ \hat{c}_1{}^{-1} \\ \hat{c}_1{}^0 \\ \hat{c}_1{}^1 \\ \vdots \\ \hat{c}_L{}^L \end{pmatrix}, \tag{2.24}$$

and $\mathbf{Y}$ is a matrix of the real-valued spherical harmonics where each row corresponds to a known bounding surface data point,

$$\mathbf{Y} = \begin{pmatrix} y_0{}^0(\theta_1, \phi_1) & y_1{}^{-1}(\theta_1, \phi_1) & y_1{}^0(\theta_1, \phi_1) & y_1{}^1(\theta_1, \phi_1) & \dots & y_L{}^L(\theta_1, \phi_1) \\ y_0{}^0(\theta_2, \phi_2) & y_1{}^{-1}(\theta_2, \phi_2) & y_1{}^0(\theta_2, \phi_2) & y_1{}^1(\theta_2, \phi_2) & \dots & y_L{}^L(\theta_2, \phi_2) \\ \vdots & \vdots & \vdots & \vdots & \vdots & \\ y_0{}^0(\theta_N, \phi_N) & y_1{}^{-1}(\theta_N, \phi_N) & y_1{}^0(\theta_N, \phi_N) & y_1{}^1(\theta_N, \phi_N) & \dots & y_L{}^L(\theta_N, \phi_N) \end{pmatrix}. \tag{2.25}$$

A standard standard least-squares regression carried out in MATLAB determines values for the harmonic coefficients vector $\hat{\mathbf{c}}$ that minimize the distance between the bounding surface data points $\hat{\mathbf{r}}$ and those estimated by $\mathbf{Y}\,\hat{\mathbf{c}}$. Consequently, the coefficients are determined by solving the equation

$$\hat{\mathbf{c}} = \left(\mathbf{Y}^T\,\mathbf{Y}\right)^{-1}\,\mathbf{Y}^T\,\hat{\mathbf{r}}. \tag{2.26}$$

2.6.3 Bounding surface fitting results

The bounding surface modeling approach detailed above is applied to the three general case studies considered in this paper. For the strong-axis, half, and weak-axis midspan blast cases, the bounding surface data and 4^{th} order real-valued spherical harmonic approximation to the radial yield function are depicted for all of the sampling points in Fig. 2.10, 2.11, and 2.12. The bottom plot in each set of figures consists of the approximated bounding surface shape colored by the error in fit at each sampling point. Each such error data point is calculated using a simple percent error formula, as

$$\% \; Error = \frac{r(\theta_i, \phi_i) - \hat{r}(\theta_i, \phi_i)}{\hat{r}(\theta_i, \phi_i)} \times 100\%, \tag{2.27}$$

where $r(\theta, \phi)$ is the approximation to the radial yield function in Eq. (2.21), and $\hat{r}(\theta, \phi)$ is the radial failure data point, obtained from Eq. (2.13). According to the convention of the above equation, a positive error value at a sampling point indicates a conservative fit at that point.

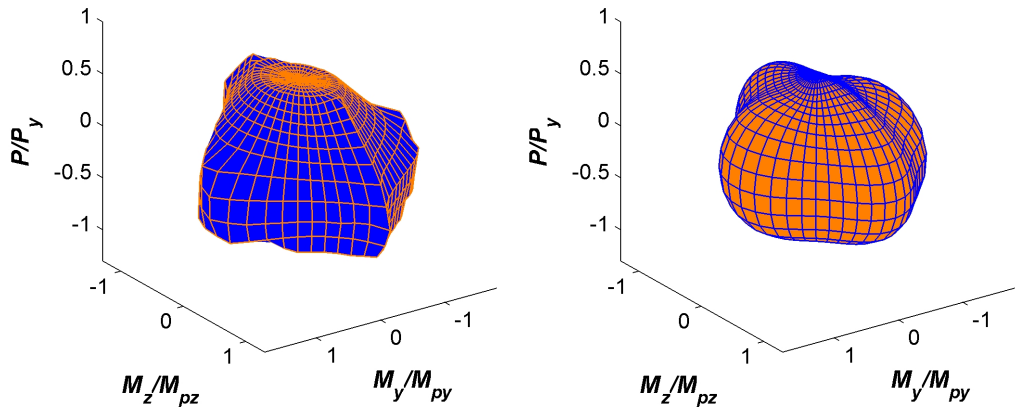

(a) Data

(b) Fit

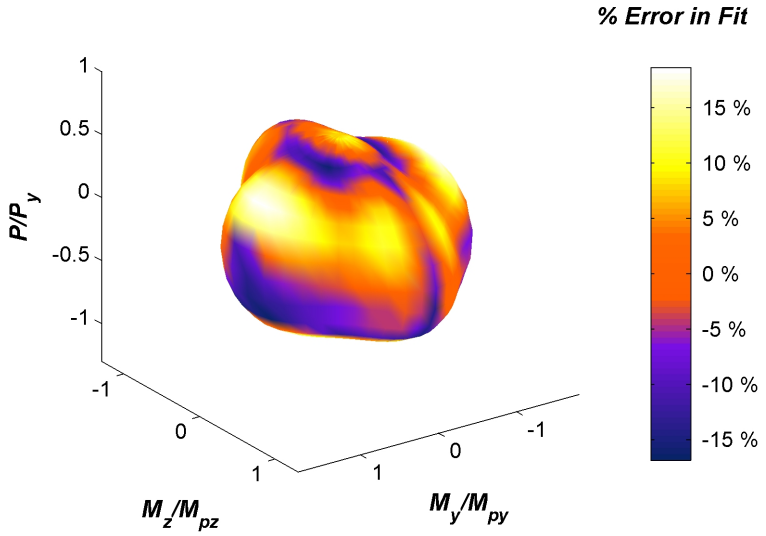

(c) Fit with Error

Figure 2.10: Comparison of bounding surface data and fit to data for a W360x57.8 (W14x38) member, L = 3.05 m long, that has been subjected to an explosion at $R_\perp$ = 6.10 m, $\Theta_\perp$ = 0 deg, and X = 0 m (strong-axis blast at midspan).

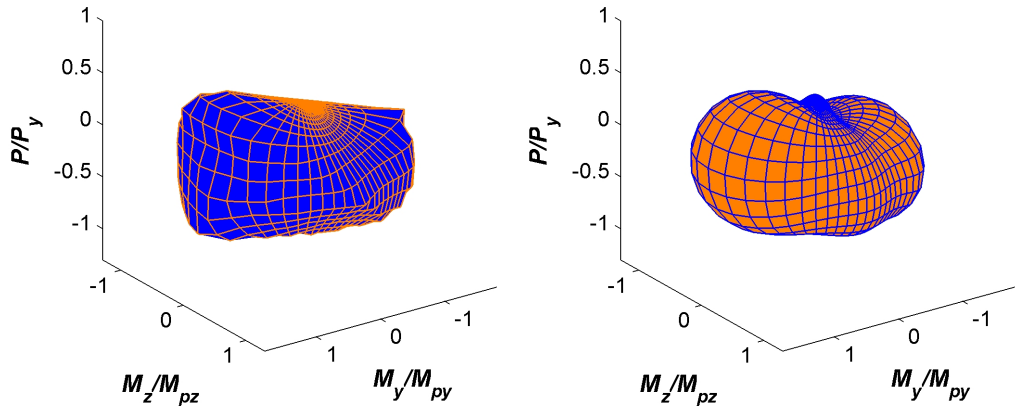

(a) Data

(b) Fit

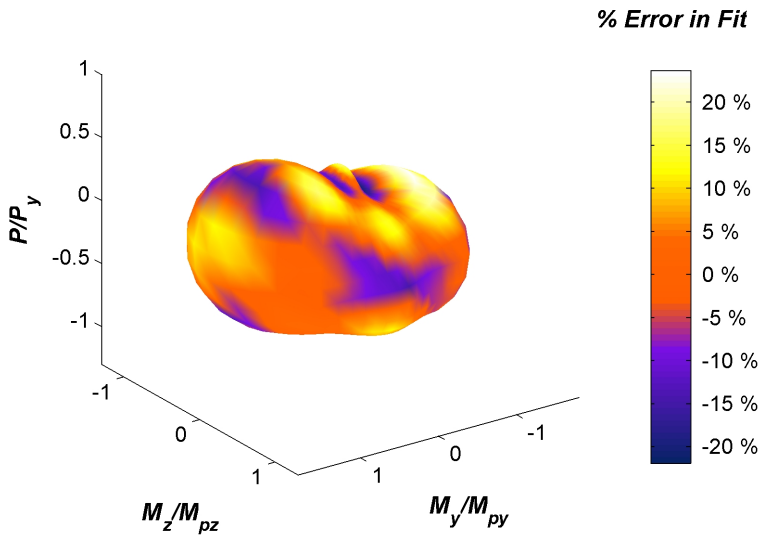

(c) Fit with Error

Figure 2.11: Comparison of bounding surface data and fit to data for a W360x57.8 (W14x38) member, $L = 3.05$ m long, that has been subjected to an explosion at $R_\perp = 8.23$ m, $\Theta_\perp = 45$ deg, and $X = 0$ m (half blast at midspan).

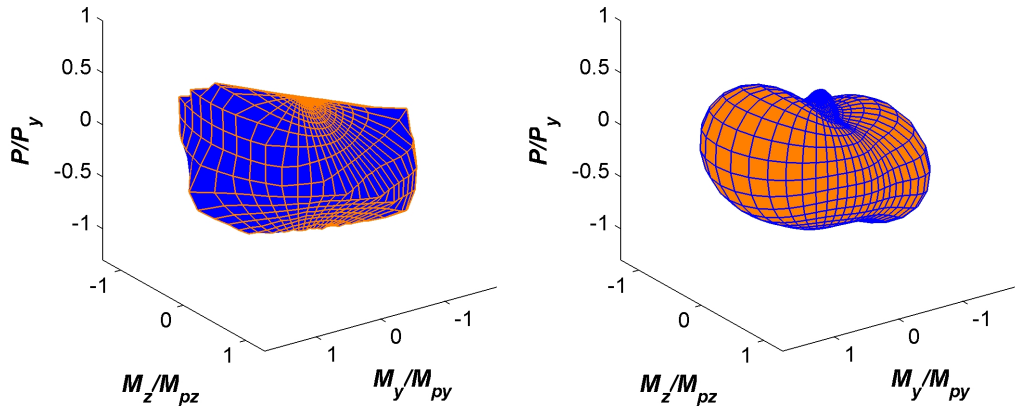

(a) Data

(b) Fit

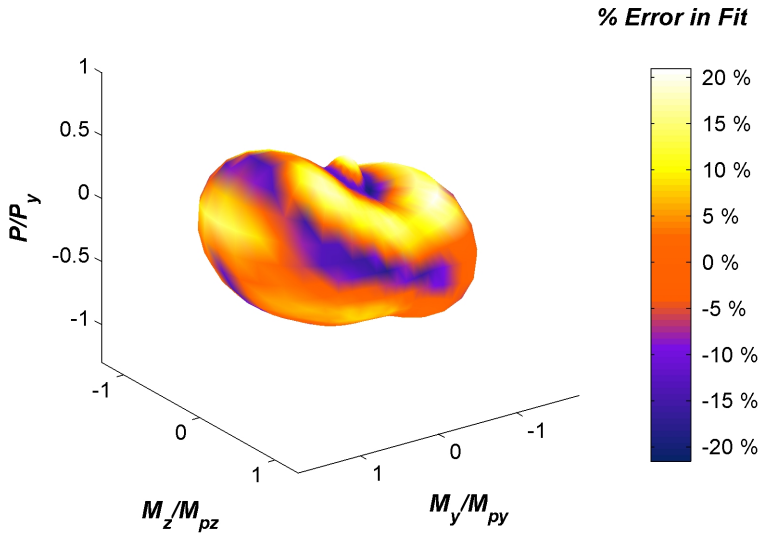

(c) Fit with Error

Figure 2.12: Comparison of bounding surface data and fit to data for a W360x57.8 (W14x38) member, $L = 3.05$ m long, that has been subjected to an explosion at $R_\perp = 14.63$ m, $\Theta_\perp = 90$ deg, and $X = 0$ m (weak-axis blast at midspan).

These figures show that the bounding surface modeling approach employed for this research, where the radial yield function is approximated with real-valued spherical harmonics, is able to capture the local features of the bounding surfaces with a smooth continuous function. The bounding surface models are not everywhere convex, but this is a reflection upon the underlying topology of the numerical bounding surface data.

For a quantitative, global evaluation of bounding surface fit, the bounding surface models defined by Eq. (2.21) are evaluated for goodness-of-fit using the following error metric based on a normalized ℓ_2 norm,

$$Error = \frac{\| r(\theta,\phi) - \hat{r}(\theta,\phi) \|_2}{N} = \frac{\sqrt{\sum_{i=1}^{N} [\, r(\theta_i,\phi_i) - \hat{r}(\theta_i,\phi_i) \,]^2}}{N}, \tag{2.28}$$

where N is the number of sampling points, $r(\theta,\phi)$ is the approximation to the radial yield function in Eq. (2.21), and $\hat{r}(\theta,\phi)$ is the radial failure data, obtained from Eq. (2.13). The error values calculated using this metric are displayed in Table 2.2 for the three general test cases. An error metric such as this might be useful when investigating how many data points to include within a given bounding surface for use in solving a practical problem.

Table 2.2: Error for 4$^{\text{th}}$ order real-valued spherical harmonic fit for radial distance to bounding surface for a W360x57.8 (W14x38) member, L = 3.05 m long, for blast at midspan.

Case	$R_\perp$ (m)	$\Theta_\perp$ (deg)	X (m)	*Error*
Strong-axis	6.10	0	0	2.26×10^{-3}
Half	8.23	45	0	1.82×10^{-3}
Weak-axis	14.63	90	0	1.99×10^{-3}

The error values indicate that the three cases exhibit similar levels of error in the spherical harmonic fit to the data, with the strong-axis blast case demonstrating a slightly worse fit.

2.7 Element implementation

The blast beam-column element is implemented in a nonlinear transient dynamic finite element code called *CU-BAMM*. The element implementation is discussed herein but code validation and case studies are included in the companion paper [29].

2.7.1 Dynamics

The developed code solves for displacement time histories by way of the standard equations for equilibrium that govern the dynamic response of a structural system idealized using finite elements,

$$\mathbf{M}\ddot{\mathbf{U}} + \mathbf{C}\dot{\mathbf{U}} + \mathbf{K}\mathbf{U} = \mathbf{Q}, \tag{2.29}$$

where $\mathbf{M}$ is the mass matrix, $\mathbf{C}$ is the damping matrix, and $\mathbf{K}$ is the total stiffness matrix. Here, the vectors $\mathbf{U}$ and $\mathbf{Q}$ represent nodal displacements and applied loads, respectively. The total stiffness matrix includes a linear elastic part, in addition to geometrically nonlinear and material nonlinear components. The geometric nonlinearity follows the standard formulation for large-displacement/large-strain relationships for a traditional frame element in an updated Lagrangian framework [48].

Damping is neglected and so Eq. (2.29) can be simplified to be of the following form at time t (the last converged solution)

$$\mathbf{M}\ddot{\mathbf{U}}^t + \mathbf{F}^t = \mathbf{Q}^t, \tag{2.30}$$

where the internal force vector is assumed to be $\mathbf{F}^t = \mathbf{K}\mathbf{U}^t$, thus necessitating

small step sizes (which is practically achieved in light of time stepping, as discussed later). In accordance with the incremental nonlinear analysis algorithm implemented within the code, $\mathbf{F}^t$ is the internal force in the structure associated with the previously converged time step.

Explicit time integration is employed within the code. The standard central difference expansion of the acceleration vector at time t is thus

$$\ddot{\mathbf{U}}^t = \frac{1}{\Delta t^2}\left(\mathbf{U}^{t-\Delta t} - 2\mathbf{U}^t + \mathbf{U}^{t+\Delta t}\right), \tag{2.31}$$

where Δt is the time increment and $\ddot{\mathbf{U}}$ and $\mathbf{U}$ represent nodal acceleration and displacement, respectively.

Combining Eq. (2.30) and (2.31) gives the temporally discretized governing equation in terms of the unknown displacement at the current solution time,

$$\mathbf{U}^{t+\Delta t} = \frac{\Delta t^2}{\mathbf{M}}\left(\mathbf{Q}^t - \mathbf{F}^t\right) + 2\mathbf{U}^t - \mathbf{U}^{t-\Delta t}. \tag{2.32}$$

Following the updated Lagrangian methodology, the code is formulated in terms of incremental displacements, and so at each time, the code determines the displacement increment

$$\mathbf{dU}^{t+\Delta t} = \frac{\Delta t^2}{\mathbf{M}}\left(\mathbf{Q}^t - \mathbf{F}^t\right) + \mathbf{dU}^t, \tag{2.33}$$

which is then added to the previously converged displacement $\mathbf{U}^t$ to solve for the displacement via the expression

$$\mathbf{U}^{t+\Delta t} = \mathbf{U}^t + \mathbf{dU}^{t+\Delta t}. \tag{2.34}$$

Mass lumping is employed, which produces a diagonal mass matrix that is easily invertible for calculation of the displacement increment, $\mathbf{dU}^{t+\Delta t}$, in Eq.

(2.33). The diagonal components of $\mathbf{M}$ are calculated as $(m_t) = \frac{1}{2}AL\rho$ for translational degrees of freedom, and $(m_r) = \frac{1}{24}AL^3\rho$ for rotational degrees of freedom, where A is the element cross-sectional area, L is the element length, and ρ is the material density [9, 22].

The central difference method, as applied to the governing system in Eq. (2.29), is conditionally stable, and so to ensure numerical stability of the solution, the size of the time steps must be limited. The code obeys the Courant condition, whereby the time step is constrained to be below a critical value, Δt_{cr}, which is the upper bound for accurate representation of a traveling wave within an element. For a beam element, the critical time step size is taken as

$$\Delta t_{cr} = \min\left(\frac{L}{c},\ \frac{L^2}{c}\sqrt{\frac{A}{48I}}\right), \tag{2.35}$$

where A is the cross-sectional area, L is the element length, I is the moment of inertia, and $c = \sqrt{E/\rho}$ is the one-dimensional material wave speed. Additionally, E is the modulus of elasticity, ρ is the material density, L/c is the critical time step associated with the period for longitudinal motion, and $L^2/c\ \sqrt{A/48I}$ corresponds to the critical time step for flexural motion [9].

2.7.2 Bounding surface gradient

As previously mentioned, the system stiffness matrix $\mathbf{K}$ includes material nonlinearity imparted by the plastic reduction matrix $\mathbf{K_m}$, which is calculated using the gradient to the element bounding surface. The radial yield function, $r(\theta, \phi)$, gives the radial length from the origin to the bounding surface for a given colatitude and longitude pair in normalized stress-resultant space. However, while $r(\theta, \phi)$ does provide a mathematical model of the bounding surface, this func-

tional form is not expressed as a surface equation in stress-resultant space. Consequently, the gradient to the non-normalized bounding surface, $\nabla\Phi$, must be calculated numerically.

The gradient calculation involves a two-step process. First, the gradient to the normalized bounding surface at the force point defined by $r(\theta, \phi)$ is approximated by the normal to the plane passing through the three nearest bounding surface points. These points are located at $r(\theta+\epsilon, \phi+\epsilon)$, $r(\theta-\epsilon, \phi)$, and $r(\theta+\epsilon, \phi-\epsilon)$, where ϵ is an arbitrarily selected small number. The components of the normal to the plane are then normalized by the plastic section capacities P_Y, M_{py}, and M_{pz} to give $\nabla\Phi$ in stress-resultant space by way of the chain rule.

2.7.3 Automatic time incrementation and elastic unloading

The developed code includes measures to address problems involving inadmissible force points and elastic unloading.

Automatic time incrementation

Automatic time incrementation is used by the code to ensure that each increment in displacement results in a new force point at an admissible location in stress-resultant space. For a given force vector $\mathbf{F} = \left\{P \;\; M_y \;\; M_z\right\}$ at an element end, the code first evaluates the radial yield function to determine the distance to the bounding surface along the path of the force vector in normalized stress-resultant space. Yielding is defined in terms of the length, R, of the normalized

force vector

$$R = \sqrt{\left(\frac{P}{P_Y}\right)^2 + \left(\frac{M_y}{M_{py}}\right)^2 + \left(\frac{M_z}{M_{pz}}\right)^2}, \tag{2.36}$$

and the condition defining the state of plastic yield can be expressed as

$$r(\theta, \phi) = R, \tag{2.37}$$

where $r(\theta, \phi)$ is the radial yield function. Following the assumption of elastic-perfectly plastic material behavior at the element ends, it follows that $R < r(\theta, \phi)$ indicates an elastic state, and $R > r(\theta, \phi)$ is inadmissible.

The developed code uses an automatic time-stepping algorithm to prevent force points outside of the bounding surface, ensuring that a given increment in displacement does not produce a new force point outside of the bounding surface. If the trial increment, $\mathbf{dU}^{t+\Delta t}$, results in a force point that breaches the bounding surface, the time step is cut in half and a new trial increment is calculated. When changing the time step size, the forward (trial) and backward displacement increments must both be modified to maintain consistency with the governing equation as derived using a central difference assumption. The new backward increment is linearly interpolated between previously calculated converged points, and is expressed as

$$\mathbf{dU}^{t'} = \mathbf{U}^{t} - \mathbf{U}^{t-\Delta t'} \approx \frac{\Delta t'}{\Delta t}\left(\mathbf{U}^{t} - \mathbf{U}^{t-\Delta t}\right), \tag{2.38}$$

where Δt is the old time step and the new step is $\Delta t' = \Delta t/2$. Consequently, the new trial increment is

$$\mathbf{dU}^{t+\Delta t'} = \frac{\Delta t'^2}{\mathbf{M}}\left(\mathbf{Q}^{t} - \mathbf{F}^{t}\right) + \mathbf{dU}^{t'}. \tag{2.39}$$

Following a series of successful time increments, the time step can be increased by a factor of two in a similar manner.

Elastic unloading

Another situation requiring special attention is elastic unloading. Once an element end has formed a plastic hinge, it is possible for the end to unload elastically as a result of force redistribution under the action of continued load application. Elastic unloading is usually indicated by a negative value in the vector of plastic deformation magnitudes, or λ from Eq. (2.7) [48]. Thus if negative values are detected in λ for any element, the code allows the end to unload elastically by reforming the plastic reduction matrix using null values for $\mathbf{G}$ at the corresponding element end and then reattempting the time step. This is similar to the procedure detailed in [48], although the increment is with respect to time rather than applied load.

2.8 Conclusions

The present paper has introduced a possible method for extending the usefulness of frame structural elements in evaluating the reserve capacity of structural systems in the post-blast, damaged condition. The discussed approach endeavors to capture salient local and global damage features within the context of a bounding surface formulated in stress-resultant space. A series of three general case studies, carried out on a W360x57.8 (W14x38) wide-flange member, L = 3.05 m (L = 10 ft) long, demonstrate the bounding surfaces for the damaged member configuration resulting from different blast locations, where these surfaces are defined by the locus of numerous failure data points acquired in a series of virtual load tests performed on a simulated blast-damaged member. Fits to the bounding surface data are achieved through the use of linear combi-

nations of real-valued spherical harmonics. The blast beam-column element is implemented within a nonlinear explicit finite element code developed to perform limit state computations for blast-resistant design. Code validation and example problems are included in the companion paper [29].

2.9 Acknowledgment

This paper is based upon research supported by Cornell University and a National Science Foundation Graduate Research Fellowship. Any opinions, findings, conclusions or recommendations expressed in this publication are those of the authors and do not necessarily reflect the views of the National Science Foundation. The authors would also like to acknowledge the contributions made to this research by Heather Reed at Cornell University.

CHAPTER 3

SIMULATING BLAST EFFECTS ON STEEL BEAM-COLUMN MEMBERS: APPLICATIONS

3.1 Abstract

Validation and application examples are presented for a beam-column element that uses bounding surface plasticity models to characterize the effects of damage imposed by an explosion on structures composed of steel wide-flange members. The formulation of the blast beam-column element and its implementation within the nonlinear explicit dynamic finite element code *CU-BAMM* is included in the companion paper [30]. The current paper details the creation of a library of bounding surfaces for various wide-flange members and explosive scenarios, and the implementation of this library within the code. A validation example shows favorable agreement between *CU-BAMM* simulation results and results obtained from a high-resolution model for the prediction of the post-blast collapse load for a steel A-frame subjected to an explosion. A series of additional example problems are also presented to highlight applications of the code.

3.2 Introduction

Terrorist attacks in recent years have generated concern over a general vulnerability to blast seen in many conventionally designed structures, with localized blast damage causing global collapse in some cases [23]. Currently,

accurate prediction of system response to an explosion necessitates expensive high-resolution modeling techniques that employ shell or continuum element discretization of individual structural components. However, in a companion paper [30] the authors propose a more computationally efficient method for modeling the reserve capacity of blast-damaged structural members, which is based on a blast beam-column element formulation that uses bounding surface plasticity models to capture the effects of component-level damage. The blast beam-column element is implemented within the nonlinear explicit dynamic finite element code *CU-BAMM*, in order to enable the application of frame elements in the study of blast-damaged systems. Consequently, one of the objectives of the current research is to validate the blast beam-column approach against a suitable benchmark.

A second objective for this research is to present a numerical example for the simulated response of a more practically relevant steel skeletal structural system subjected to a blast, as predicted by the developed code. In order to do this, however, a library of bounding surface plasticity models must be created for a variety of wide-flange members and explosive scenarios, since each bounding surface is strongly dependent upon a set of parameters describing a member and its location with respect to a specific blast. The blast beam-column elements in a structural system inevitably vary in size, shape, and orientation with respect to the blast epicenter, and so the developed code interacts with the library to scan library entries to find the closest approximation for the parameter set of an individual element. Details of the library creation and implementation within *CU-BAMM* are discussed herein.

This paper is the second of two companion papers to formulate, implement, and validate a beam-column element for the simulation of air blast effects in steel skeletal structures constructed of wide-flange components. Validation and examples are included in this paper, and the element formulation and implementation are presented in the companion paper [30].

3.2.1 Literature review

Validation of a numerical approach to modeling a complex system involves comparison of simulation results with experimental data. Several sets of physical test data exist for steel wide-flange members subjected to explosive loading. Lawver et al. [43] have conducted full-scale experiments on a selection of W360 (W14) series AISC bare steel columns subjected to explosions positioned at various distances from the specimens. By comparing the test data with numerical results, both from a single degree-of-freedom (SDOF) analysis and a high-resolution analysis, performed with the explicit, large displacement finite element program FLEX (similar to LS-DYNA), Lawver et al. conclude that FLEX is able to accurately predict permanent deformation (*i.e.* peak transverse displacement at different column heights, global buckling, etc.) caused by a blast.

Magallanes et al. [46] present results from a full-scale experiment in which a W360x347 (W14x233) column, 5.72 m (18.75 ft) long, is subjected to a large explosion on a slant to the column face. The test column is encased in brick cladding, which is entirely destroyed by the action of the blast.

A series of publications presents the results of a multi-year research effort, carried out by Myers, Houghton & Partners, Inc. (MHP) for the General Ser-

vices Administration (GSA), to investigate the blast and progressive collapse resistance of conventional welded steel frame structures [37, 38, 39]. This research endeavor, referred to as the GSA Test Program, includes a combination of predictive and post-blast numerical simulations of steel frames with full-scale blast testing and post-blast monotonic testing of the same test articles. The analyses explicitly model critical elements of the connections, anchorages, and the reinforced concrete cladding surrounding the frame assembly.

However, while all of the above sources of experimental data provide qualitative insights regarding the behavior of steel wide-flange members under the influence of an explosion, they are not useful for quantitative validation of the developed blast beam-column approach. In all cases except for [46], no mention is made of the combination of charge weight and standoff used to produce test results, presumably for security reasons. Thus, the blast loading experienced by the members in these experiments cannot be modeled with any degree of certainty. Additionally, while the experiments on the encased steel column [46] and the steel frame assembly with adjacent reinforced concrete cladding wall are valuable, they are obviously not applicable for quantitative validation of a code that models the response of bare steel sections exposed to an explosion.

It is widely accepted that numerical tools are an effective alternative to costly full-scale experiments, especially in situations where there is a lack of openly available, relevant physical test data. Thus, the research herein pursues model validation by comparing results obtained for a system simulated using the proposed approach and a high-resolution analog to the blast beam-column model.

3.2.2 Paper organization

An overview of the blast beam-column element formulation is given in Section 3.3 of the current paper, while Section 3.4 details the creation of the bounding surfaces library and its implementation within the developed code. Section 3.5 demonstrates the use of the blast beam-column approach to model a single member under the force of a blast, and Section 3.6 investigates an A-frame exposed to an explosion where the code results are validated against those from a high-resolution model. Section 3.7 presents a more practical numerical example using the developed code to model the behavior of a three-dimensional through-truss subjected to an explosion. Final conclusions are drawn in Section 3.8.

3.3 Overview of blast beam-column element formulation

The following constitutes a brief overview of the blast beam-column element formulation, included here as necessary background for the subsequent discussion of the creation of a library of bounding surface plasticity models. As detailed in the companion paper [30], the blast beam-column element takes as its point of departure the traditional frame element in [48]. In contrast to the behavior of individual member ends as specified in the traditional frame element formulation, the bounding surface that governs inelastic behavior for the blast beam-column element is based on failure modes within an entire member, either buckling or an excessive strain level anywhere within the member.

The numerical failure data used as the basis for the blast beam-column element bounding surface models is acquired in a series of virtual load tests of blast-damaged members, carried out using the commercial finite element package, LS-DYNA [31]. The failure data for a single bounding surface is obtained by subjecting a detailed shell element-based model of an individual wide-flange member to a simulated explosion, and subsequently loading the damaged member to collapse, as described in the following procedure:

1. Select parameters defining the current bounding surface (*i.e.* geometry, material, etc. for the member and blast)
2. Perform a nonlinear dynamic analysis to simulate the structural response to the blast and resulting damage sustained by the member
3. Loop over a series of axial load and biaxial moment combinations
    - For each moment-thrust combination, perform a collapse analysis to determine the force point at failure (defined by either load-shedding or excessive straining)
4. Compile failure force point data to give a point cloud (in stress-resultant space) that represents the bounding surface for that member, for the chosen explosive scenario

Additional details concerning this approach may be found within the companion paper [30]. In the above, the failure strain ϵ_{fail} is defined to be the strain level at which strain-hardening commences in ASTM-A36 steel, equal to an engineering strain of $\epsilon_{st} = 0.0203$ [5].

The point cloud of failure force point data is fitted to a real-valued basis of spherical harmonics, $y_l^m(\theta, \phi)$, to provide a functional approximation to the

blast bounding surface data examined in this and the companion paper [30]. Real-valued spherical harmonics are a complete set of orthonormal functions [24, 19], and are defined as [12]

$$y_l{}^m(\theta,\phi) = \begin{cases} \sqrt{2}\ N(l,m)\ P_l{}^m cos(\theta)\ cos\, m\phi, & m > 0, \\ Y_l{}^0(\theta,\phi), & m = 0, \\ \sqrt{2}\ N(l,m)\ P_l{}^m cos(\theta)\ sin\, |m|\phi, & m < 0, \end{cases} \tag{3.1}$$

where the variable l denotes the harmonic degree, the integer m is the order, which is constrained to $-l < m < l$ [24], and the normalization function $N(l,m)$ is given by [12]

$$N(l,m) = \sqrt{\frac{(2l+1)}{4\pi}}\sqrt{\frac{(l-m)!}{(l+m)!}}. \tag{3.2}$$

Additionally, $P_l{}^m cos(\theta)$ are the well-known Legendre polynomials that are defined with respect to Cartesian coordinates as [17, 12]

$$P_l{}^m(x) = \frac{(-1)^m}{2^l\ l!}(1-x^2)^{\frac{m}{2}}\frac{\partial^{\,l+m}}{\partial x^{\,l+m}}(x^2-1)^l, \tag{3.3}$$

and can be converted to $P_l{}^m cos(\theta)$ by substituting $x = \cos\theta$ in the above [42, 17]. As detailed in the companion paper [30], the radial yield function for the blast beam-column element is given by the following series

$$r(\theta,\phi) \approx \sum_{l=0}^{4}\sum_{m=-l}^{l} c_l{}^m\ y_l{}^m(\theta,\phi), \tag{3.4}$$

where the 25 harmonic coefficients $c_l{}^m$ corresponding to this 4^{th} order series truncation are fitted to the force point data using standard least-squares regression. Additionally, θ is the colatitude, $\theta \in [0\ \pi]$, and ϕ is the longitude, $\phi \in [0\ 2\pi)$, as is typical for spherical coordinates. The colatitude and longitude can be calculated using the following Cartesian-to-spherical coordinate conversions:

$$\theta = \theta(p, m_y, m_z) = \arccos\left\{\frac{p}{\sqrt{m_y{}^2 + m_z{}^2 + p^2}}\right\}, \tag{3.5}$$

and

$$\phi = \phi(p, m_y, m_z) = \text{atan2}(m_z, m_y), \tag{3.6}$$

where p, m_y, and m_z represent coordinates in normalized stress-resultant space,

$$p = P/P_Y, \tag{3.7}$$

$$m_y = M_y/M_{py}, \tag{3.8}$$

and

$$m_z = M_z/M_{pz}. \tag{3.9}$$

Following the general convention, these coordinates represent a dimensionless version of the element end forces, P, M_y, and M_z; here, the element end forces are normalized by the plastic section capacities P_Y, M_{py}, and M_{pz}, which are the squash load and minor and major axis plastic bending moments, respectively [48].

The gradient to the bounding surface with respect to element end forces is a key aspect of the blast beam-element formulation. The damage caused by a blast is incorporated into the blast beam-element by way of a plastic reduction matrix, $\mathbf{K_m}$, the general from of which is given as [48, 49]

$$\mathbf{K_m} = -\frac{\mathbf{K_T}\,\mathbf{G}}{\mathbf{G}^T\,\mathbf{K_T}\,\mathbf{G}}\,\mathbf{G}^T\,\mathbf{K_T}, \tag{3.10}$$

where $\mathbf{K_T} = \mathbf{K_e} + \mathbf{K_g}$ is the elastic tangent stiffness matrix, $\mathbf{K_e}$ is the linear elastic stiffness matrix, and $\mathbf{K_g}$ is the initial stress matrix. The gradient to the bounding surface, $\nabla\Phi$, at element ends 1 and 2 appears in the matrix $\mathbf{G}$ as

$$\mathbf{G} = \begin{bmatrix} \mathbf{G_1} & 0 \\ 0 & \mathbf{G_2} \end{bmatrix} = \begin{bmatrix} \nabla\Phi_1 & 0 \\ 0 & \nabla\Phi_2 \end{bmatrix}. \tag{3.11}$$

Vectors $\mathbf{G_1}$ and $\mathbf{G_2}$ are null if their respective element end force points do not persist on the bounding surface, and so the matrix $\mathbf{G}$ only has nonzero elements

at entries corresponding to an element end whose force point is impinging on the bounding surface [48, 49]. Since the yield function of the blast beam-column element is based on failure of an entire wide-flange member, if the element end force combination at either member end impinges on the associated bounding surface, then the *member* is assumed failed, and both ends assigned nonzero entries in $\mathbf{G}$. Also, note that since the radial yield function in Eq. (3.4) is not expressed as a surface equation in stress-resultant space, the gradient to the non-normalized bounding surface, $\nabla\Phi$, is calculated by way of a numerical approximation, rather than explicitly, within the code, as discussed in the companion paper [30].

The plastic reduction matrix is included as part of the system stiffness matrix for the blast beam-column element, in the usual manner for an updated Lagrangian formulation. Thus, the relationship between the increment in the internal force vector, $\mathbf{dF}$, and the increment in displacement at both element ends, $\mathbf{dU}$, for the element is

$$\mathbf{dF} = \left(\mathbf{K_e} + \mathbf{K_g} + \mathbf{K_m}\right)\mathbf{dU} = (\mathbf{K_T} + \mathbf{K_m})\,\mathbf{dU} = \mathbf{K}\,\mathbf{dU}, \tag{3.12}$$

for material and geometrically nonlinear analyses, where $\mathbf{dU}$ can be decomposed into an elastic part, $\mathbf{dU_e}$, and a plastic part, $\mathbf{dU_p}$ to give $\mathbf{dU} = \mathbf{dU_e} + \mathbf{dU_p}$.

3.4 Library of bounding surfaces

Since each blast beam-element bounding surface is strongly dependent upon a parameter set describing a member and its location with respect to a specific blast, a comprehensive bounding surface data acquisition effort is carried out in order to populate a library of bounding surface plasticity models for a variety of

wide-flange members and explosive scenarios. Different cross-sections, lengths, charge weights, and stand-off distances are considered. For each combination of parameters, failure data are obtained through an automated process, carried out in parallel within a distributed memory context, and then fitted to a radial yield function that is a linear combination of real-valued spherical basis functions, following Eq. (3.4).

3.4.1 High-resolution general model and approach

All explosive (dynamic) and post-blast collapse (static) finite element simulations use the same general base model and approach, with variable blast location and member geometry. The base model of the wide-flange member is comprised of a mix of shell and beam elements, with simply supported boundary conditions. The web and flanges are modeled with Belytschko-Lin-Tsay shell elements [31] with element thickness equal to the appropriate plate thicknesses within the given steel wide-flange cross-section. Very stiff Belytschko-Schwer [31] beam elements are placed along the web and flanges at the member ends, in order to suppress cross-sectional distortion at the support locations.

The beam elements are circular in cross-section with a diameter of 25.4 mm, and are perfectly elastic, with $\nu = 0.3$ and $E = 20,300$ GPa, which is 100 times the stiffness of the shell element material. A mesh seed of 6 elements per flange outstand, applied globally to the model, provides sufficient resolution to capture local deformation effects induced by an explosion, as determined by a mesh convergence study.

Rate-dependent and strain-hardening material behavior are accounted for by using the simplified form of the Johnson-Cook constitutive relationship to model the flow stress in the hot-rolled steel wide-flange members,

$$\sigma_{flow} = \left[A + B\left(\varepsilon_{ep}\right)^{n}\right]\left[1 + C\, ln\, \dot{\varepsilon}^{*}_{ep}\right], \tag{3.13}$$

where A, B, n, C, and m are material constants, ε_{ep} is the effective plastic strain, and the expression $\dot{\varepsilon}^{*}_{ep} = \dot{\varepsilon}_{ep}/\dot{\varepsilon}_0$ denotes the dimensionless plastic strain rate, which has been normalized by $\dot{\varepsilon}_0$, the quasistatic strain rate used for the experimental determination of the strain hardening parameters, B and n. For ASTM-A36 steel, the Johnson-Cook parameter values are $A = 244.764$ MPa, $B = 483.929$ MPa, $C = 1.6503 \times 10^{-2}$, $n = 0.23505$, $\dot{\varepsilon}_0 = 1.9457 \times 10^{-4}$ s^{-1} [57, 55, 56] and the material constants are $E = 199.4$ GPa, $\nu = 0.3$, and $\rho = 7850$ kg/m^3.

Air blast loading is applied over structural surfaces in direct line of sight of the explosion using a blast load generation code previously developed by the authors [28]. Acting as a preprocessor to LS-DYNA, the air blast load generation code calculates spatially and temporally varying blast loads for a given explosive scenario, where these loads are then applied as nodal force time histories within the LS-DYNA finite element model.

Dynamic analyses are carried out to a total solution time of 1300 ms, where mass damping (5%) is applied after 750 ms in order to generate the final deformed shape of the wide-flange member by the end of the analysis. The damping force is assumed to be proportional to the velocity, with a proportionality constant equal to the damping ratio, ζ, multiplied by twice the fundamental frequency of the structure, where $\zeta = 0.05$.

To ensure a uniform critical time step size for the entire model, the density of the cross-section-stiffening beam elements is modified so that the critical time

step size, used for the automatic time stepping, is similar for both the shell and beam elements. Consequently, the material density of the beam elements is set to be $\rho = c\,\rho_{shell}$, where ρ_{shell} is the density of the shell elements and c is a constant greater than unity ($c > 1$) whose value depends on the shell element size.

As a follow-up to the dynamic blast analysis, the damaged member is loaded to failure in a static collapse analysis, where the deformed geometry and residual strain field from the end of the dynamic blast simulation are used to initialize each static analysis. For an individual collapse analysis, combined loading representing a vector in stress-resultant space is applied proportionally as $LPF \cdot \left\{P\ M_y\ M_z\right\}$, where the load proportionality factor, LPF, is increased until either of the two previously defined failure criteria (instability or strain-to-failure) is met. Each loading vector is defined such that the Euclidean norm of the loading vector when normalized by the plastic section capacities is equal to LPF, meaning that $\sqrt{\left(\frac{P}{P_Y}\right)^2 + \left(\frac{M_y}{M_{py}}\right)^2 + \left(\frac{M_z}{M_{pz}}\right)^2} = 1$. Thus, the value of the load proportionality factor (LPF) at failure, equal to $\max(LPF)$, actually represents the radial distance $\hat{r}(\theta, \phi)$ from the origin along the current loading vector to the bounding surface in normalized stress-resultant space for the member and blast scenario of interest, or

$$\hat{r}(\theta, \phi) = \max(LPF), \tag{3.14}$$

where θ is the colatitude and ϕ is the longitude from Eq. (3.5) and (3.6). In order to obtain data representing the blast-damaged bounding surface for a given member and explosive scenario, multiple separate collapse analyses are performed for loading vectors at various evenly spaced θ and ϕ over a spherical sampling grid in stress-resultant space. Per previous work for the companion paper, this grid has 13 latitude and longitude lines of unit radius per octant, for a total of 1106 sampling points per bounding surface [30].

3.4.2 Library parameter space

The parameters affecting the bounding surface topology, including member length, cross-sectional proportions, material, boundary conditions, and blast size and location with respect to the member, are chosen such that the library has entries applicable within a reasonable array of structural contexts.

For the library, attention is limited to the following common hot-rolled wide-flange sections: W360x57.8 (W14x38), W360x122 (W14x82), W360x162 (W14x109). These sections span a range of uses in design, since the W360x57.8 is typically used as a beam, and the W360x162 as a column, yet they are of the same W360 (W14) series, as may be the case within a single structural system to ensure connection compatibility. Cross-section geometrical properties are included in Table 3.1.

Table 3.1: Cross-section geometrical properties [2].

Cross-section	A_g (mm^2)	d (mm)	t_w (mm)	b_f (mm)	t_f (mm)	Z_z (mm^3)	Z_y (mm^3)
W360x57.8 (W14x38)	7230	358	7.87	172	13.1	1010	198
W360x122 (W14x82)	15500	363	13.0	257	21.7	2280	734
W360x162 (W14x109)	20600	363	13.3	371	21.8	3150	1520

The plastic section capacities are calculated in the usual manner for each of the cross-sections. Accordingly, the squash load is $P_Y = F_Y A_g$, the weak-axis plastic moment is $M_{py} = F_Y Z_y$, and the strong-axis plastic moment is $M_{pz} = F_Y Z_z$ [2], where A_g is the gross cross-sectional area and Z_y and Z_z are the respective principal axis plastic section moduli. A yield stress value of $F_Y = 244.764$ MPa (35.5 ksi) is used for the ASTM-A36 steel, to be consistent with the value of the yield stress constant, A, assumed for all high-resolution models in the simplified Johnson-Cook constitutive relationship in Eq. (3.13). Plastic section capacities

for the three cross-sections are included in Table 3.2.

Table 3.2: Cross-section plastic capacities, ASTM-A36 steel.

Cross-section	P_Y (kN)	M_{py} (kN-m)	M_{pz} (kN-m)
W360x57.8 (W14x38)	1769	48.5	246.7
W360x122 (W14x82)	3806	179.7	557.5
W360x162 (W14x109)	5053	371.8	770.1

Each cross-section is investigated for two lengths, where each unbraced length L is chosen to be between the plastic limit and elastic limit of lateral-torsional buckling ($L_p < L < L_r$), so that L is in the range for inelastic lateral-torsional buckling. Consequently, the investigated lengths are $L = 3.05, 4.57$ m for the W360x57.8 section, $L = 4.57, 6.10$ m for the W360x122 section, and $L = 6.10, 7.62$ m for the W360x162 section.

Following the convention proposed in the companion paper [30], blast locations are cataloged as a function of the following three parameters, illustrated in Fig. 3.1:

- $R_\perp$: the perpendicular distance from the blast source point to the element longitudinal axis
- X: the distance along the element longitudinal axis to the intersection with the vector denoting the perpendicular distance from the blast source point to the element longitudinal axis
- $\Theta_\perp$: the angle between the normal to the member longitudinal axis that is coplanar with the member web, and the vector from the blast source point to the element longitudinal axis along the shortest path (of length $R_\perp$)

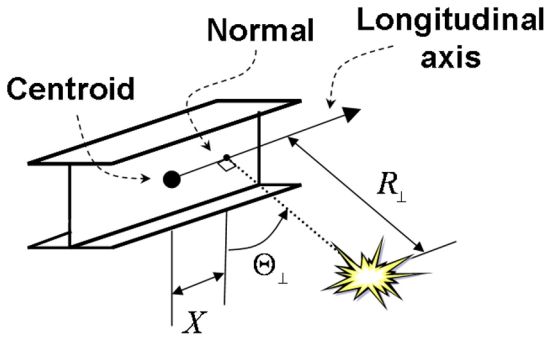

Figure 3.1: Blast location defined as a function of $R_\perp$, $\Theta_\perp$, and X, where $\Theta_\perp = 45$ deg and $X = L/4$ is shown here.

Three separate cases of perpendicular loading angle ($\Theta_\perp$) are considered for each member to represent a variety of response modes: strong-axis blast ($\Theta_\perp = 0$ deg), half blast ($\Theta_\perp = 45$ deg), and weak-axis blast ($\Theta_\perp = 90$ deg).

Various parallel longitudinal position (X) values are chosen, where each is expressed as a ratio of the member length: $X = 0, L/4, L,$ and $5L/2$. The first two cases produce the most structural damage, with $X = 0$ representing a blast located perpendicular to the member midspan and $X = L/4$ a blast perpendicular to the member quarter-point.

Two values of perpendicular distance ($R_\perp$) are investigated at each perpendicular loading angle ($\Theta_\perp$) for a given member. The same $R_\perp$ values are used at each of the four parallel longitudinal positions. For a given member and $\Theta_\perp$, this produces an inner set of explosions located at $(R_\perp)_{inner}$ and an outer set of explosions located at $(R_\perp)_{outer}$. The outer perpendicular distance is actually determined as $(R_\perp)_{outer} = 1.5(R_\perp)_{inner}$ for each perpendicular loading angle, for a given member. A schematic of the selection process is shown in Fig. 3.2, where only the plan view of the weak-axis blast case is shown, for clarity.

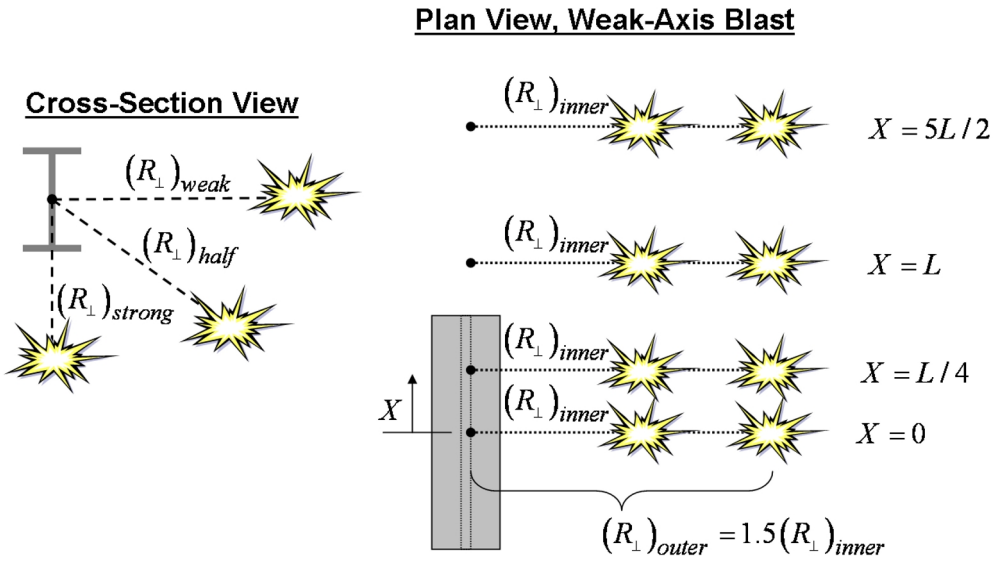

Figure 3.2: Standoff distances and spatial variation in blast locations for each member.

The inner perpendicular distance ($(R_\perp)_{inner}$) is determined in the following manner for each perpendicular loading angle $\Theta_\perp$. For a given member (and $\Theta_\perp$), $R_\perp$ is iterated on in 0.15 m (0.5 ft) increments for midspan blast ($X = 0$) until a value is reached such that the maximum effective plastic strain over the model domain is slightly less than the failure strain, or until $\max(\epsilon_{ep}) \approx 0.01887$. This represents a standoff distance for midspan blast that comes very close to causing failure of the member through the action of the (dynamic) explosion alone. In general, should the member develop a plastic strain in excess of the strain failure criterion, or $\max(\epsilon_{ep}) = 0.01887$, the bounding surface would be undefined. Since explosions not located at the midspan or at the inner perpendicular distance cause less damage to a member, then this blast location represents the worst case scenario for which the blast beam-column element approach is valid.

The cross-section and length combination together are considered a *member* and the set of blast parameters $R_\perp$, $\Theta_\perp$, and X constitute an *explosive scenario*

for the ensuing discussion. The bounding surface also depends on the member material, but for this research only ASTM-A36 steel is considered and so this variable is not treated separately within the code at this time. Additionally, the bounding surface would also depend on the explosive weight and charge type, but only $W = 453.6$ kg (1000 lb) equivalent TNT spherical explosions are examined in this research and, so these explosive characteristics are not treated explicitly within the current code, aside from error-checking of model inputs. Thus, each bounding surface is formed for a given set of parameters describing both the member and the explosive scenario, as defined above.

The above choices in cross-section, length, perpendicular loading angle, parallel longitudinal position, and perpendicular standoff distance result in a wide breadth of bounding surface library entries. To summarize, three cross-sections are each examined for two separate lengths, three perpendicular loading angles, four parallel longitudinal positions, and two perpendicular standoff distances per loading angle, giving 144 unique cases. The parameter combinations selected for the library creation are summarized in Table 3.3.

For each combination of cross-section and length, bounding surface data are also acquired for an undamaged version of that member. Since some of the parameter combinations in Table 3.3 result in no permanent deformation (zero effective plastic strain in the model at the end of the dynamic analysis), failure data acquisition is not undertaken for these models and instead these parameter sets are associated with the bounding surface model for the undamaged member. Combinations resulting in zero damage include all strong-axis blast cases at $X = 5L/2$ for all members, and all weak-axis and half blast cases at $X = 5L/2$ for the two larger sections (W360x122 and W360x162).

Table 3.3: Library parameter space, where each row consists of eight cases that correspond to the cross-section, L, $\Theta_\perp$ combination shown, as repeated for the two listed values of $R_\perp$ and for four values of X, $X = 0, L/4, L, 5L/2$.

Cases	Cross-section	Length, L (m)	$\Theta_\perp$ (deg)	Minimum $R_\perp$ (m)	$1.5 \times$ Minimum $R_\perp$ (m)
1-8	W360x57.8	3.05	0	6.10	9.14
9-16	(W14x38)		45	8.23	12.34
17-24			90	14.63	21.95
25-32		4.57	0	6.10	9.14
33-40			45	8.23	12.34
41-48			90	15.24	22.86
49-56	W360x122	4.57	0	4.57	6.86
57-64	(W14x82)		45	5.18	7.77
65-72			90	6.40	9.60
73-80		6.10	0	4.57	6.86
81-88			45	5.49	8.23
89-96			90	6.10	9.14
97-104	W360x162	6.10	0	6.10	9.14
105-112	(W14x109)		45	3.66	5.49
113-120			90	6.71	10.06
121-128		7.62	0	5.79	8.69
129-136			45	3.66	5.49
137-144			90	6.71	10.06

The dynamic analysis and automated failure data acquisition for each bounding surface are performed on a SGI Altix XE 1300 High Performance Computing Cluster, where each of the 42 nodes has 8 GB of RAM and two quad-core Xeon Processors (2.66 GHz). Clock time ranges from 1.1 to 5.2 hours for a dynamic analysis (on a single processor core), and 5 to 18 hours (across 48 processor cores) for the automated failure data acquisition, for a single bounding surface.

3.4.3 Library implementation in code

The library of bounding surfaces is integrated with the developed nonlinear explicit dynamic finite element code *CU-BAMM* such that the code is able to scan

the library to identify and apply relevant bounding surfaces for each element in a model domain. Individual bounding surface models are described by the 25 coefficients that correspond to the radial yield function in Eq. (3.4), and are indexed within the library by the parameters used to obtain data for that model (cross-section, L, $R_{\perp}$, X, and $\Theta_{\perp}$). These library parameter sets are shown above in Table 3.3.

For any explosive scenario associated with an element in a *CU-BAMM* model that does not match an entry in the bounding surfaces library, the code employs an approximation scheme to find a library entry that is a reasonable approximation for the given element and explosive scenario. Specifically, the code first matches the cross-section parameters (*i.e.* area, moments of inertia, plastic section capacities) for a given element with those corresponding to the cross-sections included in the library. Next, the code scans the library to find the largest length that corresponds to this section, since members with longer unbraced lengths sustain more damage from an explosion. For the cross-section and length chosen, the code then compares the $\Theta_{\perp}$ for the element with the $\Theta_{\perp}$ values in the library, choosing the $\Theta_{\perp}$ from the library that is next largest in size to the $\Theta_{\perp}$ of the element: the rationale here is that blast loading in the weak-axis direction usually results in more damage than blast loading at a perpendicular loading angle that is closer to half or strong-axis blast. Then, for the cross-section and length and $\Theta_{\perp}$ chosen, the code scans the relevant entries of the library to select the one that has the smallest X and $R_{\perp}$ values that exceed the values of X and $R_{\perp}$ associated with the element under consideration. In the end, the code chooses a library entry with parameters (cross-section, L, $R_{\perp}$, X, $\theta_{\perp}$) that represent a close, but conservative approximation for a given element and explosive scenario.

In order to obtain bounding surface data, a sign convention had to be assumed for the applied moment-thrust load combinations for a given member and explosive scenario. To ensure that element end forces have the correct signs, with respect to the sign convention used for bounding surface creation, the code includes a subroutine to map element end forces, for a given explosive scenario, to the appropriate octant of the bounding surface when checking for bounding surface force impingement at element ends. As part of this subroutine, the code is able to handle X and $\Theta_{\perp}$ values outside the ranges specified in the library, or $X < 0$ and $90 < \Theta_{\perp} < 360$ deg, by means of a series of sign transformations.

Additionally, each library entry includes an associated blast arrival time to be applied to the blast beam-column element, within the context of a dynamic analysis performed in *CU-BAMM*. The library arrival time value is extracted from the air blast loading data used in the dynamic blast analysis, and associated with the member and explosive scenario used to create that particular bounding surface in the library. Since the explosion arrival time varies throughout the member spatial domain in the dynamic analysis for the high-resolution model, the single arrival time in the library corresponds to the time that the shock wave first reaches the member midspan for the high-resolution model. In *CU-BAMM*, the bounding surface plasticity models for the blast beam-column elements are activated only after the blast shock wave has reached the longitudinal axis midpoint within the given structural element, or at first subsequent time increment after the arrival time associated with the bounding surface model for that element. Finally, to save computational time, the code calculates the minimum element blast arrival time for the entire model, and adjusts all element arrival times in the model by that amount, so that the bounding surface plasticity model for the closest element to the blast is activated at $t = 0$ in the analysis.

3.5 Single member example

This section discusses a numerical example using a single blast beam-column element to model a vertical column in order to investigate the post-blast response of a single structural member under various applied load combinations.

3.5.1 Single member description

The member consists of a W360x122 (W14x82) wide-flange section, 4.57 m (15 ft) in length, with simply supported boundary conditions. In accordance with all *CU-BAMM* examples presented herein, the material is assumed to be ASTM-A36 steel, with E = 199.4 GPa, ν = 0.3, and ρ = 7850 kg/m^3.

The member response is simulated in *CU-BAMM* for a weak-axis blast explosive scenario, where the charge weight W = 453.6 kg (1000 lb) equivalent TNT explosion is located 9.6 m (31.5 ft) from the member midpoint. A schematic of the member and explosive scenario is included in Fig. 3.3. Note that the bounding surface is defined with axial compression as positive and so the applied axial load on the top column end in Fig. 3.3 is positive, even though it corresponds to a vertical translation in the $-x$ direction with respect to the global coordinate system.

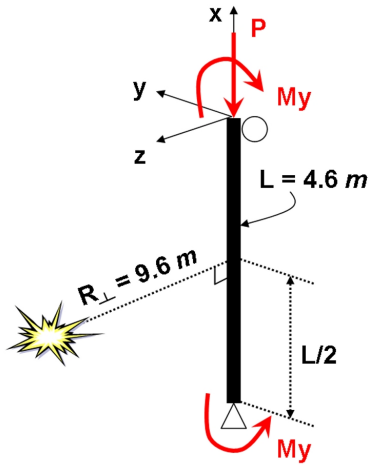

Figure 3.3: Single member model setup, with ASTM-A36 steel wide-flange member consisting of W360x122 (W14x82) cross-section with the web facing the blast.

3.5.2 Single member results

The collapse simulation involves the application of member-end loads, increasing linearly in magnitude with quasi-time, up to a predetermined load level. A quasistatic analysis is carried out by slowly increasing the applied loads until their full value is attained at an analysis time equal to 50 times the fundamental period of the system, or t = 2 s, after which the load is held constant. Applying loads at a rate many times the fundamental period of the system is intended to minimize impact effects. The collapse load for the quasistatic analysis is determined to be the minimum upper bound in loading wherein the member exhibits a load-shedding response after reaching the full load level. Table 3.4 lists two load cases that cause the column to fail. Load Case 1 is a single loading state (axial compression) and Load Case 2 serves as combined loading (axial compression and weak-axis bending).

Table 3.4: Load cases for single member model, for P and M_y as shown in Fig. 3.3 ($M_z = 0$).

Load Case No.	P (kN)	M_y (kN-m)
1	2191.2	0
2	2524.4	49.4

The loading at the column top for Load Case 1 is depicted in Fig. 3.4(a), with zero bending about the weak-axis, and an axial load ramping linearly to a maximum level of 2191.4 kN at $t = 2$ s of analysis time. Plots of the vertical translation and rotation about the weak-axis at the top end are shown in Fig. 3.4(b), below the corresponding applied load plots.

As expected for elastic behavior (*i.e.* a force point inside the bounding surface), the column tip displacement changes linearly with load application until the force point at the element end impinges on the bounding surface at $t = 2$ s, and the column buckles. From Fig. 3.3, it can be seen that the explosion will impose a permanent deformation in the $-z$ direction, corresponding to a rotation in the $-\theta_y$ direction at the top column end. Thus, when the column does collapse, the mode of failure would be expected to be buckling in the $-\theta_y$ direction, adding to the initial deformation from the explosion. The plot of θ_y in Fig. 3.4(b) confirms this expectation, as seen by the sudden change in behavior from zero rotation to unconstrained rotation about the global y-axis in the $-\theta_y$ direction after the structure begins to collapse.

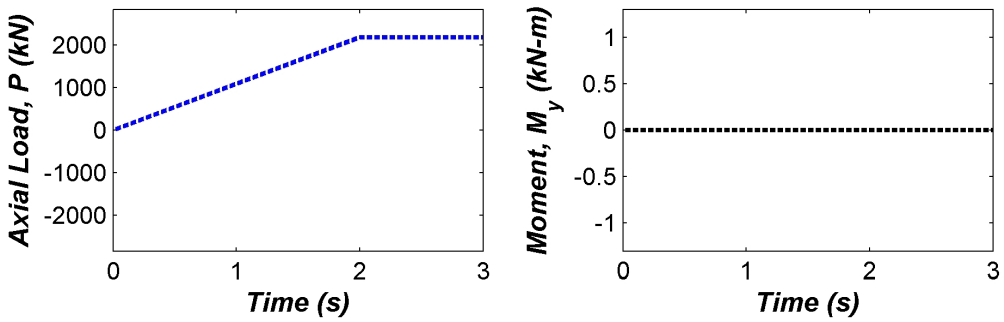

(a) Loading

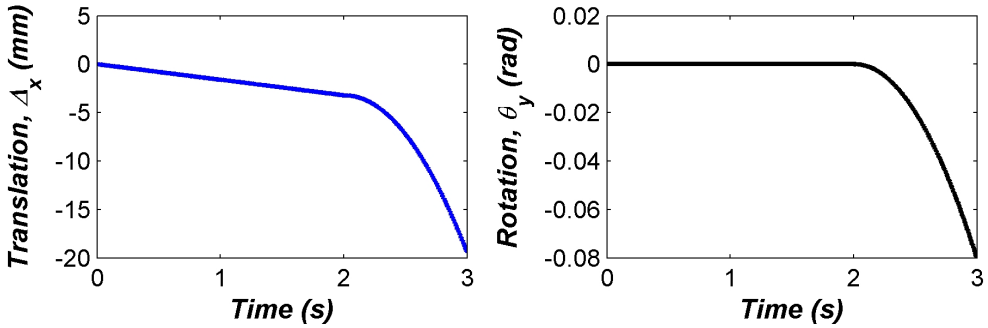

(b) Response

Figure 3.4: Applied loading (axial compression) and structural response (vertical displacement and rotation about weak-axis) at column top, Load Case 1.

For Load Case 2, the applied loads and structural responses are depicted in Fig. 3.5. The axial load and weak-axis moment ramp linearly to maximum values of 2524.5 kN and 49.4 kN, respectively. Again, the column exhibits an elastic response until the full load values are achieved at t = 2 s of analysis time, after which it yields and collapses.

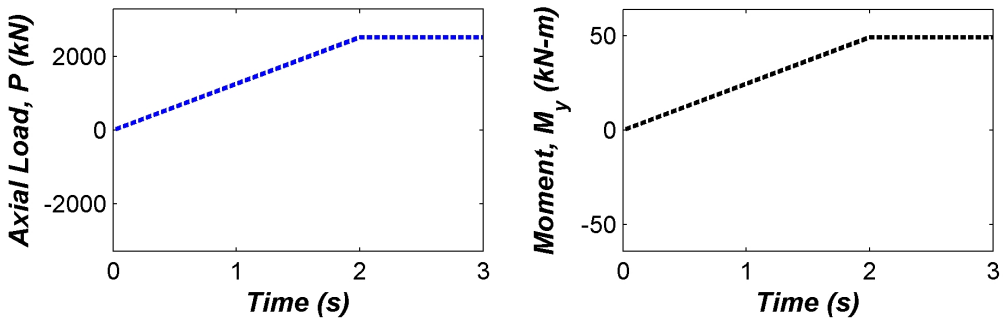

(a) Loading

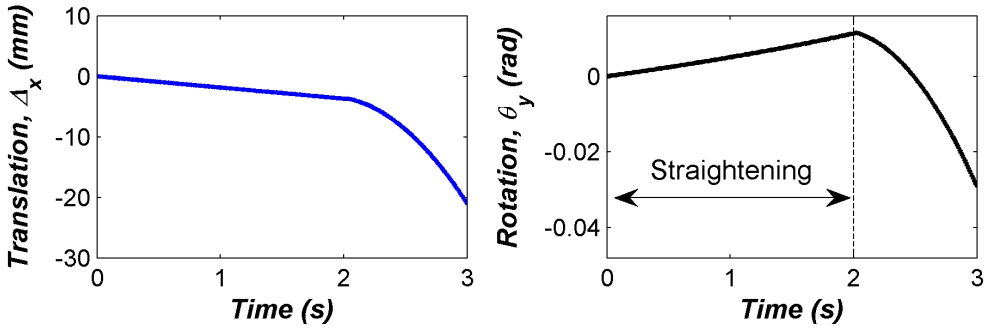

(b) Response

Figure 3.5: Applied loading (axial compression and weak-axis bending) and structural response (vertical displacement and rotation about weak-axis) at column top, Load Case 2.

While the force point at the element top is within the bounding surface in stress-resultant space, the applied moment produces a straightening effect, forcing the column to bend opposite to the direction of blast damage. However, once the column buckles at $t = 2$ s, this effect is reversed and the column resumes rotation in the $-\theta_y$ direction weakened by the explosion, as seen by the sudden reversal in the behavior of θ_y after $t = 2$ s in Fig. 3.5(b).

The plastic behavior described in the above two load cases can be more fully explained by examining the bounding surface for the blast beam-column element used to model the column. Once the force point at an element end reaches

the bounding surface, the assumption of an associated flow rule [30] dictates that the increment in plastic displacement must be normal to the bounding surface in stress-resultant space. Accordingly, the gradient to the surface at a given force point indicates the direction of the increment of plastic displacement to be taken in the next time step. The gradients with respect to normalized stress-resultant space are shown for both load cases at incipient collapse ($t = 2$ s) in Fig. 3.6.

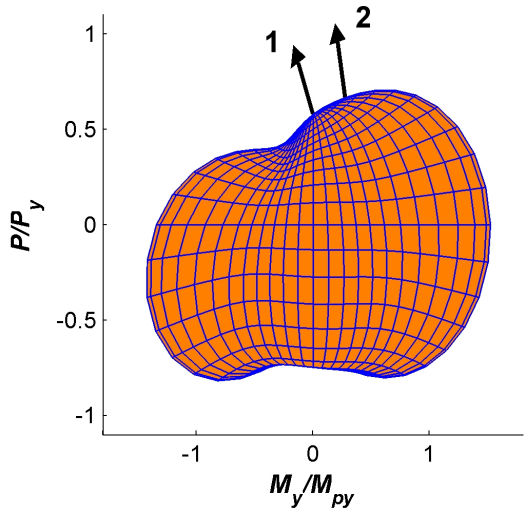

Figure 3.6: Bounding surface model and gradients, with respect to normalized stress-resultant space, for Load Cases 1 and 2 of single member example. Member is W360x122 (W14x82), $L = 4.57$ m long, and explosive scenario is $R_\perp = 9.60$ m, $\Theta_\perp = 90$ deg, and $X = 0$ m (weak-axis blast at midspan).

For both cases, the gradient points in the $-M_y$ direction, which indicates that the plastic displacement increment in the associated degree-of-freedom (θ_y) will be in the opposite direction to the positive sense of M_y at this element end, as is the case for this example.

3.6 A-frame example

The following example compares the post-blast capacity of a structural system damaged by an air blast explosion using two different modeling approaches: a simplified approach with blast beam-column elements (*CU-BAMM*), and a high-resolution, shell element-based modeling approach (LS-DYNA).

3.6.1 A-frame description

The structural system is an A-frame with a vertical member and slanted member connected at a top joint, as illustrated in Fig. 3.7. The structural components consist of W360x122 (W14x82) wide-flange sections, where the vertical member is 4.57 m (15 ft) long, and the slanted member is 6.10 m (20 ft) in length. The A-frame is subjected to a spherical explosion of W = 453.6 kg (1000 lb) equivalent TNT, which is positioned at a perpendicular distance of 9.6 m (31.5 ft) from the point 0.25 m (10 in) above midspan of the vertical member, as shown in Fig. 3.7.

Member cross-sections are oriented with the webs facing the blast, so that the explosion induces a response dominated by weak-axis bending. The top connection is assumed to act as a pin, and this joint is braced out of plane but free to translate in-plane. The bottom two joints are restrained against translation in the three coordinate directions, and against twisting about the member longitudinal axis. The material is assumed to be ASTM-A36 steel, with E = 199.4 GPa, ν = 0.3, and ρ = 7850 kg/m^3. The high-resolution model uses the simplified Johnson-Cook relation in Eq. (3.13) to model material behavior, with the same parameter values that were used for the bounding surface data acquisition.

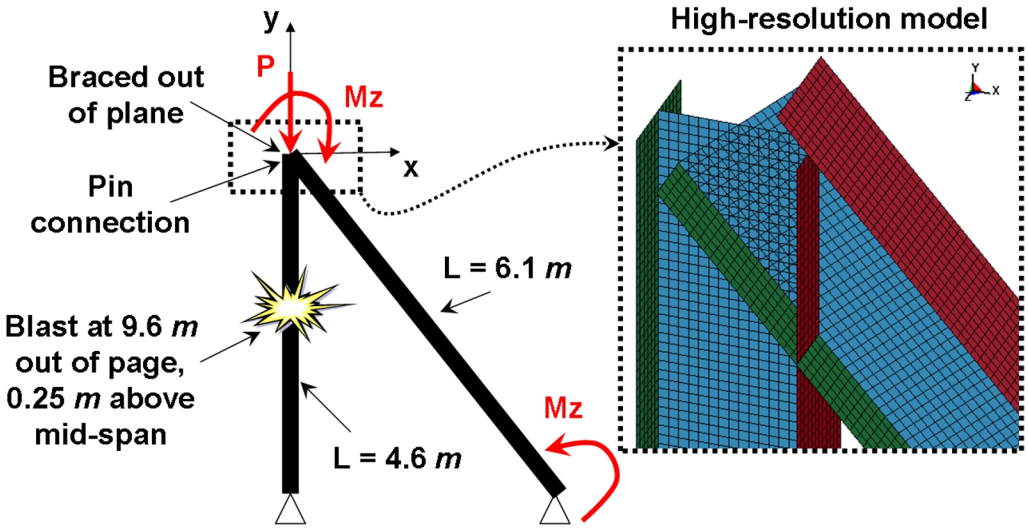

Figure 3.7: A-frame model setup, with ASTM-A36 steel wide-flange members consisting of W360x122 (W14x82) sections with the webs facing the blast.

The high-resolution simulation in LS-DYNA requires a two-step process, similar to the procedure used for the failure data acquisition. First, a nonlinear dynamic analysis is performed to determine the response of the members to the explosive loading, and then the damaged configuration is loaded in a separate static analysis, whereby axial and moment loads are applied at member ends, and linearly increased until the system becomes unstable and collapse commences. In the same manner as the collapse analyses carried out for the bounding surface failure data acquisition [30], the axial load is applied as a point load at the member cross-section centroid, and the moment is applied as a force couple via point loads applied at the flange tips. The dynamic effects of the explosion are modeled within the dynamic analysis through the application of a series of nodal force time histories calculated using the air blast loading code developed by the authors [28].

In *CU-BAMM*, a quasistatic analysis is carried out to determine the collapse load for the A-frame system. Loads are applied to the top and bottom right joints with a ramp function, similar to that for the column example. Thus, the loads are increased linearly, with quasi-time, until reaching a predetermined load level, after which they are maintained at a constant value. To minimize impact effects, the applied loads do not attain their maximum value until an analysis time equal to 50 times the fundamental period of the A-frame system, or t = 4 s. Several analysis iterations are performed to find the collapse load.

The high-resolution model utilizes the same general finite element modeling approach for the W360x122 (W14x82) wide-flange members that were used for the failure data acquisition; thus, it is composed of Belytschko-Lin-Tsay shell elements [31] to model the plates and very stiff Belytschko-Schwer [31] beam elements, at the member ends, to suppress cross-sectional distortion at the joints. Using a global mesh seed of 6 elements per flange outstand, this model includes 20080 elements (19920 shells and 160 beams) and 20499 nodes. The *CU-BAMM* model consists of one blast beam-column element per member, for a total of 2 elements and 3 nodes.

As discussed previously, *CU-BAMM* does not explicitly model the explosion itself, but rather calculates a series of parameters that define the explosion location relative to a given member, and then accesses the library of bounding surfaces to find the bounding surface with parameters that most reasonably approximate the actual physical explosive scenario, and member geometry. A comparison between actual bounding surface parameters and those determined by the bounding surface library interaction algorithm in *CU-BAMM* for the two components is shown in Table 3.5.

Table 3.5: Comparison of actual versus library bounding surface parameter sets for A-frame components.

Component	Cross-section	Length, L (m)	$\Theta_\perp$ (deg)	$R_\perp$ (m)	X (m)
Vertical (actual)	W360x122	4.57	90	9.60	0.25
Vertical (library)	W360x122	4.57	90	9.60	0
Slanted (actual)	W360x122	6.10	82	9.70	1.52
Slanted (library)	W360x122	6.10	90	9.14	1.52

For both models, the pin connection ensures that no moment is transferred at the top joint, causing each structural component to experience a loading state that is decoupled in a moment sense. For the applied loads pictured in Fig. 3.7, this means that, to the first order, the vertical member is in pure compression, and the slanted member is in pure strong-axis flexure. Three load cases are considered for this example, corresponding to the failure of one or both members. The applied load cases and their associated intended end results are summarized in Table 3.6. Actual results for *CU-BAMM* and the high-resolution model will be discussed subsequently.

Table 3.6: Load cases and reference loads for A-frame models, for P and M_z (as shown in Fig. 3.7).

Load Case No.	Intended End Result	P (kN)	M_z (kN-m)
1	Vertical Member Fails	2189.4	113.0
2	Slanted Member Fails	889.6	453.6
3	Both Members Fail	2148.5	453.7

3.6.2 A-frame results and discussion

The failure loads for the different approaches are quantitatively compared using a collapse index (CI), which is defined to be the ratio of recorded failure load to

reference load, or ratio of length of applied load vector at failure to length of reference load vector, for a given load combination. Thus, the collapse index is defined by the following ratio of ℓ_2 norms,

$$CI = \frac{\left\| \text{ Applied Load Vector at Failure } \right\|_2}{\| \text{ Reference Load Vector } \|_2}, \tag{3.15}$$

where the reference loads for each load case are defined in Table 3.6. By design, the reference loads are actually equal to the failure loads for the *CU-BAMM* simulation at each listed load combination, giving a collapse index equal to unity, or $CI = 1.0$, for these.

For the high-resolution model, the loads are applied proportionally along the load vector $\mathbf{Q}$ until collapse ensues. The constant of proportionality is called the load proportionality factor (LPF), and so $\mathbf{Q} = LPF \cdot \left\{ P \; M_y \; M_z \right\}$ here, where P and M_z are listed for each load case in Table 3.6 and $M_y = 0$ for all cases. From the definition of the collapse index in Eq. (3.15), it can be seen that the collapse index for the high-resolution model is just equal to the maximum value of the load proportionality factor (LPF) in this context.

As a further point for comparison, the collapse index is computed for the actual failure data used to produce the bounding surface model for the individual beam-column element assigned to each A-frame member as part of the *CU-BAMM* analyses. The load vectors represented by the load combinations in Table 3.6 have already been considered as part of the bounding surface data acquisition and so the collapse index for these can simply be computed by dividing the length of the appropriate load vector at failure by the length of the reference load vector. Fig. 3.8, 3.9, and 3.10 depict the collapse index results for the simplified and high-resolution approaches and the failure data.

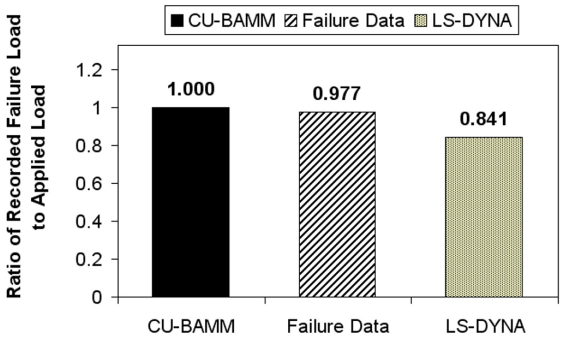

Figure 3.8: Collapse index comparison: failure of vertical member (Load Case 1).

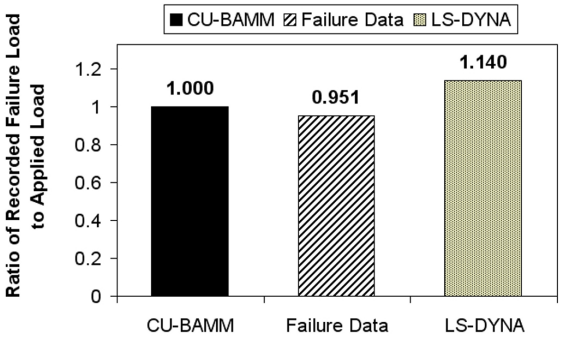

Figure 3.9: Collapse index comparison: failure of slanted member (Load Case 2).

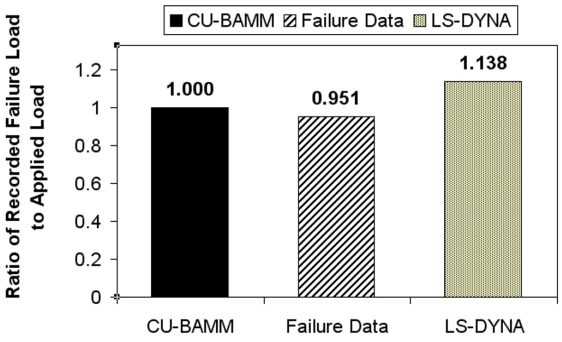

Figure 3.10: Collapse index comparison: failure of both members (Load Case 3).

The collapse index results for the A-frame test case show that the simplified blast beam-column approach implemented in *CU-BAMM* is able to predict post-

blast collapse loads within ±16% of the high-resolution model results from LS-DYNA for the chosen load cases. For loading causing the slanted member to fail (Load Cases 2 and 3), the collapse load is underpredicted by 14% using *CU-BAMM*, and for loading causing the vertical member to buckle (Load Case 1), the failure load predicted by the high resolution model is 16% less than that determined by *CU-BAMM*.

The above discrepancies can be attributed to a number of factors including boundary condition assumptions, bounding surface fit error, and bounding surface approximations employed by the bounding surface library interaction algorithm implemented in the code. Regarding boundary condition assumptions, the finite element models used to generate the bounding surface data for a single blast beam-column element assume simply supported boundary conditions (pin and roller). However, the top joint of the A-frame is free to translate in-plane, adding a component of lateral translation not allowed in the failure data acquisition models. Lateral translation of the top joint introduces a $P - \Delta$ effect that reduces member resistance against global buckling, an effect not accounted for in the bounding surfaces used for the post-blast collapse load calculation in *CU-BAMM*. Accordingly, this $P - \Delta$ effect is likely the cause of the reduced CI seen in the high-resolution results for Load Case 1.

Another source of error is the approximation of the bounding surface failure data with a continuous radial yield function (a weighted sum of real-valued spherical harmonics). Fig. 3.8, 3.9, and 3.10 report collapse index values that are less than unity for the failure data, as compared to the collapse index values of unity for *CU-BAMM*, indicating that the bounding surface models fitted to the failure data are overly conservative at the load combinations chosen for this ex-

ample. Thus, the bounding surfaces used to model the members and explosive scenarios for these load cases will produce an overprediction of the post-blast capacity of the A-frame. While this error could be eliminated by using the actual faceted bounding surface failure data in place of the radial yield function, this alternative approach could cause numerical problems when attempting to calculate the gradient $\nabla\Phi$ to the interpolated surface at a force point in stress-resultant space where the data are not smooth (*i.e.* at facet corners).

Now while the overly conservative fit to the bounding surface data discussed above will contribute to collapse index values less than unity for the high-resolution models (*i.e.* an overprediction of collapse load by *CU-BAMM*), the collapse index values for the high-resolution models are greater than unity for the two load cases involving failure of the slanted member. However, this observation may be partially explained by the error that is introduced into the post-blast collapse load determination through the bounding surface approximations employed by the bounding surface library interaction algorithm implemented in *CU-BAMM*. As detailed in Table 3.5, the bounding surface used to model the post-blast behavior of the slanted member is based on an explosion located at $R_{\perp} = 9.14$ m (library entry), yet the actual explosion is located farther away at a perpendicular standoff distance of $R_{\perp} = 9.70$ m. Since the damage caused by an explosion scales with standoff distance, this approximation will lead to an overprediction of the damage caused by the blast, and thus an underprediction of the A-frame collapse load by *CU-BAMM*.

There is a large disparity in computational expense between the two modeling approaches, at least in terms of run time. The high-resolution simulation is performed on a single processor core of a SGI Altix XE 1300 High Performance

Computing Cluster, where each computational node has 8 GB of RAM and two quad-core Xeon Processors (2.66 GHz). Clock time ranges from 7.5 to 8 hours for the analyses using the high-resolution model. The *CU-BAMM* simulations are carried out on a single processor core within a laptop that has 2 GB of RAM and a dual-core Intel Processor (2.00 GHz), each taking less than 1 min of clock time. For this example, the simplified blast beam-column element approach provides a good approximation to the post-blast collapse load of a structural system at a tiny fraction of the computational expense incurred by a high-resolution model. As mentioned previously, creation of the bounding surfaces library does incur a substantial up-front computational cost, which is not accounted for in the above comparisons of computational expense. However, after the library has been established, numerous parametric studies can be carried out with *CU-BAMM* at a much reduced computational cost as compared to the high-resolution modeling approach, a fact that can justify the library creation cost.

3.7 Through-truss example

The following example is presented to demonstrate a potential practical application for the developed blast beam-column element approach. To maintain consistency with the assumptions inherent in the air blast load computation and general methodology used to develop the bounding surfaces library, the example focuses on a steel skeletal structure, comprised of wide-flange members, that is subjected to a spherical open-air explosion. The example structure is a three-dimensional through-truss modeled loosely on a railroad bridge system.

3.7.1 Through-truss description

A schematic of the through-truss is shown in Fig. 3.11. The structural system includes two trusses at the front and back of the structure, each with longitudinal members separated by angled diagonals to form a pattern of alternately inverted equilateral triangles.

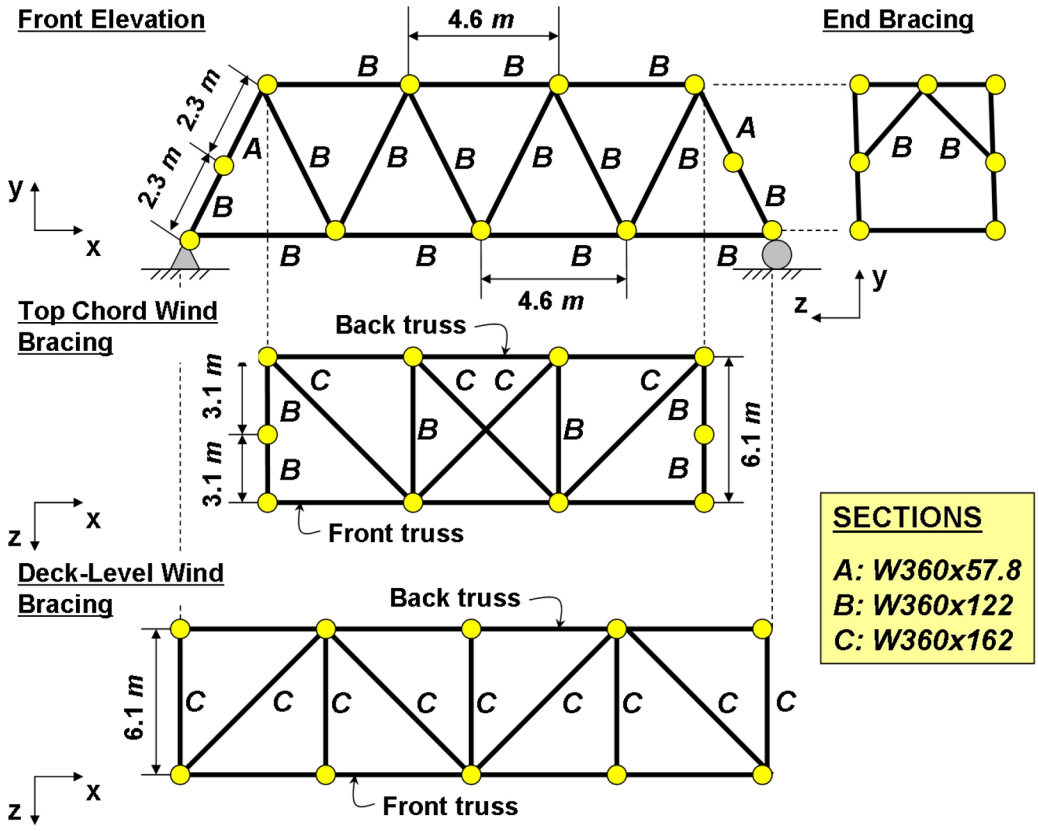

Figure 3.11: Through-truss model setup, with ASTM-A36 steel wide-flange members consisting of W360x57.8 (W14x38), W360x122 (W14x82), and W360x162 (W14x109) sections and one blast beam-column element assigned per member.

The main trusses are connected by struts and lateral bracing in the top, bottom, and ends of the structure to provide structural stability. Although lateral bracing would usually employ smaller sections than chord members, which are

mostly W360x122 in this case, heavier W360x162 sections are used in this example to fully explore the breadth of the bounding surfaces library.

The through-truss is assumed to be simply supported, with pins at the front and back chord panel points on the left end, and rollers at the front and back bottom chord panel points on the right end. In these locations, the structure is also assumed to be braced out of plane. Member joints are not expected to act as pins, under the assumption that a realistic blast would cause damage that could inhibit rotation at joints. The through-truss is modeled with *CU-BAMM* using one blast beam-column element per member, giving a model with 57 elements and 24 nodes.

The through-truss is damaged by a spherical explosion of $W = 453.6$ kg (1000 lb) equivalent TNT, located as shown in Fig. 3.12. The blast is centered on the midpoint of the front truss bottom chord member that is the second from the right end, and the blast epicenter is located a vertical distance of 3.05 m below the bottom plane of the structure, and at a transverse distance of 7.11 m outward from this midpoint.

This explosion location corresponds to a perpendicular standoff of $R_{\perp} = 7.74$ m, a parallel longitudinal position of $X = 0$, and a perpendicular loading angle of $\Theta_{\perp} = 66.8$ deg for the front truss bottom chord member second from the right. Explosive scenario parameters $R_{\perp}$, X, and $\Theta_{\perp}$ take on various values for the remaining 56 members, ranging from $41.0 - 187.9$ m for $R_{\perp}$, $0 - 3.8L$ for X, and $0 - 86.7$ deg for $\Theta_{\perp}$.

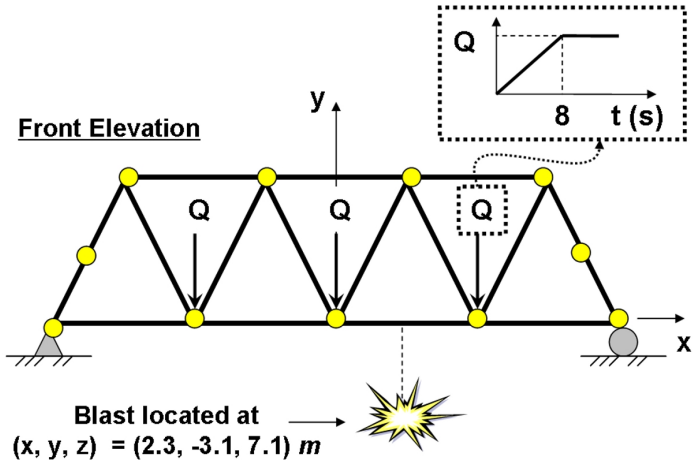

Figure 3.12: Through-truss blast location and quasistatic post-blast loading. In the front and back trusses, member webs face the blast.

Similar to previously discussed numerical examples, a quasistatic analysis is carried out in *CU-BAMM* to determine the post-blast collapse load for this structural system. Loads are applied to the interior panel points on the bottom of the front and back trusses with a ramp function, as illustrated in Fig. 3.12. The loads are increased linearly with quasi-time until reaching the maximum load level at t = 8 s, after which they are held constant.

3.7.2 Through-truss results and discussion

Several analysis iterations are carried out for different values of the maximum static load, Q, in order to determine the value of the collapse load. Fig. 3.13 compares the vertical translation, Δ_y, at the middle joint of the bottom chord of the front truss for analyses for Q = 601.5 kN and Q = 601.6 kN. As a reference, this measurement point is located at the origin of the model global coordinate system in Fig. 3.12. The vertical translation at this point is chosen as a represen-

tative response metric since it measures the sag of the global structural system, and thus unconstrained displacement for this degree-of-freedom would be an indication of global collapse.

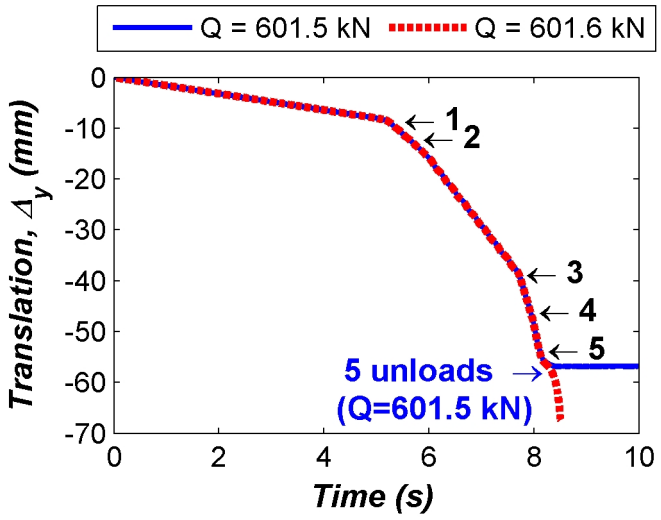

Figure 3.13: Vertical y-translation at middle joint of the front truss bottom chord for Q = 601.5 kN and Q = 601.6 kN. Numbers correspond to times at which a through-truss member has failed; all failed members remain failed for the entire analysis except as noted.

For Q = 601.6 kN, as applied to this structural system and explosive scenario, Fig. 3.13 demonstrates that unconstrained displacement takes place shortly after reaching the full load level. However, while a slightly smaller load of Q = 601.5 kN causes some members to fail, the structure is able to redistribute forces in such a way that nodal displacements are bounded. Thus, Q = 601.6 kN is deemed to be the post-blast collapse load for this example.

The numbered labels in Fig. 3.13 correspond to time points at which a member of the through-truss has failed. Upon comparing the response of the through-truss for the near-collapse (Q = 601.5 kN) and collapse (Q = 601.6 kN) loads, it is apparent that the response remains the same until soon after the full

load level is attained. In fact, at $t = 8.34$ s of solution time, the fifth failed element in the near-collapse model is able to unload elastically, stabilizing the structural system and thus preventing global collapse.

Fig. 3.14 depicts a detail of the through-truss right end, where the failed elements are marked in order of failure. The following observations can be made when correlating the response data in Fig. 3.13 with the element locations in Fig. 3.14: failure of the first and third members markedly softens the global structural response, as seen by the noticeable change in the slope of the displacement after these failures; failure of the second and fourth members has less of an effect on the global structural response; and failure of the fifth element leads to global collapse.

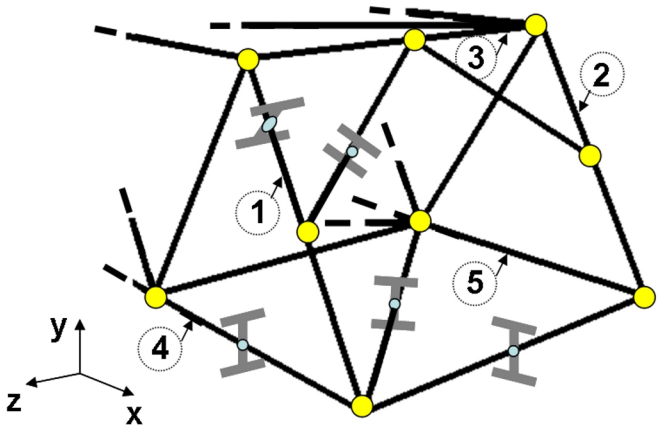

Figure 3.14: Detail of through-truss right end, including cross-section orientations and failed members (labeled in order of failure).

The exact mechanism for collapse is most clearly seen in contour plots of nodal horizontal translation Δ_x at different analysis times, shown in Fig. 3.15. At $t = 8.34$ s, four members have failed, and the fifth one fails just after the snapshot in Fig. 3.15(a). After the failure of the fifth member, a mechanism forms for global collapse via buckling of the right end of the through-truss.

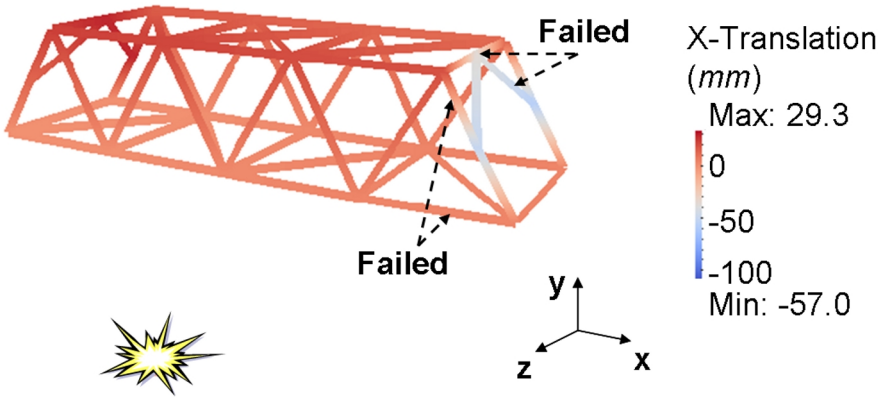

(a) $t = 8.34$ s

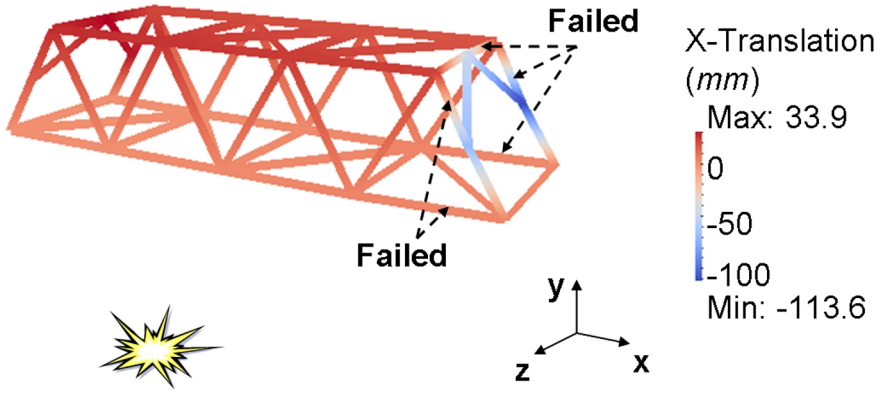

(b) $t = 8.50$ s

Figure 3.15: Contour plot of joint horizontal x-translation of through-truss at $t = 8.34$ s and $t = 8.50$ s for collapse load $Q = 601.6$ kN, with failed elements denoted accordingly.

This collapse mechanism can be seen by comparing the extreme values of Δ_x in Fig. 3.15(a) and Fig. 3.15(b). In the interval of analysis time between these snapshots, the top of the through-truss has moved farther in the $+x$ direction, whereas the mid-height joints of the diagonal members on the right end have moved farther in the $-x$ direction. This trend also produces a significant rotation in θ_z and a downward displacement in Δ_y at the same locations, which are not shown here.

3.8 Conclusions

An approach to modeling the post-blast behavior of steel skeletal structures using blast beam-column elements has been described in this paper and a companion paper [30]. The approach leverages a library of bounding surface plasticity models based on numerical failure data from high-resolution models of individual wide-flange members, in order to facilitate a macro-element description of blast-damaged wide-flange components in a finite element context. Such an approach enables a system-wide consideration of post-event structural performance that would be prohibitively expensive with high-resolution modeling tools. In particular, a finite element code employing the developed blast beam-column element would enable computationally efficient evaluation of the effects associated with numerous explosion locations and loading scenarios for a structure subjected to explosive air blast.

3.9 Acknowledgment

This paper is based upon research supported by Cornell University and a National Science Foundation Graduate Research Fellowship. Any opinions, findings, conclusions or recommendations expressed in this publication are those of the authors and do not necessarily reflect the views of the National Science Foundation. The authors would also like to acknowledge the contributions made to this research by Heather Reed at Cornell University.

CHAPTER 4

FUTURE WORK

Future work for the blast beam-column element approach should focus on minimizing the error incurred by using this method in its current state. Investigating alternative functional forms to fit the bounding surface data might yield a functional form that more closely captures the salient features of the bounding surface data, thus decreasing fit error. Exploring possible parameterizations of the bounding surfaces to allow for interpolation between surfaces defined for discrete combinations of members and explosive scenarios (rather than choosing a close, but conservative bounding surface model) could reduce the approximation error in the current bounding surfaces library interaction algorithm. This step would also increase the robustness of the proposed approach, especially if the parameterization could be used for interpolation of bounding surfaces between material types other than the ASTM-A36 steel examined herein. Potential alternate materials may include ASTM-A992 or other Grade 50 steels.

Additional future research should also be carried out to increase the robustness of the blast beam-column approach as implemented in the developed code. Further population of the bounding surfaces library for different sections, including channels or angles, would increase the applicability of the code. Future work might also focus on examining the behavior of various steel connections under explosive loading with a view towards creating macro-models to characterize post-blast connection behavior. A nonlinear finite element code with the developed blast beam-column macro-element implemented together with a library of connection macro-models would provide a very powerful tool for computationally efficient assessment of blast effects in steel skeletal structures.

BIBLIOGRAPHY

[1] ADINA R&D, Inc., Watertown, MA. *ADINA Theory and Modeling Guide*, November 2006.

[2] AISC. *Manual of Steel Construction Load and Resistance Factor Design: Structural Members, Specifications and Codes*. American Institute of Steel Construction AISC, 2nd edition, 1998.

[3] AISC. *Specification for structural steel buildings*. American Institute of Steel Construction AISC, March 2005.

[4] R. Andersson, M. Syk, and C. Magnusson. The development of high strain rate equations for stainless steels. *Journal of Materials Engineering and Performance*, 14(5):553–562, 2005.

[5] ASCE-WRC. *Plastic Design in Steel: A Guide and Commentary*. ASCE, New York, 2nd edition, 1971.

[6] W. E. Baker. *Explosions in Air*. University of Texas Press, Austin, 1973.

[7] W. E. Baker, P. A. Cox, P. S. Westine, J. J. Kulesz, and R. A. Strehlow. *Explosion Hazards and Evaluation*. Elsevier, New York, 1983.

[8] A. Bassi, F. Genna, and P.S. Symonds. Anomalous elastic–plastic responses to short pulse loading of circular plates. *International Journal of Impact Engineering*, 28:65–91, 2002.

[9] Klaus-Jurgen Bathe. *Finite element procedures*. Prentice Hall, New Jersey, 1996.

[10] James T. Baylot and Denis D. Rickman. Uncertainties in blast loads on structures. In *Proceedings of ASCE Structures Congress*, May 2007.

[11] F. B. A. Beshara. Modelling of blast loading on aboveground structures–I, general phenomenology and external blast. *Computers and Structures*, 51(5):585–596, 1994.

[12] M.A. Blanco, M. Florez, and M. Bermejo. Evaluation of the rotation matrices in the basis of real spherical harmonics. In *THEOCHEM–Journal of Molecular Structure*, volume 419, pages 19–27, November 1–30 1997.

[13] W. Bleakney, D. R. White, and W. C. Griffith. Measurements of diffraction of shock waves and resulting loading of structures. *Journal of Applied Mechanics – Transactions of the ASME*, 17(4):439–445, 1950.

[14] David D. Bogosian, Brian W. Dunn, and Jon D. Chrostowski. Blast analysis of complex structures using physics–based fast–running models. *Computers & Structures*, 72:81–92, 1999.

[15] David D. Bogosian, John Ferritto, and Yongjiang Shi. Measuring uncertainty and conservatism in simplified blast models. In *30th DoD Explosives Safety Seminar Proceedings*, Atlanta, GA, August 2002. Department of Defense Explosives Safety Board.

[16] Elan Borenstein and Haym Benaroya. Sensitivity analysis of blast loading parameters and their trends as uncertainty increases. *Journal of Sound and Vibration*, 321(3–5):762–785, 2009.

[17] Christian Brechbuhler, G. Gerig, and O. Kubler. Parametrization of closed surfaces for 3-D shape description. *Computer Vision and Image Understanding*, 61:154–170, 1995.

[18] Harold L. Brode. Quick estimates of peak overpressure from two simultaneous blast waves. Technical Report DNA4503T, Defense Nuclear Agency, Aberdeen Proving Ground, MD, December 1977.

[19] Gilles Burel and Hugues Henocq. Three-dimensional invariants and their application to object recognition. *Signal Processing*, 45:1–22, 1995.

[20] H. Chen and J. Y. R. Liew. Explosion and fire analysis of steel frames using mixed element approach. *Journal of Engineering Mechanics*, 131(6):606–616, 2005.

[21] J. M. K. Chock and R. K. Kapania. Review of two methods for calculating explosive air blast. *The Shock and Vibration Digest*, 33(2):91–102, 2001.

[22] Robert D. Cook, David S. Malkus, Michael E. Plesha, and Robert J. Witt. *Concepts and applications of finite element analysis*. John Wiley and Sons, Inc., New York, 4th edition, 2002.

[23] W. Gene Corley. Lessons learned on improving resistance of buildings to terrorist attacks. *Journal of Performance of Constructed Facilities*, 18(2):68–78, 2004.

[24] Jean-Louis Dillenseger, Helene Guillaume, and Jean-Jacques Patard. Spherical harmonics based intrasubject 3-D kidney modeling/registration technique applied on partial information. *IEEE Transactions on Biomedical Engineering*, 53:2185–2193, 2006.

[25] Sherif El-Tawil and Gregory G. Deierlein. Stress-resultant plasticity for frame structures. *Journal of Engineering Mechanics*, 124(12):1360–1370, 1998.

[26] FEMA. *Reference Manual to Mitigate Potential Terrorist Attacks Against Buildings (FEMA-426)*. Washington, DC, December 2003.

[27] Jason R. Florek and Haym Benaroya. Pulse-pressure loading effects on aviation and general engineering structures–review. *Journal of Sound and Vibration*, 284(1–2):421–453, 2005.

[28] Emily Leigh Guzas and Christopher J. Earls. Air blast load generation for simulating structural response. *Steel and Composite Structures*, TBD(TBD):(under review), TBD.

[29] Emily Leigh Guzas and Christopher J. Earls. Simulating blast effects on steel beam-column members: Applications. *Computers & Structures*, TBD(TBD):(under review), TBD.

[30] Emily Leigh Guzas and Christopher J. Earls. Simulating blast effects on steel beam-column members: Methods. *Computers & Structures*, TBD(TBD):(under review), TBD.

[31] John O. Hallquist. *LS-DYNA Theory Manual, Version 971*. Livermore Software Technology Corporation, Livermore, CA, March 2006.

[32] S.I. Hilmy and John F. Abel. A strain–hardening concentrated plasticity model for nonlinear dynamic analysis of steel buildings. In *NUMETA85, Numerical Methods in Engineering: Theory and Applications*, volume 1, pages 305–314, Rotterdam, The Netherlands, January 1985.

[33] David Hyde. *ConWep – Application of TM5-855-1*. Structural Mechanics Division, Structures Laboratory, USAE Waterways Experiment Station, Vicksburg, MS, August 1992.

[34] G. Johnson and W. H. Cook. A constitutive model and data for metals subjected to large strains, high strain rates and high temperatures. In *Proceed-*

ings of 7th International Symposium on Ballistics, pages 541–547, The Hague, The Netherlands, April 1983.

[35] G. R. Johnson and W. H. Cook. Fracture characteristics of three metals subjected to various strains, strain rates, temperatures and pressures. *Engineering Fracture Mechanics*, 21(1):31–48, 1985.

[36] J. Kajberg and B. Wikman. Viscoplastic parameter estimation by high strain-rate experiments and inverse modelling – speckle measurements and high-speed photography. *International Journal of Solids and Structures*, 44(1):145–164, 2007.

[37] Jesse E. Karns, David L. Houghton, Bruce E. Hall, Joonghwan Kim, and Kyungkoo Lee. Blast testing of steel frame assemblies to assess the implications of connection behavior on progressive collapse. In *Structures Congress 2006: Structural Engineering and Public Safety – Proceedings of the 2006 Structures Congress*, volume 2006, page 32, St. Louis, MO, May 18–21 2006.

[38] Jesse E. Karns, David L. Houghton, Bruce E. Hall, Joonghwan Kim, and Kyungkoo Lee. Analytical verification of blast testing of steel frame moment connection assemblies. In John W. Wallace, editor, *Proceedings of the Research Frontiers Sessions of the 2007 Structures Congress*, volume 2007, pages 1–19, Long Beach, CA, May 16–19 2007. ASCE.

[39] Jesse E. Karns, David L. Houghton, Jong-Kook Hong, and Joonghwan Kim. Blast testing of steel frame assemblies to assess the implications of connection behavior on progressive collapse. In *Proceedings of the 2009 Structures Congress – Don't Mess with Structural Engineers: Expanding Our Role*, volume 2009, pages 1868–1877, Austin, TX, April 30–May 2 2009.

[40] C. N. Kingery and G. Bulmash. Airblast parameters from TNT spherical air burst and hemispherical surface burst. Technical Report ARBRL-TR-02555, Armament Research and Development Center, Ballistic Research Laboratory, Aberdeen Proving Ground, MD, April 1984.

[41] G. F. Kinney and K. J. Graham. *Explosive Shocks in Air*. Springer-Verlag, New York, 2nd edition, 1985.

[42] Bruce R. Kusse and Erik A. Westwig. *Mathematical Physics: Applied Mathematics for Scientists and Engineers*. John Wiley and Sons, Inc., New York, 1998.

[43] Darell Lawver, Raymond Daddazio, David Vaughan, Michael Stanley, and Howard Levine. Response of AISC steel columns to blast loading. In *ASME Pressure Vessels Piping Div Publ PVP, Problems Involving Thermal-Hydraulics, Liquid Sloshing, and Extreme Loads on Structures*, volume 454, pages 139–148, Cleveland, OH, July 20–24 2003.

[44] J. Y. R. Liew. Survivability of steel frame structures subject to blast and fire. *Journal of Constructional Steel Research*, 64(7–8):854–866, 2008.

[45] LS-DYNA. *LS-DYNA Keyword User's Manual, Version 971, Vols. 1–2*. Livermore Software Technology Corporation, Livermore, CA, May 2007.

[46] Joseph M. Magallanes, Ruben Martinez, and John W. Koenig. Experimental results of the AISC full–scale column blast test. Technical Report TR-06-20.2, Contract No. KC–05–27.2, Karagozian & Case (KCSE), Battelle, Columbus, OH, March 21 2006.

[47] G. C. Mays and P. D. Smith. *Blast Effects on Buildings*. Thomas Telford Service Ltd., London, 1995.

[48] William Mcguire, Richard H. Gallagher, and Ronald D. Ziemian. *Matrix Structural Analysis*. John Wiley and Sons, Inc., New York, 2nd edition, 2000.

[49] James G. Orbison, William McGuire, and John F. Abel. Yield surface applications in nonlinear steel frame analysis. *Computer Methods in Applied Mechanics and Engineering*, 33(1–3):557–573, 1982.

[50] F.L. Porter and G.H. Powell. Static and dynamic analysis of inelastic frame structures. Technical Report EERC-71-3, Earthquake Engineering Research Center, Univeristy of California at Berkeley, California, June 1971.

[51] G.H. Powell and P.F.S. Chen. 3D beam-column element with generalized plastic hinges. *Journal of Engineering Mechanics*, 112(7):627–641, 1986.

[52] Glenn Randers-Pehrson and Kenneth A. Bannister. Airblast loading model for DYNA2D and DYNA3D. Technical Report ARL-TR-1310, Army Research Laboratory, Aberdeen Proving Ground, MD, March 1997.

[53] Denis D. Rickman and Donald W. Murrell. Development of an improved methodology for predicting airblast pressure relief on a directly loaded wall. *Journal of Pressure Vessel Technology*, 129:195–204, 2007.

[54] J. M. Santiago and S. Bhattacharya. Sensitivity of plate response calculations to blast load definition. *Computers and Structures*, 40(2):375–392., 1991.

[55] Leonard Schwer. Optional strain-rate forms for the Johnson-Cook constitutive model and the role of the parameter epsilon_0. In *Proceedings of the 77th Shock and Vibration Symposium (SAVIAC)*, Monterey, CA, October 29–November 3 2006.

[56] Leonard Schwer. Optional strain-rate forms for the Johnson-Cook constitutive model and the role of the parameter epsilon_0. In *Proceedings of the 6th German LS-DYNA Forum*, Frankenthal, Germany, October 11–12 2007.

[57] Jeremy D. Seidt. EOD material characterization final report: Constitutive and fracture model development of multiple materials for three dimensional EOD impact simulations. Technical Report NAVEODTECHDIV Subcontract No. 05-OAT-0003, Naval Explosive Ordnance Disposal Technology Division (NAVEODTECHDIV), Battelle, Columbus, OH, August 2006.

[58] Li Shen, Mark A. McPeek, and Hany Farid. Modeling three-dimensional morphological structures using spherical harmonics. *Evolution*, 63:1003–1016, April 2009.

[59] P. D. Smith and J. G. Hetherington. *Blast and Ballistic Loading of Structures*. Butterworth-Heinemenn Ltd., London, 1994.

[60] L. Song, B.A. Izzuddin, A.S. Elnashai, and P.J. Dowling. An integrated adaptive environment for fire and explosion analysis of steel frames – part I: Analytical models. *Journal of Constructional Steel Research*, 53(1):63–85, 2000.

[61] US Air Force US Army, US Navy. Structures to resist the effects of accidental explosions. Technical Report TM 5-1300/NAVFAC P-397/AFR 88-22, November 1990.